



UNIVERSITY OF PADUA FACULTY OF ENGINEERING

DEPARTMENT OF MANAGEMENT AND ENGINEERING

DOCTORAL SCHOOL OF INDUSTRIAL ENGINEERING
CURRICULUM IN MECHATRONICS AND INDUSTRIAL SYSTEMS
CYCLE XIII

MAGNETIC FIELD SENSORS SUITABLE FOR HIGH TEMPERATURE AND VACUUM OPERATIONS AND FOR REMOTE HANDLING IN HARSH ENVIRONMENT

PROF. PAOLO FRANCESCO BARIANI, CHAIR OF THE SCHOOL
PROF. ALBERTO TREVISANI, COURSE COORDINATOR
PROF. GIUSEPPE CHITARIN, ADVISOR

Ph.D Candidate: ANTONIO GALLO

alla mia famiglia

Table of contents

1	Energy and nuclear fusion	10
1.1	Introduction.....	10
1.2	The nuclear fusion process.....	11
1.3	ITER device	12
2	ITER magnetic diagnostic.....	15
2.1	Working principles of magnetic sensors.....	15
2.1.1	Pick-up coil and flux loop.....	15
2.1.2	Rogowski coil	16
2.1.3	Hall sensors	18
2.2	Implementation of In-Vessel pick-up magnetic coils on existing devices	19
2.2.1	JET	20
2.2.2	RFX-mod	22
2.2.3	JT-60 Upgrade	23
2.3	ITER in-Vessel magnetic sensors	23
2.4	Description of previous design of ITER tangential and normal coils.....	25
2.5	Challenges in the construction of in-Vessel magnetic sensors for ITER.....	29
2.5.1	Mechanical errors.....	29
2.5.2	Sources of parasitic signals	31
3	Development of LTCC prototype sensors	37
3.1	Design and testing of Ag LTCC sensors.....	40
3.1.1	Micrographic analysis	41
3.1.2	Electric characterization.....	44
3.1.3	Magnetic characterization.....	49
3.1.4	Thermal characterization	55
3.1.5	Outgassing rate in ITER relevant conditions	66
3.1.6	TIEMF measurements.....	72
3.2	Design and testing of Au LTCC sensors.....	76
3.2.1	Dimensional, density and shrinkage analysis	80
3.2.2	Planarity tests	82
3.2.3	Electrical tests: static and dynamic characterization	83
3.2.4	Magnetic tests: main and transverse equivalent area	87
3.2.5	Thermal conductivity tests along the main direction.....	92
3.2.6	Vacuum out-gassing in ITER relevant conditions	93
3.2.7	Micrographic tests.....	94
3.2.8	Appropriate connection tests on the coil terminals.....	100
3.2.9	TIEMF measurements.....	104
4	Development of pick-up coils built with POZh cable	111
4.1	Insulation withstand voltage	112
4.2	Electric characterization.....	113
4.3	Magnetic characterization.....	117
4.4	Vacuum out-gassing in ITER relevant conditions	119
5	Design proposal of a mechanical and electrical connection system for ITER in-vessel magnetic sensors	121
5.1	Description of the Platform.....	124

5.2	Description of the Support Plate	126
5.3	Thermal Analyses	128
5.3.1	Thermal analyses of new design concept.....	128
6	Conclusions.....	136
7	References.....	138

Introduzione

Nell'ambito delle tecnologie alternative per la produzione di energia la fusione termonucleare controllata appare la più promettente allo scopo di diminuire la dipendenza mondiale dai combustibili fossili quali il petrolio e il carbone. La ricerca sulla fusione mira allo sviluppo di una nuova fonte energetica nel medio termine e dovrebbe trovare ingegnerizzazione nella seconda metà di questo secolo, affiancando le attuali tecnologie.

La ricerca sui tokamak quali JET e ITER e il futuro DEMO, basata sul confinamento del plasma attraverso l'utilizzo di campi magnetici, appare allo stato attuale la più promettente e dovrebbe fornire risultati importanti già nei prossimi due decenni.

Nell'ambito della fusione termonucleare controllata grande importanza rivestono le diagnostiche magnetiche, che forniscono informazioni fondamentali sullo stato del plasma e permettono un controllo attivo sulla posizione e la forma dello stesso.

Questa tesi si occupa dell'ideazione, sviluppo e produzione di due nuove tipologie di sensori magnetici, adatti al funzionamento in ambienti ostili quali l'interno della camera da vuoto (vessel) di ITER. Tali sensori sono stati ideati per resistere ad alte temperature e ad intensi bombardamenti neutronici e dovranno essere installati dietro la prima parete del vessel, a contatto dello stesso. Si tratta di sensori per campi magnetici aventi una frequenza compresa tra 0.001Hz e 10kHz.

La tesi è così strutturata:

- Il capitolo 1 fornisce una visione di massima sul problema energetico e descrive i rudimenti teorici della fusione nucleare
- Il capitolo 2 introduce il problema delle diagnostiche magnetiche elencando i tipi di sensori utilizzati in macchine esistenti (JET, RFX-mod, JT60), con un approfondimento delle problematiche relative ad ITER
- Il capitolo 3 descrive lo sviluppo e la produzione di diversi set di sensori costruiti utilizzando la tecnologia LTCC. Tale capitolo elenca i test e le analisi micrografiche effettuate

- Il capitolo 4 descrive lo sviluppo e la costruzione di una serie di sensori costruiti mediante la tecnologia del cavo avvolto usando cavi in rame con isolamento in fibra di vetro denominati POZh
- Il capitolo 5 descrive il progetto di una struttura necessaria al supporto di tali sensori (LTCC/POZh) all'interno del vessel di ITER

Introduction

In the context of the alternative technologies for energy production, nuclear fusion is the most promising in order to reduce global dependence on fossil fuels such as oil and coal. Fusion research aims at developing a new energy source in the medium term and it should be engineered in the second half of this century, coming alongside the current technologies.

Research on tokamak such as JET and ITER (DEMO in the future), based on the plasma confinement through the use of magnetic fields, is at present the most promising and should provide important results in the coming two decades. In this context magnetic diagnostics are of great importance, providing key information on the confinement of high temperature plasma and allowing an active control on the position and shape of the plasma itself. This work deals with the design, development and production of magnetic sensors, suitable for operation in hostile environments such as the ITER vacuum vessel. These sensors are designed to withstand high temperatures and intense neutron irradiation and have to be installed behind the plasma first wall, in contact to the vessel. These sensors have been built in order to measure magnetic fields having a frequency between 50Hz and 10 kHz.

This work is structured as follows:

- Chapter 1 provides an overview of the energy problem and describes the theoretical basis of nuclear fusion
- Chapter 2 introduces the importance of the magnetic diagnostic in the thermonuclear fusion research and lists the sensors used in existing machines (JET, RFX-mod, JT60), with a focus on the issues related to ITER
- Chapter 3 describes the development and construction of a new type of sensor built using the LTCC technology. This chapter lists the tests and the micrographic analysis carried out upon these new sensors
- Chapter 4 describes the development and construction of a new sensor formed by a copper wire with fiberglass insulation (called POZh) wound on a metallic reel

- Chapter 5 describes the design of the platform necessary to support these sensors (LTCC/POZh) within the ITER vacuum vessel

Acknowledgment

The author Antonio Gallo would like to thanks his family, Giulia Fanin, Prof. G. Chitarin, S. Peruzzo, R. S. Delogu, A. DeLorenzi and all the colleagues at Consorzio RFX Padova.

1 Energy and nuclear fusion

1.1 Introduction

Since the worldwide population is foreseen to grow in the next years the research of new sources of energy is fundamental. This is especially true in the case of the developing countries where people aspire to the standard of living, agricultural productivity and industrialization characteristic of developed countries.

Nowadays the energy demand is covered by oil (41%), gas (22%), coal (16%), nuclear (15%) and renewables (6%), as we can see from Figure 1. It is possible to appreciate how the scenario is currently dominated by fossil fuels.

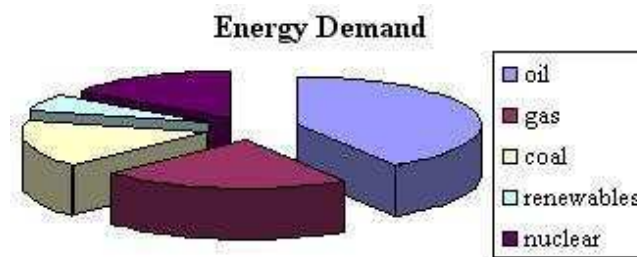


Figure 1: Current Energy Demand

The large increase of CO₂ emissions, due to the traditional fossil fuels, over the last century, is likely to be related to a considerable increase of temperature, resulting in a destabilization of the worldwide climate system. This problem could be partially solved by gradually reducing the use of fossil fuels and increasing the fraction of energy produced by renewable sources, even if the experts agree that they will not be able to satisfy the total demand.

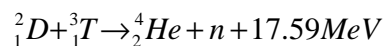
Therefore new energy options must be developed, systems which are optimally safe and environmental and economical friendly. Controlled thermonuclear fusion is one of these rare options. Thermonuclear fusion is not a short-term solution and the first nuclear fusion power plant DEMO (DEMONstration Power Plant) could be operating by 2040. In the present situation, we believe that it is certainly worth to spend resources to explore this option and to develop something useful for future generations.

DEMO is intended to be a prototype power station to be build upon the expected success of the ITER (International Thermonuclear Experimental Reactor) experimental nuclear fusion reactor that will be operating by 2020.

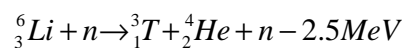
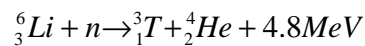
1.2 The nuclear fusion process

The nuclear fusion process consists of forcing together two light nuclei and obtaining a combination whose mass is less than the sum of the masses of the individual nuclei. The decrease in mass comes off on the form of Energy according to the Einstein relationship $E=mc^2$.

In the past years some fusion reactions were individuated to be suitable to get a thermonuclear fusion. The most promising was the one that involves Deuterium and Tritium, isotope 2 and 3 of Hydrogen.



Deuterium can be extracted from sea water by electrolysis. Tritium is very rare and is obtained by the fission reaction of Lithium:



In order to start the fusion reaction it is necessary to overcome the Coulomb barrier, and this is obtained by maintaining the nuclei at a high temperature for a sufficient time and with the proper ion density. The overall conditions, which must be met in order to get more energy than the one required for the heating of the plasma, are usually stated in terms of the product of ion density n_e , confinement time τ_E and temperature T, a condition called Lawson's criterion [2]:

$$n_e T \tau_E \geq \frac{12k_B T^2}{E_{ch} \langle \sigma v \rangle}$$

where k_B is the Boltzmann constant, σ is the fusion cross section, v is the relative velocity, and $\langle \rangle$ denotes an average over the Maxwellian velocity distribution at the

temperature T . E_{ch} is the energy of the fusion products, which, for a D-T reaction, is about 3.5MeV.

For D-T fusion, the temperature where this reaction becomes self-sustaining is equal to $T_{D-T} = 4.5 \cdot 10^7 k$. In order to control the plasma at this high temperature two methods have been developed:

- Inertial confinement
- Magnetic confinement

Inertial confinement is a process where D-T reactions are initiated by heating and compressing a fuel target, typically in the form of a pellet. To compress and heat the fuel energy is delivered using laser beams, ion beams, or X-ray radiation.

In the magnetic confinement approach magnetic fields are used to confine the plasma. The magnetic approach is usually considered more promising for energy production (it is used by the ITER device, see 1.3). Within the nuclear fusion devices magnetic fields are used to contain the charged particles that compose the hot plasma and keep it away from the chamber walls. Magnetic confinement rests upon the property of the charged particles to follow the lines of the magnetic field. By arranging the magnetic fields lines it is possible to “trap” the plasma within the fields. While the plasma is held, it can be heated through a combination of microwaves and particle beams. It can be also heated by the currents flowing through the plasma.

In the next paragraph the ITER project will be presented.

1.3 ITER device

ITER is a is an international tokamak research project to demonstrate the scientific and technical feasibility of fusion power [1] (*Figure 2*). The partners in the project are the European Union, Japan, China, India, Korea, Russia and Usa. The ITER device should obtain some important goals:

- to obtain a gain factor $Q \geq 10$ (where Q represent the amount of thermal energy generated by fusion reactions divided by the amount of external heating). A value

of $Q < 1$ means that the external power is bigger than the power generated by fusion

- to test and verify the future processes and the technology necessary for the DEMO reactor
- to test and develop the possibility to get a tritium breeding from lithium. The lithium should be contained inside the blanket surrounding the plasma.

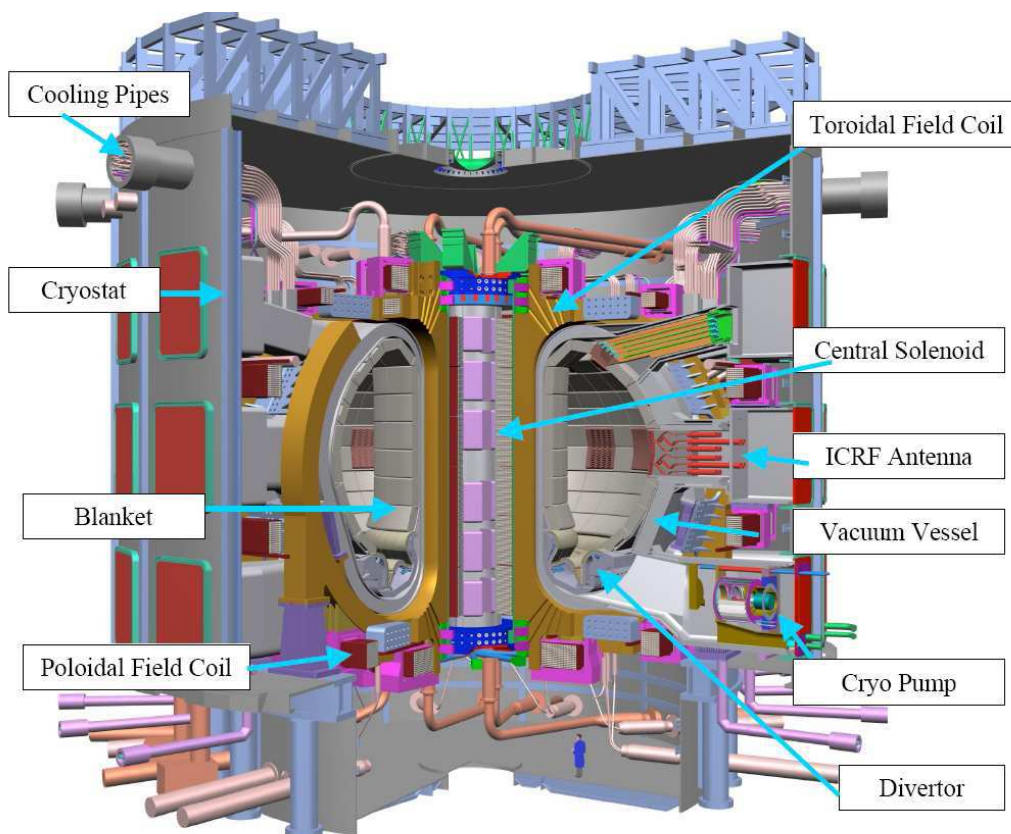


Figure 2: ITER

Table 1 reports the main plasma parameters and the overall dimensions of the ITER device.

Table 1: main plasma parameters and dimensions

Total fusion power	500 MW
Q factor	≥ 10
Average neutron power wall loading	0.57 MW/m^2
Plasma inductive burn time	$\geq 300\text{s}$
Plasma major radius	6.2 m
Plasma minor radius	2.0 m

Plasma current	15 MA
Plasma volume	837 m ²
Plasma surface	678 m ²
Auxiliary heating	73 MW

The main components of ITER are the following:

- magnet and conductor system
- vessel, blanket and divertor system
- plasma diagnostic system
- heating and current drive system
- cryostat system

In the following chapter the ITER magnetic diagnostic system will be described.

2 ITER magnetic diagnostic

The magnetic diagnostic system is fundamental in the context of nuclear fusion experiments such as ITER and JET, because it permits both to measure some of the principal parameters of the plasma and to control in real time its position and shape. The measured and controlled plasma parameters are:

- Plasma current
- Position and vertical speed of the centre of the plasma
- Loop voltage
- Shape of the plasma
- MHD modes
- Halo current distribution

In the following sub-section a brief description is given of the working principles of the in-Vessel magnetic sensors.

2.1 Working principles of magnetic sensors

2.1.1 Pick-up coil and flux loop

The induction coil or pick-up coil (*Figure 3*) is based on Faraday's law: if a loop of wire is crossed by a time-changing magnetic flux φ , then a electromotive force proportional to the rate of change of the flux will be induced in the loop.

$$v = -\frac{d\Phi}{dt} = -\frac{d(\vec{B} \cdot \vec{A})}{dt}$$

where B and A are respectively the magnetic field induction and the cross section of the loop. This equation states that a temporal change in B or the mechanical orientation of A relative to B will produce a voltage. Considering a uniform magnetic field in the volume of the winding, parallel to the sensor axis constituted by a cylindrical coil having area A and N turns, then the inducted electromotive-force is:

$$v = -NA \frac{dB(t)}{dt} = K \frac{dB(t)}{dt}$$

where K is the calibration constant of the coil.

The integration of the voltage measured gives the value of the magnetic field. The winding should be built in such a way that the transversal induction is minimized in order to reduce the spurious signals.

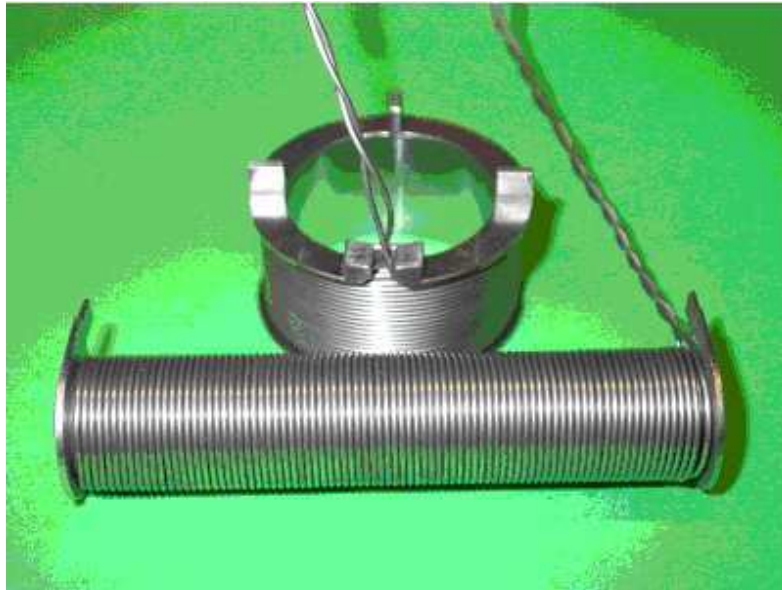


Figure 3: JET tangential and normal pick-up coils

2.1.2 Rogowski coil

Halo currents are produced by the plasma facing the vessel first-wall during the plasma disruptions. These currents, flowing through the vessel and the blanket, are measured by means of Rogowski coils. Rogowski coils are solenoids whose ends are brought around together to form a torus (*Figure 4* and *Figure 5*). Considering a coil of uniform cross section A, with constant turns per unit length n, and assuming that $\frac{\nabla B}{B} \ll n$ (the magnetic field varies little over one turn spacing), the total flux linked by the coil is:

$$\Phi = n \oint \int dA \bar{B} \cdot \bar{dl}$$

where dl is the line element along the solenoid axis.

According to the Ampere's law the integration of a magnetic field along a path gives:

$$\oint_l \vec{B} \cdot d\vec{l} = \mu I$$

where I is the total current encircled by l and μ is the magnetic permeability of the medium. Thus:

$$\Phi = nA\mu I$$

and the voltage out of the Rogowski coil is:

$$v = \frac{d\phi}{dt} = nA\mu \frac{dI}{dt}$$

which integrated gives a signal proportional to I .

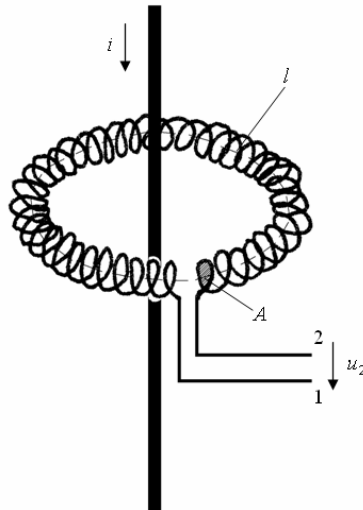


Figure 4: simplified scheme of a rogowski coil

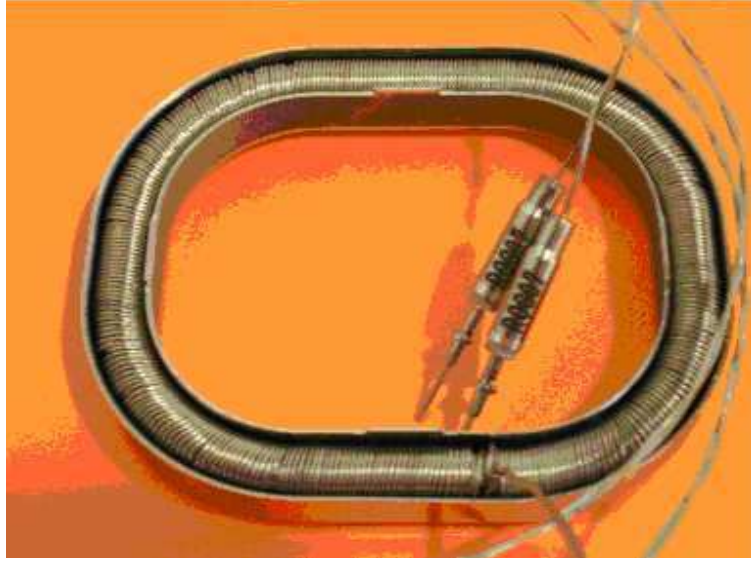


Figure 5: JET halo rogowski coils

2.1.3 Hall sensors

Hall sensors are solid state voltage generators which provide an output electromagnetic force (E.M.F.) proportional to the magnetic flux density. Contrary to the other sensors above described, Hall sensors do not require any time-integration of the output signal and in principle appear to be suitable to be used for steady-state sensors. The Hall sensors have been used in the present machines (JET), however their radiation hardness is limited.

The active part of Hall sensors is made of semiconductor materials. In fact the E.M.F. is proportional to the mobility μ of the charge carriers available in the material, which can be made very high. The semiconductors mainly employed are: Si, Ge, GaAs, InAs, InSb. In the following a basic physical principle of the Hall effect is described. Considering bar-shaped semiconductor (**Figure 6**), we assume that a constant current I flows along the y -axis from left to right in the presence of a z -directed uniform magnetic field. Electrons, subjected to the Lorentz force

$$\vec{F}_L = q \cdot (\vec{v} \times \vec{B}) = q \cdot \vec{E}_L$$

initially drift away from the current line toward the negative x -axis, resulting in an excess of charges which produces a transverse voltage equal to:

$$v_{HALL} = \left| \vec{E}_L \right| \cdot a = v_z B_y a$$

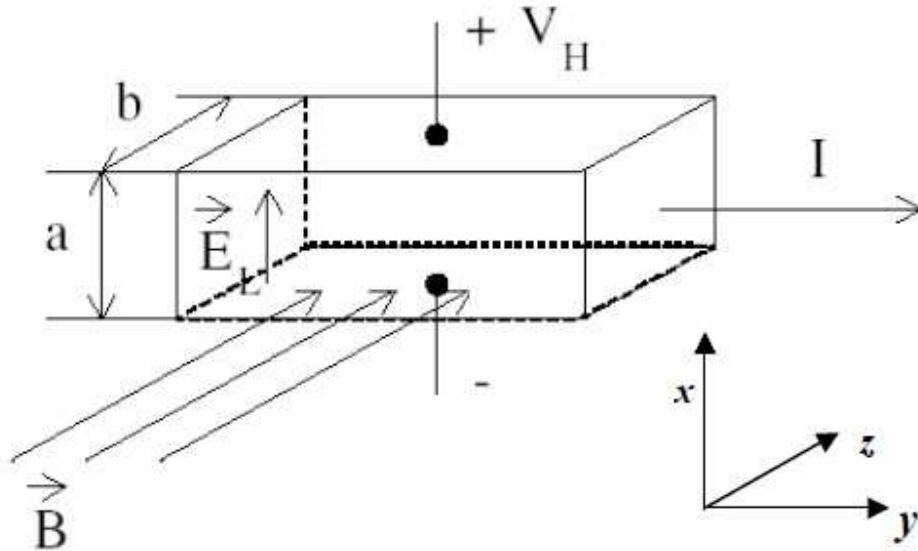


Figure 6: basic principle of the Hall effect

Introducing the current density $J=nqv$, we can write:

$$v_{HALL} = \frac{JB_z a}{nq} = \frac{IB_z}{nab}$$

The Hall voltage V_{Hall} depends on the mobility $\mu=1/na$ of the carrier density, on the resistivity ρ of the material and on the dimension of the bar-shaped semiconductors, so we can write:

$$V_H(t) = \frac{\mu\rho B(t)I}{b} = kB(t)I$$

where k is the sensibility of the hall sensor.

2.2 Implementation of In-Vessel pick-up magnetic coils on existing devices

The magnetic diagnostic follows the same general principles in all experimental machines, but their electrical parameters (inductance, resistance, bandwidth etc.), mechanical dimensions, number and topological layout are instead peculiar of each

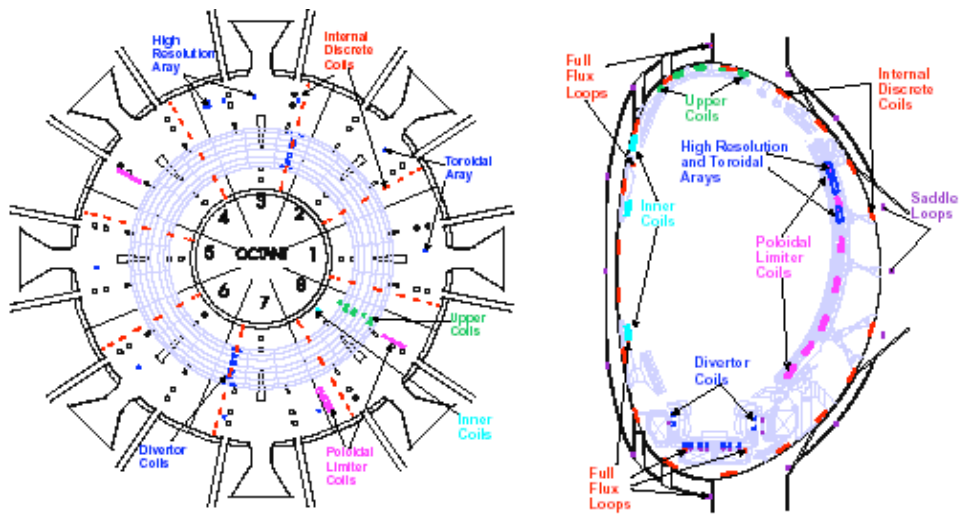
machine. In most of the existing devices the in-Vessel magnetic system consists of arrays of pick-up coils made with mineral insulated conductors (MIC).

In the following subsections the sensors installed in some representative machines are described.

2.2.1 JET

The magnetic diagnostic system operating in JET (*Figure 7*) consist of [18] [19] [20] [29] [30] [31]:

- Internal Discrete Coils: 18 tangential coils fitted against the in-Vessel wall of each octant (except Octant 8, which has only 9 bottom coils). There are 135 coils in total.
- Divertor Coils: 11 pairs of coils \times 2 octants = 44 coils (installed in 1996) in Divertor region, of which 22 coils are currently faulty plus 7 pairs of coils \times 2 octants = 28 coils (installe in 2005) in Divertor region, of which 1 coil is currently faulty.



In Vessel Probes

2 arrays of probes at the inner octants 8-1, 4-5 (blue); 2 arrays of divertor coils (red)

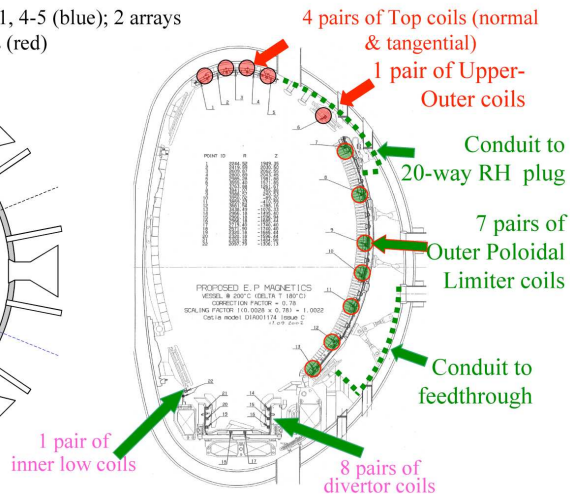
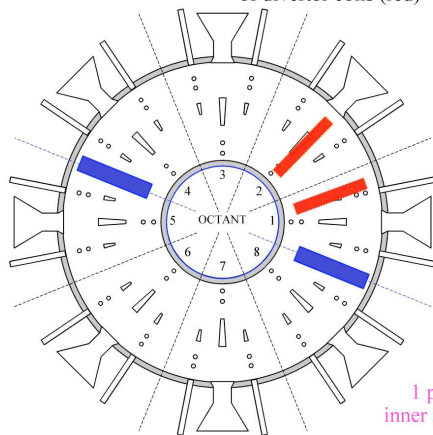


Figure 7: poloidal and toroidal distribution of the original JET magnetic sensors (top) and distribution of the new in-Vessel sensors (bottom) [18]

In **Figure 7** it is possible to see the toroidal and poloidal position (original and new) of the magnetic sensors.

The normal and tangential coils of JET are constituted by an even number of layers of mineral insulated cable of 1 mm outer diameter, wound around an Inconel 600 former (**Figure 3**). The sheath of the mineral cable is also made of Inconel 600, the insulation material is high purity magnesia and the inner conductor is Chromel (90% Nickel, 10% Chrome).

2.2.2 RFX-mod

In RFX-mod a new system of magnetic sensors has been installed inside the vacuum Vessel in order to study both the effects on the plasma and the MHD mode response to the action of the external active coil system [21]. The system consists of 116 toroidal pick-up coils, 15 poloidal pick-up coils and 8 saddle probes. The pick-up coil (18x18x4.5mm) (*Figure 8*) is installed below the graphite tiles. The winding, wound in two layers around a ceramic support (MACOR), is made of a mineral insulated cable.

The characteristics of magnetic sensors of RFX-mod are reported in the *Table 2*.

Table 2: principle characteristics of the magnetic sensors of RFX-mod

Parameter	Tangential coil		Normal coil	
	Value	Comments	Value	Comments
Type of wire	MIC	MgO (99.4%)	MIC	MgO (99.4%)
Insulated conductor Outer Diameter	0.254 mm		0.635 mm	
Bare conductor diameter	0.076 mm	Chromel P	0.165 mm	Nickel-clad copper
Wire sheath thickness	0.051 mm	Inconel 600	0.076 mm	Inconel 600
Insulation thickness	0.038 mm		0.16 mm	
Number of layers	2		1	
Number of turns	80			
Rc	3.7 Ohm/m	Cu	0.8 Ohm/m	
Withstand Voltage	400 V		1000 V	
Frequency response	400 kHz		> 10kHz	



Figure 8: new coil of RFX-mod

2.2.3 JT-60 Upgrade

The characteristics of the tangential and normal coil for plasma equilibrium study are reported in the *Table 3* [22] [23] while in *Figure 9* their poloidal positions are shown.

Table 3: parameters of the tangential and normal equilibrium coil

Parameter	Tangential coil	Normal coil
Material of coiling wire	Ceramic coated Pt wire (diameter=0.2mm)	Ceramic coated Pt wire (diameter=0.2mm)
Sheath	Inconel	Inconel
Working temperature	< 500 °C	< 500 °C
Cross section	0.32 m ²	0.58 m ²
Frequency response	< 10 kHz	< 10 kHz

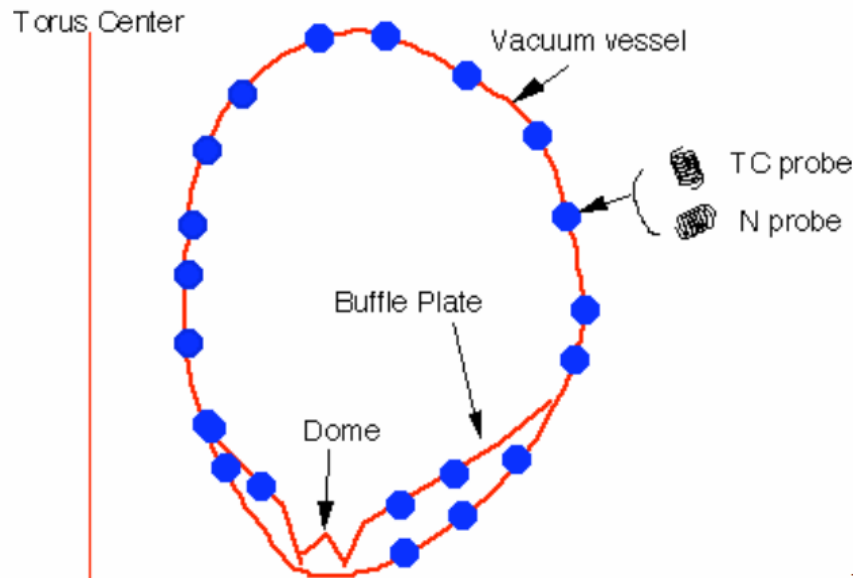


Figure 9: poloidal position of tangential and normal coil

2.3 ITER in-Vessel magnetic sensors

The ITER in-Vessel system includes:

- tangential, normal and toroidal equilibrium coils mounted on the inner surface of the VV
- tangential high frequency coils mounted on the inner surface of the VV
- complete and partial flux loops mounted on the inner surface of the VV

- MHD-dedicated saddle loops mounted on the inner surface of the VV
- a (temporary) PF and TF error field measurement assembly

These coils are installed in a hostile environment due to radiation, high temperature and stray magnetic field. All these phenomena can seriously degrade the performance of the measurements or bring to the sensor failure. For this reason, given also the difficulties with maintenance, the magnetic system must be designed with sufficient redundancy by foreseeing some layers of backups to minimize the need for maintenance, without precluding it. In ITER, critical systems have been designed with a primary and secondary measurement set which can be used to measure the same plasma parameters or to improve the measurement accuracy by giving more data. In **Figure 10** and **Figure 11** the ITER poloidal and toroidal magnetic sensors distribution is shown for the in-Vessel sensors. The tangential and normal coils are used for the reconstruction of the shape of the plasma, of the plasma current, and of the low MHD modes.

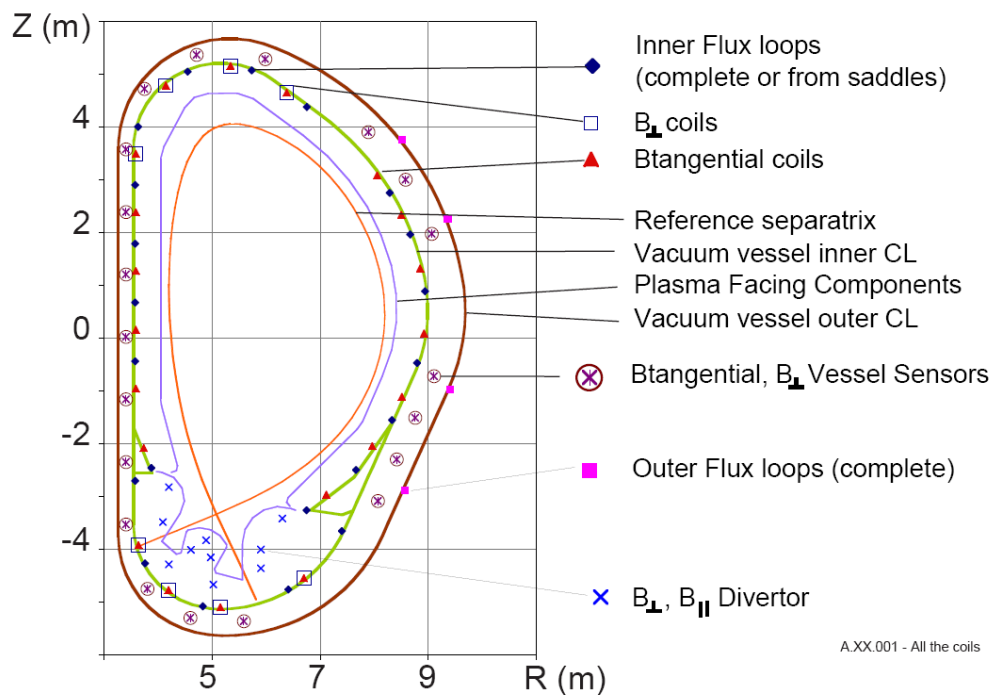


Figure 10: ITER poloidal distribution of magnetic sensors

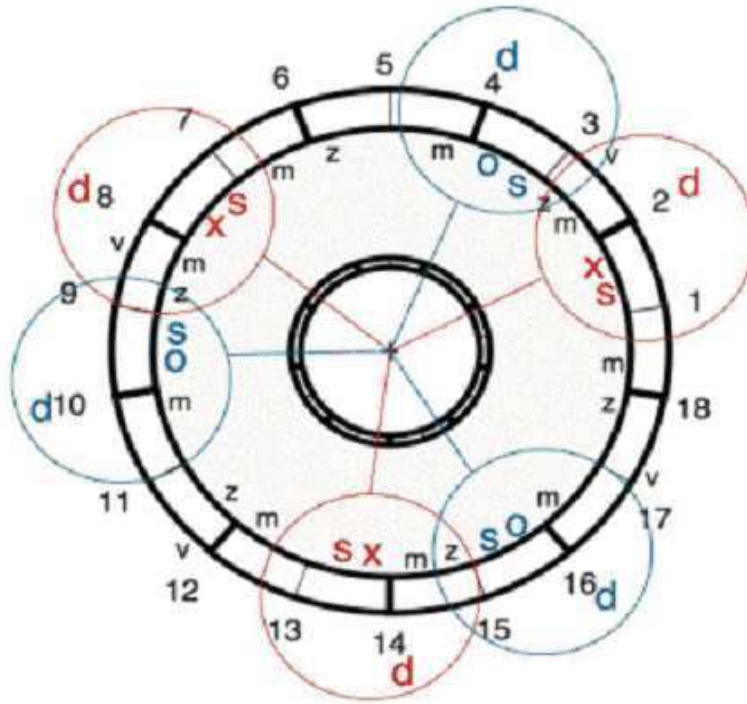


Figure 11: ITER toroidal distribution of magnetic sensors

2.4 Description of previous design of ITER tangential and normal coils

The in-Vessel tangential and normal coils will be installed behind the blanket modules positioned in a cut-outs (100mm x 50mm) provided near the corners (*Figure 12*) to avoid interaction with the plasma current. The poloidal and toroidal distribution of the coils are reported in *Figure 10* and *Figure 11*.

The previous design [17] has been obtained as an optimization of electrical and mechanical constraints and radiation effects in order to guarantee the coil performance. The principal constraint for the coil design is the maximum temperature and the thermal gradient induced by the neutron loads on the different material assuming that the sensor can cool itself only for conduction through the vacuum Vessel, considered isothermal at the temperature of 140°C. The principal characteristics of these sensors are reported in *Table 4*.

Table 4: Coil parameters for the tangential and normal coils

	Tangential coil	Normal coil
--	-----------------	-------------

Parameter	Value	Comments	Value	Comments
Type of wire	MIC	MgO Al ₂ O ₃	MIC	MgO Al ₂ O ₃
Insulated conductor Outer Diameter	1.6 mm		2.0 mm	
Bare conductor diameter	0.75 mm	Cu	1.0 mm	Cu
Wire sheath thickness	0.325 mm		0.5 mm	
Insulation thickness	0.1 mm	Stainless Steel	0.1 mm	Stainless Steel
Number of layers	6			
Number of turns	300			
Magnetic effective area	0.273 m ²		0.3 m ²	
Coil length	80.8 mm			
Former outer diameter	24 mm			
Rc	2.9 Ohm	Cu		
E _{max} @ 100 T/s	88kV/m			
Frequency response	> 10kHz		> 10kHz	

The winding, realized in 6 layers with a MIC wire, is wound on a central tube in stainless steel attached to the vacuum Vessel. In order to limit the temperature gradient the two following components have been added (*Figure 12*, *Figure 13* and *Figure 14*):

- a heat conducting copper bar welded on the central tube. This bar is slitted in order to reduce the eddy currents
- a cooper felt strip between each winding layer

The thermal analyses performed by a finite elements code show that the maximum temperature is 240°C (*Figure 16*) while the maximum temperature drop is about 100°C.

The tangential and normal coils can be permanently fixed (hardwired) on the vacuum Vessel or replaceable by remote handling. In the first case the mineral insulated cable of the coil winding is brought to a set of connectors within the upper port without other intermediate connections; in the second case a removable connection, made by two spot welded junctions, is made near to the coil.

Figure 15 shows the previous mechanical and electrical connection system for the magnetic sensors inside the ITER vessel. The device has been completely (see section 5) re-designed since it was not suitable for remote handling operations.

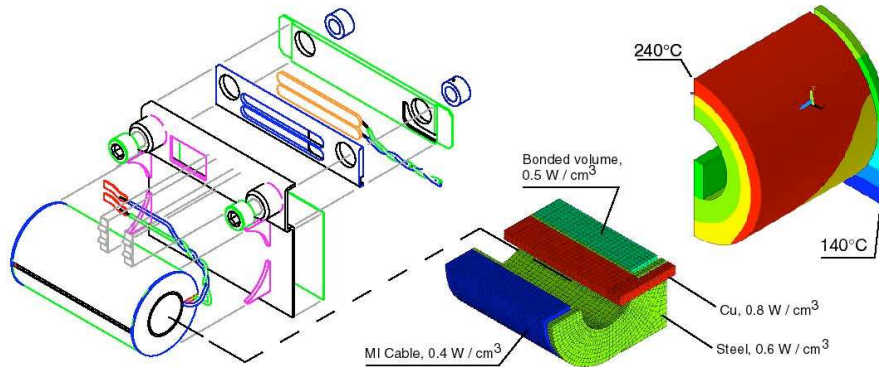


Figure 16: Temperature distribution within the coil during burn. [16]

In the following sections the design, development and constructions of two new types of in-Vessel pick-up coil sensors, LTCC sensors and POZh sensors, will be presented.

2.5 Challenges in the construction of in-Vessel magnetic sensors for ITER

Many sources of error can compromise the reliability of the magnetic fields measurements inside the ITER vacuum vessel, as for example temperature gradients and neutron and gamma ray radiation, misalignments of the sensors and electronics inaccuracies. According to [11] a total target error of error of $\pm 0.7\%$ with 95% confidence (0.35% r.m.s) has been specified for the in-Vessel equilibrium tangential normal pick - up coils in order to permit to reconstruction of the plasma shape.

A list of all the possible sources of error is presented in the following.

2.5.1 Mechanical errors

2.5.1.1 Static mechanical errors

Static mechanical errors can be considered constant during plasma operation. They can be so classified:

- installation errors
- errors of the coil winding
- misalignments when the device is at operating temperature and low pressure

According to the ITER Design Description document [DDD_2001, pag 11], the positioning errors are assumed to be less than $\pm 1\text{mm}$ (over 6 m) and the orientation errors less than $\pm 0.5^\circ$ for both normal and tangential pick-up coils

Also, the manufacture of the coil winding can be inaccurate owing to either a mechanical error of the support of the winding or the difficulty to wind more layers guaranteeing a perfect alignment with respect to the normal direction of the magnetic field to be measured.

2.5.1.2 Mechanical errors due to electromagnetic forces

Due to the Lorentz force, the eddy currents and Halo currents flowing in the metallic structure and in the blanket can produce a vacuum Vessel deformation up to 2 mm during plasma disruption events. This could produce a misalignment of the sensors fixed on the Vessel.

2.5.1.3 Mechanical errors due to thermal expansion

Temperature variations during plasma operations produce variations in the dimensions of the Vessel and of the pick-up coil structure, resulting in a displacement of the sensor itself and in a change of orientation. This error might be estimated using a suitable thermo-mechanical model for the Vessel, but does not seem to be critical since the orientation change is typically small.

2.5.2 Sources of parasitic signals

2.5.2.1 Effect of electro-mechanical environment, transverse field and eddy currents

During the non-stationary phases of the plasma pulse (in particular during a disruption event) a magnetic flux variation is produced which induces eddy currents in all the surrounding structure (e.g. vacuum Vessel). The magnetic sensors measure the actual field configuration at their specific locations, including the effects of the eddy currents in all the metallic structures. However, if the influence of local eddy current in the metallic structures located close to the sensors is not negligible, the magnetic field measurement could be not exactly representative of the global configuration. Since the measurements are to be used for the reconstruction of the global magnetic plasma configuration by means of numerical codes, these local effects should be evaluated or compensated before using the signals. Other measurement errors related to spurious signals are:

- Sensitivity to the transverse magnetic field due to the errors of the coil winding
- Stray pickup area of twisted conductors, connectors and the distance of the ends of the coil winding.
- Using wires made of uniform material

The calibration accuracy can be $\approx 0.1\%$ using a precise and stable AC magnetic field source.

2.5.2.2 Effects of radiation

Neutron and γ -ray radiation can produce some spurious output signals that could compromise the accuracy of the sensor. In the case of ITER in-Vessel magnetic sensors the most critical effects are the following:

RIC effect

The neutronic and γ ray radiation excite the isolated electrons which charge the sensor during the impulse modifying the output signal, resulting in a modification of the electrical conductivity of the sensor. The RIC effect depends on:

- Purity of the isolation
- Shape of the isolation

In Figure 17 we can see the variation of the conductivity of different types of cable as a function of the radiation dose.

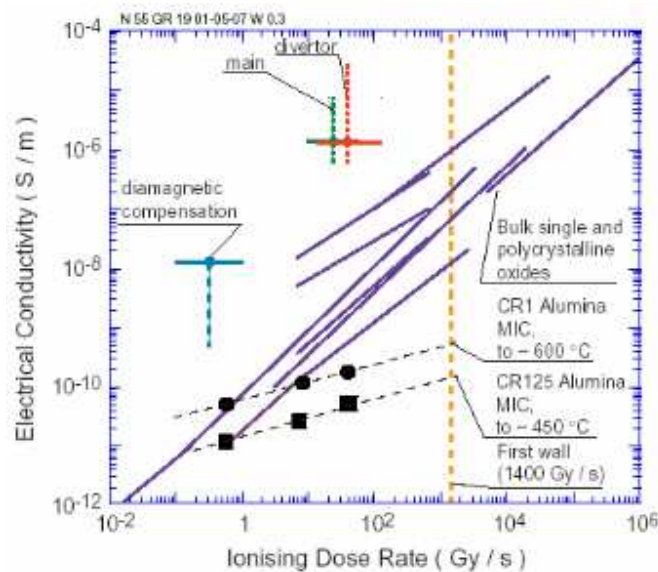


Figure 17: variation of the conductivity of different types of cable as a function of the radiation dose

RIEMF effect

Neutronic and gamma ray radiation induce currents between the sensor wire and surrounding structures including mineral insulated cable (MIC) sheath and blanket structure. The dominant mechanism depends on:

- Geometry of the sensor
- Insulating material
- Composition of the metals
- Gamma and neutron spectra
- Time of activation

Some precaution can be adopted in order to reduce the RIEMF effect as indicated in [25], [26]:

- Minimize the effect of temperature and radiation field asymmetries by adopting an even layer coil structure
- Optimize the diameters of the core and sheath
- Keep a minimum insulator thickness
- Reduce the non-uniformity (density) of the insulator over the cable diameter
- Minimize integrator sensitivity to common mode voltage by lowering its input impedance

The strong neutron and γ ray radiation also produces degeneration in the materials that form the sensors, cables and insulators, and this is one of the most difficult long term problem to solve. Some effects of radiation are:

- The material become brittle
- The corrosion resistance usually decreases
- A decrease of the mechanical resistance of the materials

Insulators are far more sensitive to radiation damage than metals and the following properties could change under the effect of radiation:

- Electrical conductivity
- Dielectric loss
- Permittivity
- Optical absorption (+ emission)
- Thermal conductivity
- Mechanical properties

2.5.2.3 Effects of temperature gradients inside the sensor

TIEMF effect

The TIEMF effect is the presence of a parasitic voltage induced by thermal gradients inside the sensor. This undesired voltage can strongly affect the measurements of the magnetic fields inside the ITER vacuum vessel because of the drift produced during long integration time. This effect is probably with the R.I.E.M.F. effect the main and dominant cause of errors for the magnetic measurements of ITER, for pulse length longer than 100 seconds. Some suggestion can help to reduce all the negative effects of TIEMF

- Decreasing the thermal gradients
- Improving the cooling and the wiring of the coils

TIEMF effect upon LTCC sensors is examined in the following sections.

2.5.3 Signal drift integration

For long pulse machine the measurement becomes sensitive to very small parasitic voltages that, when integrated, can give rise to unacceptable errors signals. These voltages can arise due to radiation-induced (RIEMF) or thermoelectric-induced (TIEMF) electromagnetic force between coil winding and surrounding structures.

Digital integration can't guarantee the requested accuracy over a long time integration, more than 1 hour in the case of ITER. In this scenario a time-reliable analogical integration method has to be used.

In order to evaluate the electronic error the Tore Supra integrator [27] has been considered . The tests results, carried out with toroidal and poloidal fields and without plasma current in - situ of Tore Supra, shown an average drift of 1.36 mVs after 1000s. Some considerations can be done:

- the integrator proposed in the [27] owing to the absence of input stage differential amplifier, in order to reduce the noise to the input of the integration stage due to this electronic component, makes the conditioning electronic little immune to the common mode voltage.
- The presence of plasma current could increase the noise picked up from the coils and the wiring and make worse the performance of the integrator. According to [

28] (p. 76) the integrator drift can be assumed to be $1 \mu V s / s$, which seems to be good enough for most magnetic measurements. According to the same report [28] (p. 76), the effect of the common mode can be disregarded because the "integrator board is electrically isolated from the ground". The latter assumption seems to be too much optimistic.

	Error source	Percentage error
(A)	Angular misalignment	0.1%
(B)	Error coil to coil	0.1%
(C)	Errors due to stray area	<0.1%
(D)	Radiation error evaluated per 1000s (assuming constant drift for 1000s)	Tangential coil = 0.3% Normal coil = 0.4%
(E)	Winding size variation due to the temperature	0.1% (thermal gradient of 20°C)
(F)	Electronic error evaluated per 1000s	Tangential coil=0.4% (worst case: $1.36mVs/0.35Vs$)*100 = 0.4% Normal coil = 0.5%
	Total error	~ 1.2%

Table 5: estimated total error for the in-Vessel pick-up coils

As shown in **Table 5** an optimistic error of 1.2% has been obtained. This value could be larger principally due to other radiations effect and parasitic voltage introduced by the cable transitions which should be realized in the path from coil to the conditioning electronic. This error is larger than total target error (0.7%) requested for an optimal reconstruction of the plasma position. In our opinion it is very difficult to reach this goal and so alternative hypothesis should be considered in order to reduce the differential and common mode noise to the input stage of the electronic conditioning. In the following some solutions are proposed:

- To build two coils for each position wrapped in the opposite direction. In this way it will be possible to reduce the noise by subtracting the two signals.

- To add a hall sensor (if it is radiation compatibility) close to the magnetic coil. In this way the coil signal should be integrated from a frequency of some kHz, which would permit to reduce the low frequency noise.

In spite of two solutions described above, further assessment should be done about the feasibility to obtain the same plasma position error by means of more robust reconstruction code, which permits to have a higher measurements noise level. This would permit to have larger safety margin with respect to the real error of the signal measured.

2.5.4 Errors due to temperature variation

Temperature variation due to neutron radiation increases the winding size and this could lead to not-negligible variation of the calibration constant of the sensor.

As described in the following sections new types of sensors have been built and tested in order to comply with ITER requirements.

3 Development of LTCC prototype sensors

The design and development of in-Vessel magnetic sensors is critical since these sensors are placed in a hostile environment with strong neutron radiation and frequent heat loads. This cause undesired effects such as TIEMF that produce spurious voltages that affect the accuracy of the sensor.

High Temperature Co-fired Ceramic (HTCC) and Low Temperature Co-fired Ceramic (LTCC) technologies have been used in special purpose electronic applications such as aerospace, telecommunication and defense for several years [3]. Both technologies can be used in order to produce compact and reliable pick-up coils constituted by a stack of superimposed ceramic layers with printed metallic circuits, high-pressure laminated and fired in one or more steps. Metallic lines on different layers are connected by metallic "vias". Thick film HTCC are made of alumina layers with refractory metallization (tungsten or molybdenum), pressed and co-fired at 1500°C. A uniform and reliable dielectric isolation can be obtained, but the use of refractory metal implies high resistance and requires complex and expensive processing. On the other hand, LTCC is characterized by a relatively low firing temperature (850°C) which makes it compatible with high electrical and thermal conductivity metals (Ag, Au, Pd) for the conductive lines.

However, mainly because the lower conductor resistance makes the reduction of the noise due to neutron radiation possible, it was decided to proceed with the construction of some sensor prototypes based on LTCC technology (*Figure 18*).

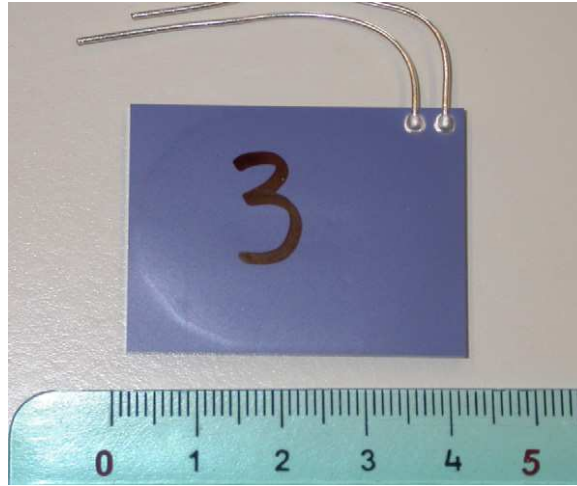


Figure 18: 10-layer LTCC sensor having Ag internal conductors and HERATAPE® CT 700 ceramic substrate

LTCC pick-up coils have an outstanding dimensional and mechanical stability, a good thermal conductivity and a fine line pattern. These sensors should also guarantee increased radiation hardness and Signal/Noise ratio with respect to the standard pick-up coils made with Mineral Insulated Cables (MIC). They are also compact, highly reliable and have an increased main/transverse magnetic area ratio. **Figure 19** and **Figure 20** show the disposition of the internal conductive lines of the sensor.

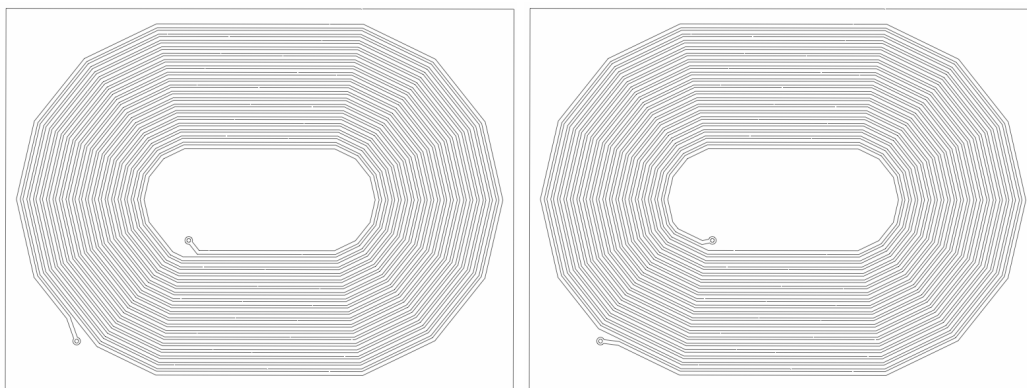


Figure 19: scheme of an LTCC internal circuit: odd layers (left) and even layers (right)

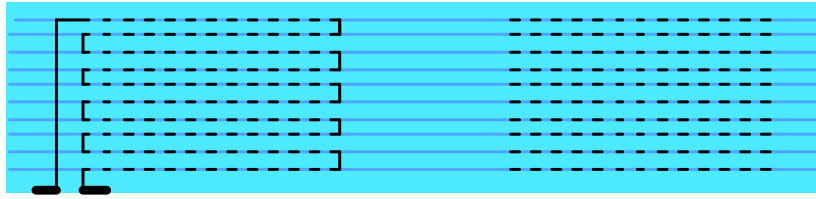


Figure 20: internal layers disposition

The design parameters and reference requirements for the LTCC prototype sensors are summarized in **Table 6**.

Table 6: Initial design requirements of LTCC pick-up coils.

Magnetic sensor equivalent area	0.3m ² (optimal), 0.1m ² (min.)
Electrical resistance	100Ω (optimal), 500Ω (max.)
Sensor size (transverse to field direction)	40mm×30mm (max.)
Substrate material	Alumina
Conductive lines material	Ag or Au
Number of layers	10–40
Normal operating temperature	200 °C
Max. tolerable temperature	500 °C
Max. expected voltage between terminals	30V

Different sets of LTCC sensors have been built and tested since 2007 in order to test different materials for both the conductive lines and the ceramic substrate, as indicated in Table 7. In the development and construction of these prototype sensors several specific precautions have been taken regarding non-uniform shrinkage during firing, misalignment of layers, non-uniform thickness of conductive lines and stray magnetic areas, since the number of layers required for obtaining the equivalent area required is larger than that usually produced with LTCC technology .

At the same time, the issues related to the behavior at high temperature in vacuum, compatibility of ceramic components with radiation (exact composition of ceramic is proprietary information of Heraeus and DuPont) and on metallic conductive lines have been taken into consideration.

Table 7

Description	Quantity	Dimensions [mm]	Number of layers	Terminal wires material	Ceramic material

Ag 10 layer sensors	6	40x30x3	10	Ag	Heraeus CT700
Au 10 layer sensors	3	40x30x2.7	10	Au	DuPont 951
Au 30 layer sensors	7	40x30x6.8	30	Au	DuPont 951
Au 40 layer sensors	1	40x30x9	40	Au	DuPont 951

3.1 Design and testing of Ag LTCC sensors

The first set of LTCC sensors, procured by Consorzio RFX through an industrial supplier (Linkra <http://www.linkra.it>) at the beginning of 2008, was formed by 6 pick-up coils with 10 silver conductive layers printed on HERATAPE® CT 700 ceramic substrate (*Figure 18*).

The following tests have been carried out upon the Ag LTCC sensors:

- electrical tests: measurement of inductance, resistance, parasitic capacitance, measurement of magnetic area along main and transverse direction (at various frequencies)
- dimensional test, SEM-EDS analysis of sectioned sensors, x-ray imaging
- thermal conductivity tests
- outgassing rate in ITER relevant conditions
- TIEMF measurements

The set of 6 prototype sensors (*Figure 18*) with Ag internal conductors was built according to the design described in *Table 8*.

Table 8: design parameters of the first LTCC sensor prototypes

number of ceramic layers	11
number of conducting layers	10
turns/layer	20
layer thickness	300 micron
outer dimensions	40 mm x 30 mm x 3 mm
conductor layout	Elliptic
conductor line width	400 micron
conductor line thickness	10-20 micron
inter-line insulation	200 micron
ceramic material	Heraeus CT700

conductor material	Ag
electrical resistance	50 Ohm

Ag LTCC sensors have the following nominal dimensions: 30 x 40 x 3 mm

3.1.1 Micrographic analysis

The geometry of the prototype sensors has been verified using x-ray imaging (Figure 21) and also micrographic images of sectioned sensors (*Figure 22*), showing that the tolerance in the positioning of the conductive lines and vias is sufficient to ensure a reliable connection of the different layers.

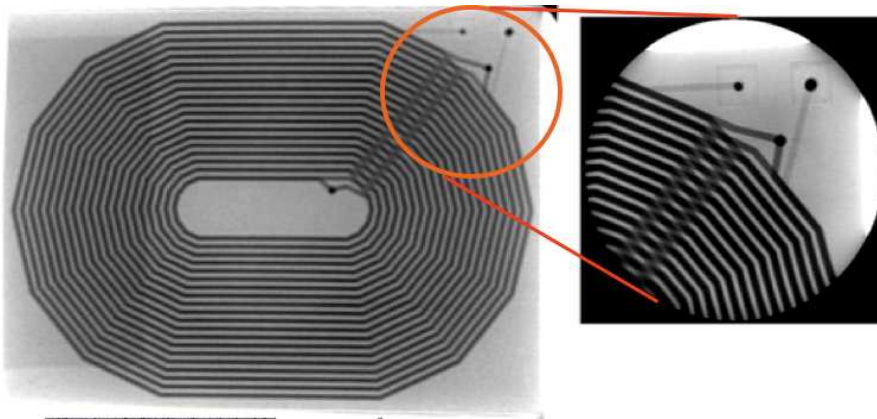


Figure 21: x-ray picture of the Ag LTCC sensor prototype showing the actual layout of conductor connections

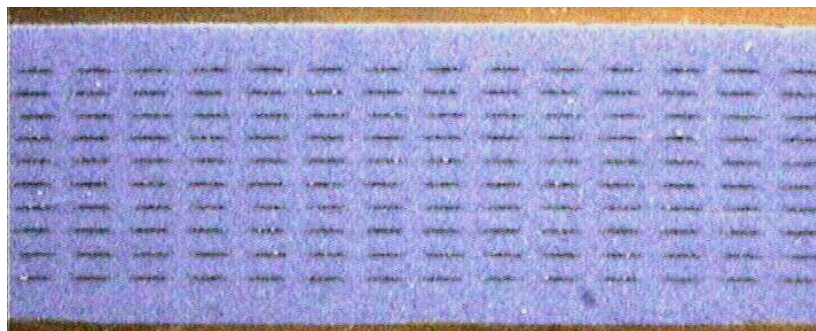


Figure 22: Ag LTCC sensor cross-section

Table 9 displays the cross-section characteristics of 10-layer Ag LTCC sensors.

Table 9: characteristics of 10-layer Ag LTCC sensor cross-section

Number of layers	10
------------------	----

Number of turns per layer	20
Offset between layers	485 μm
Layer thickness	200 \pm 5 μm
Distance between conductive lines	195 \pm 5 μm
Thickness of conductive lines	19 \pm 2 μm
Width of conductive lines	400 \pm 5 μm

SEM-EDS analyses have been carried out in order to characterize the ceramic and the conductors of the LTCC sensors. The Heraeus CT700 ceramic is a mixture of alumina and silica glass, containing small percentage of Pb and Ca, and small percentage of BaO, CoO, SrO. Exact compositions are proprietary, but the ceramic seem to be compatible with ITER requirements. **Figure 24** and **Figure 25** show the compositions of the Heraeus CT700 LTCC ceramic used as substrate material for the Ag LTCC sensors while **Figure 26** shows the composition of the metallic lines of the sensors. It's possible to appreciate the presence of BaO, CoO, SrO.

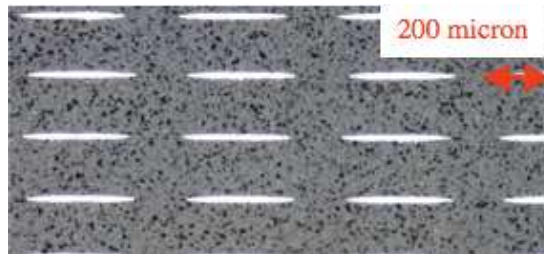


Figure 23: SEM picture of sensors cross-section showing the positioning of the conductor lines.

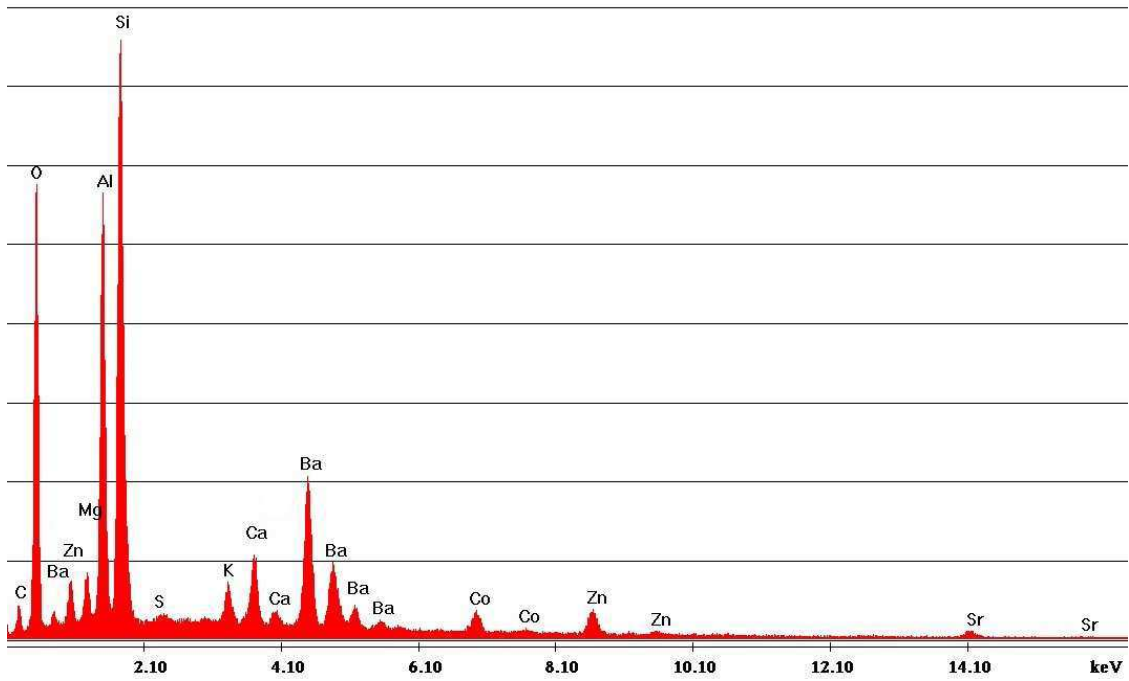


Figure 24: Composition of Heraeus CT700 ceramic

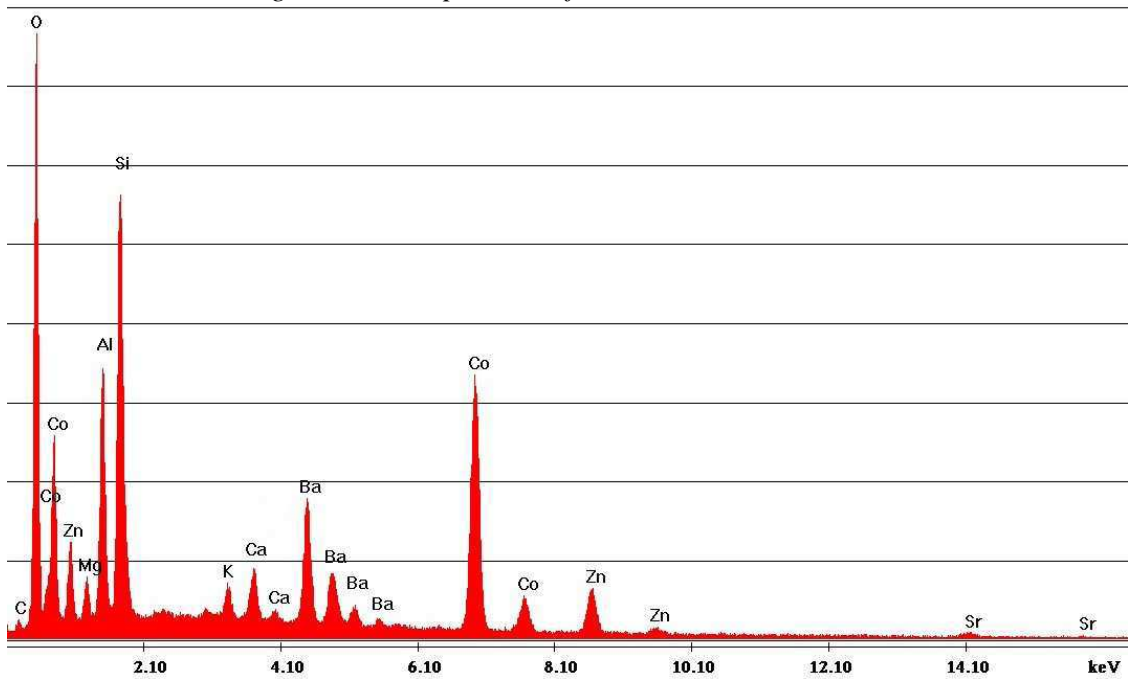


Figure 25: compositions of metallic inclusions

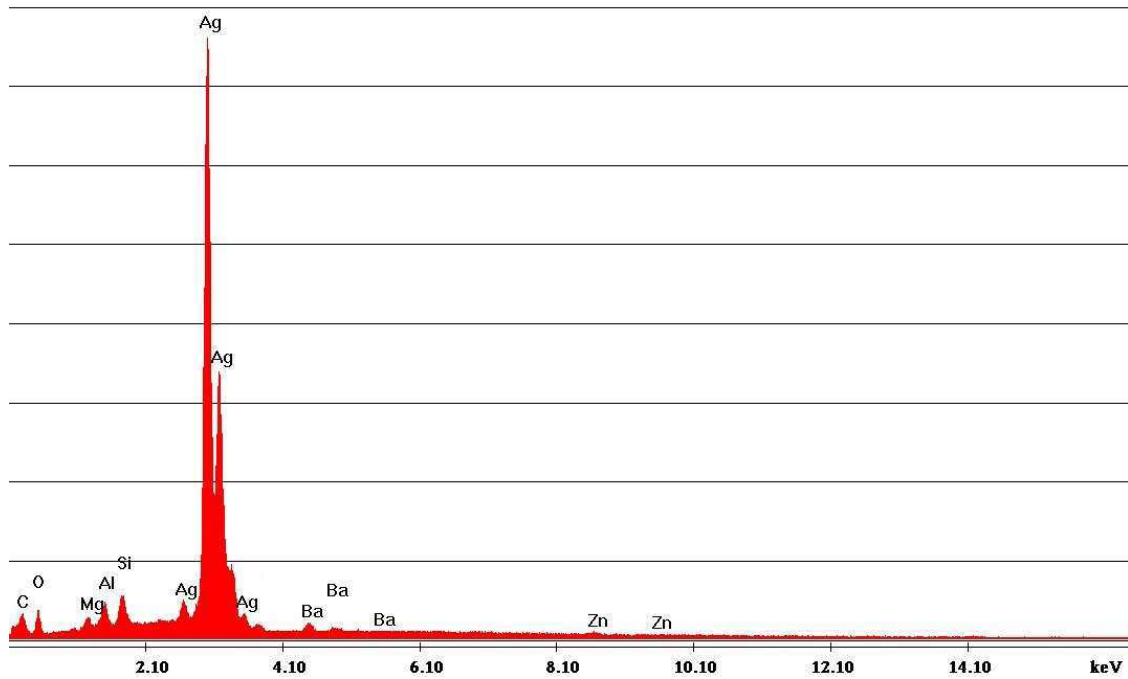


Figure 26: composition of sectioned Ag metallic lines

3.1.2 Electric characterization

Both static and dynamic electric tests have been carried out on each LTCC sensor in order to find out important parameters such as the insulation withstand voltage (dielectric strength), the static resistance, the equivalent inductance and capacitance, the resonance frequency and the bandwidth.

3.1.2.1 Insulation withstand voltage

The insulation withstand voltage was measured by grounding the outer surfaces of the LTCC sensor with two aluminum plates (*Figure 27*) and applying a voltage up to 5kV between one terminal and the plates (*Figure 28*). The measurements have been carried out by means of two different instruments, the SATURN-ISO LEM in the range 100-1000V and the ABB METRISO 5000 in the range 2500- 5000V. The breakdown voltage was found bigger than 2500 V for all the sensors. A surface discharge has occurred at 5000 V.

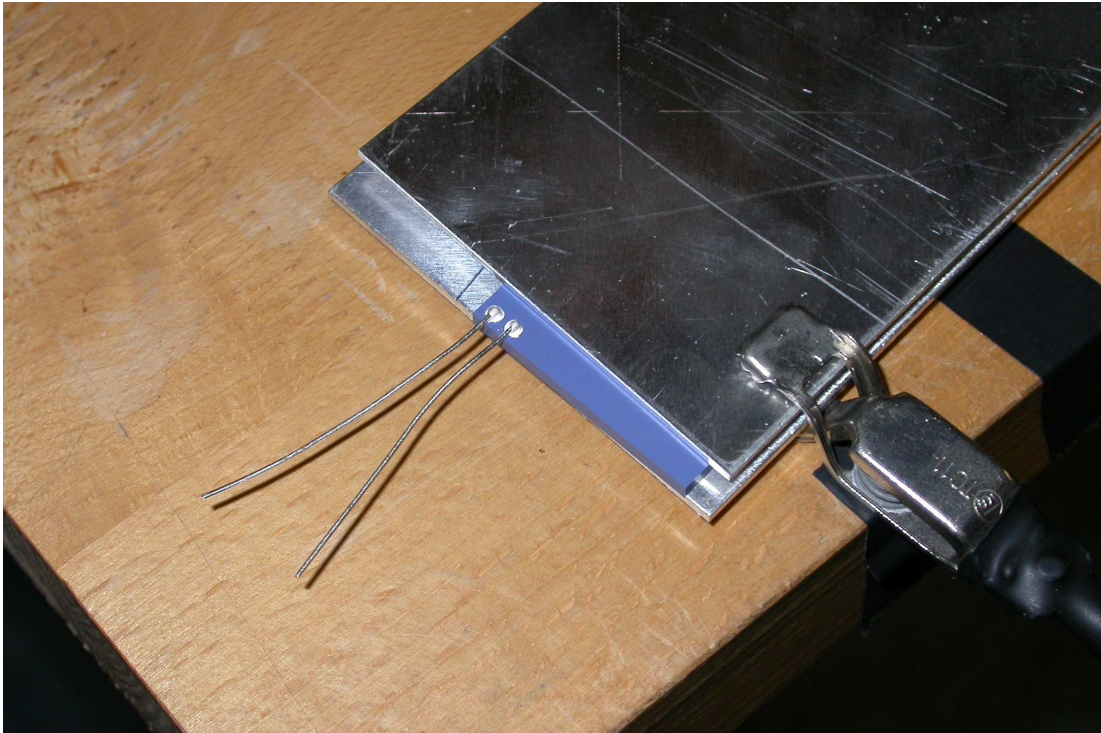


Figure 27: LTCC sensor between two aluminum plates

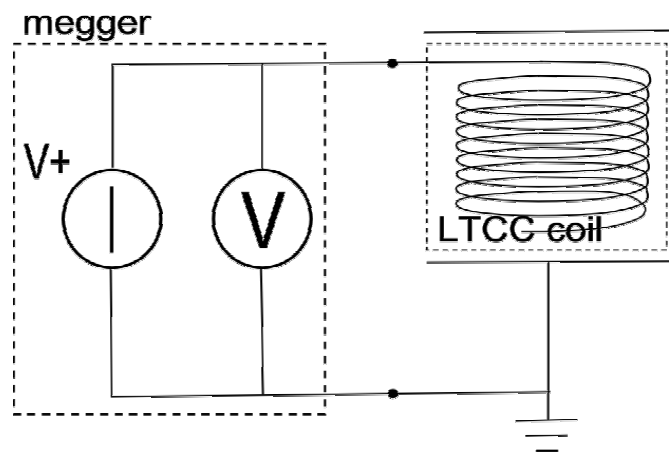


Figure 28 : insulation withstand voltage test set-up

3.1.2.2 Static and dynamic electric characterization

The sensor dynamic behavior is equivalent to that of a circuit constituted by the series of an inductance and a resistance in parallel with a capacitance (Figure 29). The above mentioned parameters have been measured using the HP4194 impedance analyzer and

are shown in **Table 10**. The measure has been carried out using twisted and short cables in order to minimize spurious signals. The equivalent electric circuit has been chosen by testing different configurations (by means of the impedance analyzer) and selecting the one that better match the measured impedance.

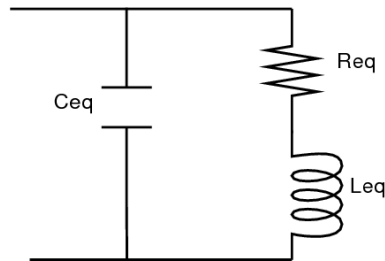


Figure 29: Equivalent circuit of the LTCC sensor

Table 10: electric parameters of the LTCC sensor equivalent circuit

Req	Leq	Ceq	Resonance frequency
[Ω]	[μH]	[pF]	[Hz]
47.4	725	32.2	1.04E+06

Figure 30 shows the bode diagram of the impedance Z_{eq} of the equivalent circuit (calculated according to the values of Req, Leq and Ceq determined).

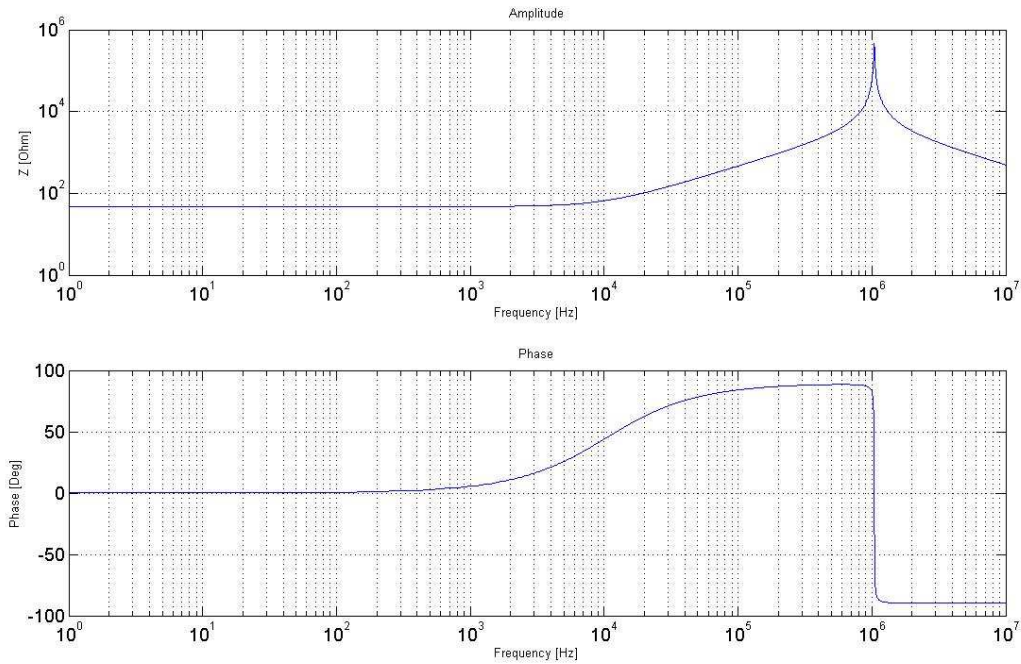


Figure 30: amplitude and phase of the equivalent impedance of the LTCC sensor

The bandwidth of the measuring probe consisting of LTCC sensor and acquisition system (schematized with the input resistance $R_{in} = 1 \text{ M}\Omega$) has been determined referring to the equivalent circuit shown in Figure 31. As transfer function (frequency response) the ratio V/E between the output signal V and the electromotive force $E = -d\phi/dt$ due to the external magnetic field has been considered.

Figure 32 shows the amplitude of the transfer function of the measuring probe (LTCC + input impedance of the acquisition system) while **Table 11** display the cut off frequency.

The transfer function V/E is the following:

$$\frac{V}{E} = \frac{R_{eq}}{(R_{eq} + R_{in} - \omega^2 L_{eq} C_{eq} R_{in}) + (j\omega L_{eq} + j\omega C_{eq} R_{eq} R_{in})}$$

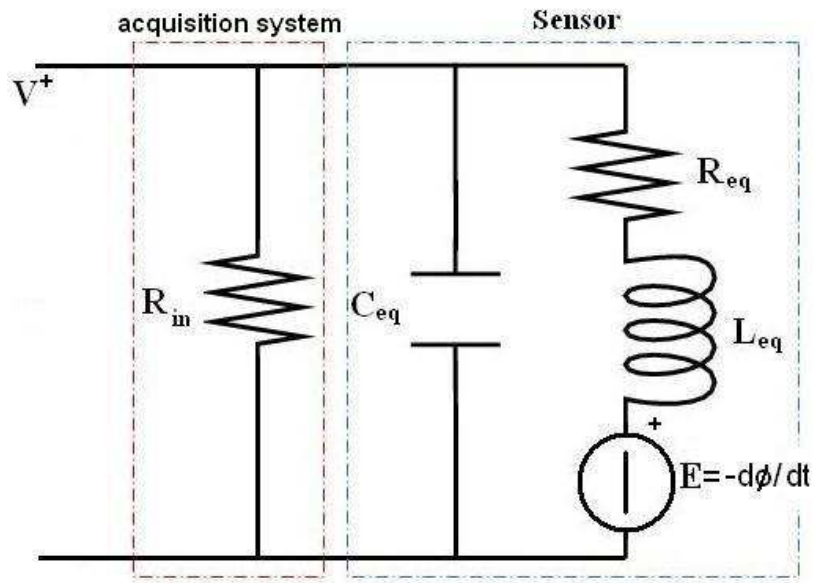


Figure 31: Equivalent circuit of the probe, consisting of LTCC sensor and input impedance of the integrator

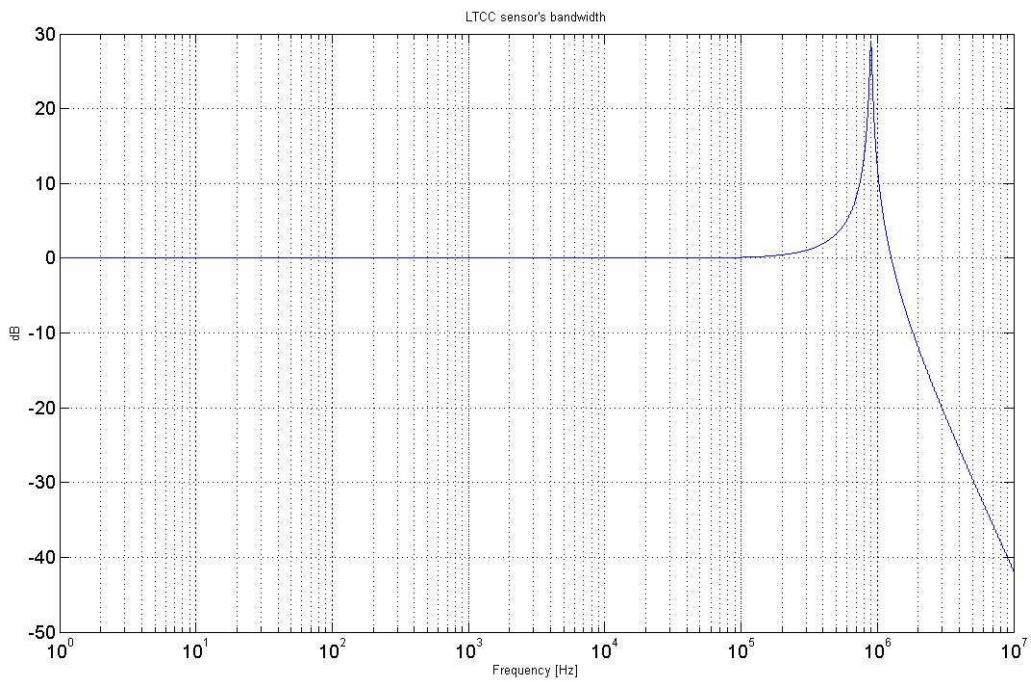


Figure 32: Amplitude of the frequency response of the LTCC magnetic probe

Table 11: cut off frequency of the measuring probe (LTCC sensor and input impedance of the acquisition system)

LTCC sensor	Cut off frequency [MHz]
Ag 10 layer sensor	1.39

3.1.3 Magnetic characterization

The equivalent magnetic areas of the LTCC sensors, main and transverse, have been measured in order to evaluate the sensitivity to magnetic fields along the main and transverse direction of the sensor (*Figure 33*).

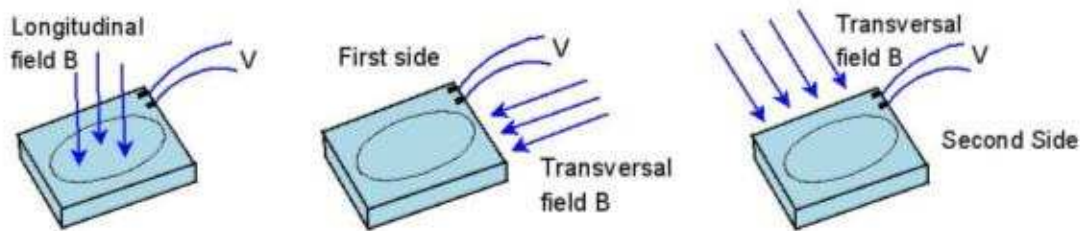


Figure 33: magnetic field crossing the LTCC sensor along three different directions: main side (left), first transverse side (center), second transverse side (right)

3.1.3.1 Instrumentation

The tests have been carried out at frequencies between 50 Hz and 10 kHz using a calibrated solenoid (*Figure 34*) to produce a well defined magnetic field. The solenoid is formed by three layers connected in series having the characteristics listed in *Table 12*.

Table 12: Solenoid characteristics

Length	545mm
Wire diameter	1.2mm
Number of coils	453 per layer
Average diameter (middle layer)	224.2mm
Equivalent inductance	140.4 mH
Equivalent resistance	20.1 Ω
Equivalent capacity	17.35pF

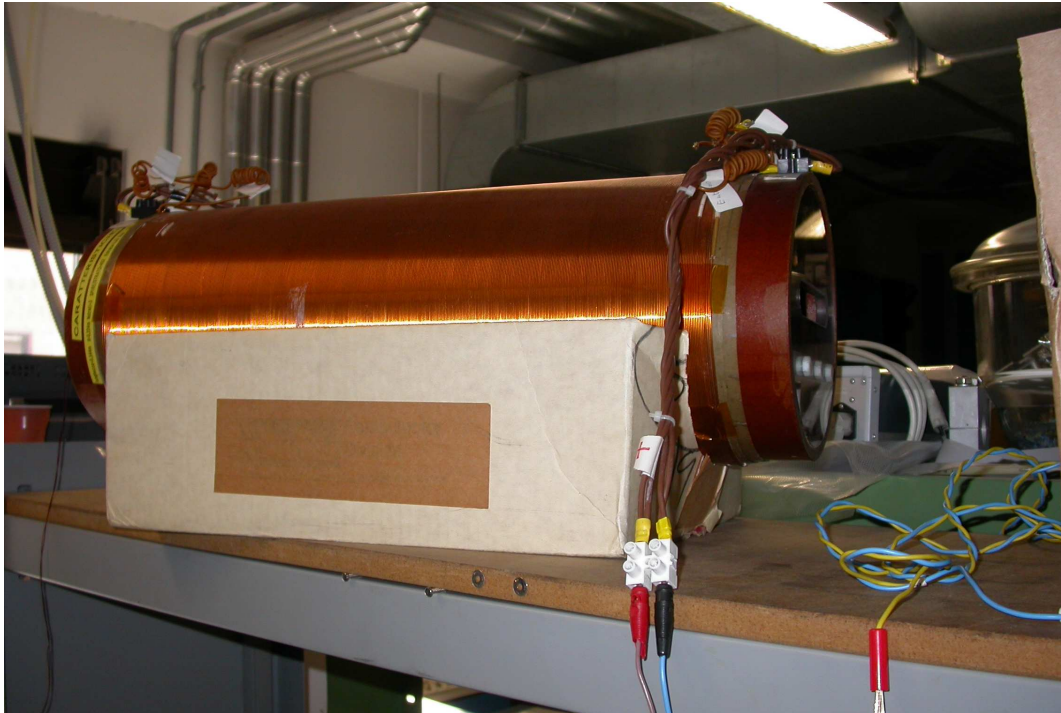


Figure 34: calibrated solenoid used to produce the magnetic field

For the test only the external layer has been used. The procedure for the magnetic calibration is based on the procedure adopted for the calibration of the magnetic sensors used for JET experiment [7].

The LTCC sensors were fixed on a calibrated support (*Figure 35*) in order to obtain a good alignment with respect to the direction of the imposed magnetic field B . The value of the field is proportional to the current I inside the solenoid, where the constant of proportionality is $k = 0.0009642 \text{ T/A}$ [8].

$$(1) \quad B = k \cdot I$$

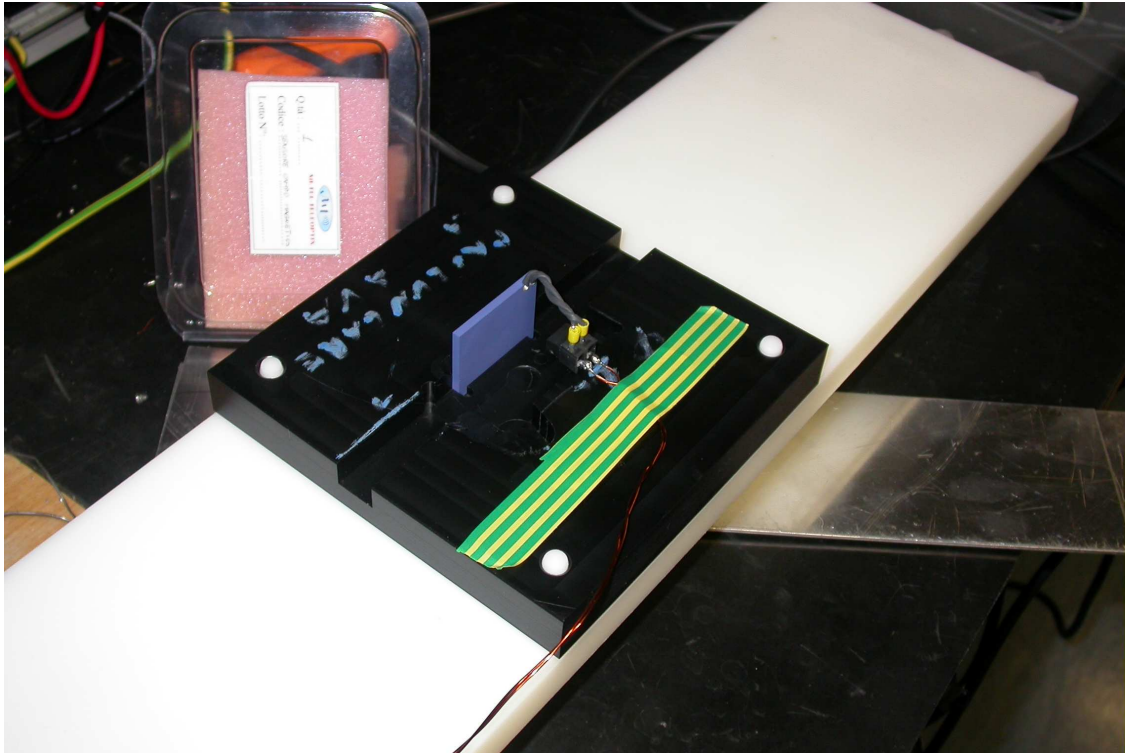


Figure 35: LTCC sensor fixed on the calibrated support

The current flowing inside the solenoid has been measured by the HP34401A multimeter (six digits and a half). Another equal instrument (HP34401A) has been used to measure the voltage between the terminals of the LTCC sensor due to faraday's law. Wavetek 18s wave generator has been used together with the Paso Serie 4000 amplifier to generate a sinusoidal current flowing on the primary circuit (solenoid). Finally to verify the variation frequency of the current the Lecroy 9310L oscilloscope has been used. **Figure 36** shows the electric circuit used for the test

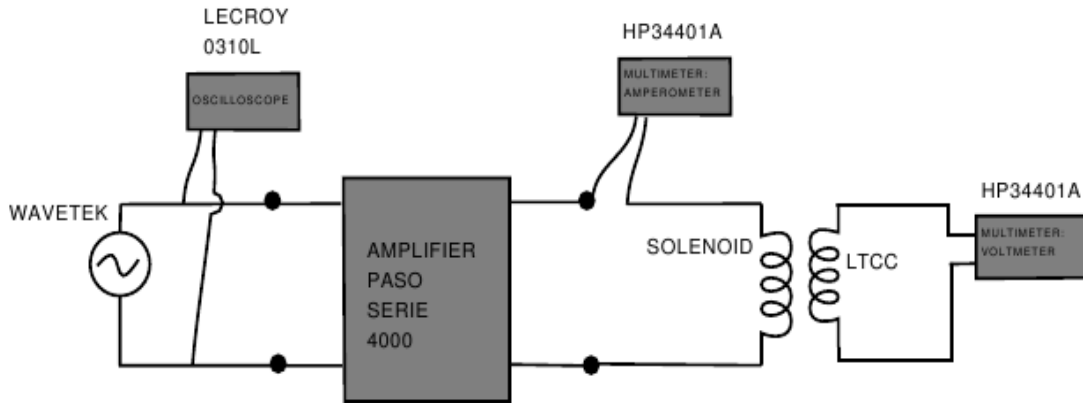


Figure 36: electric circuit

3.1.3.2 Test results

According to the Faraday-Neumann-Lenz equation written below:

$$V = -\frac{d\Phi}{dt} = -\frac{d(A_{eq}B)}{dt} = -A_{eq} \frac{dB}{dt}$$

and considering the RMS values:

$$\frac{dB}{dt} = \omega B = 2\pi f B$$

we obtain:

$$(2) \quad A_{eq} = \frac{V}{2\pi f B}$$

The longitudinal and transversal equivalent areas have been calculated. A correction has been introduced in the calculation of the equivalent area since the actual current flowing inside the solenoid is different from the current measured by the HP34401A multimeter: a fraction of the current flows through the capacitance that exist between the solenoid coils and between the connecting cables. As a consequence the magnetic field B calculated is a bit smaller than the real magnetic field produced by the solenoid. Consequently the equivalent area calculated by equation (2) is bigger than the actual equivalent area. In order to have a more reliable value of the magnetic field produced by the solenoid the following equation could be used [8]:

$$(3) \quad B = k_1 I (1 + k_2 f^2)$$

where k_1 is the same constant used in equation (1) and k_2 is $1.37e^{-10}$.

During the test the sensor has been wrapped into an aluminum foil in order to shield high frequency fields. This causes a reduction in the amplitude of low frequency waves too. This reduction has been estimated as following. With an aluminum foil of 0.025mm the reduction at 5KHz is about 1.2%. In fact the depth of penetration for aluminum at 50Hz is $\delta_{50Hz} \approx 13\text{mm}$. At 5kHz $\delta_{5kHz} \approx 1.3\text{mm}$, and so:

$$\frac{\Delta B_{5kHz}}{B} = e^{-1} \frac{\text{thickness}}{\delta_{5kHz}} = 0.63 \frac{0.025}{1.3} \approx 1.2\%$$

with a frequency of 5kHz. In the case of 50Hz the reduction is:

$$\frac{\Delta B_{50Hz}}{B} = e^{-1} \frac{\text{thickness}}{\delta_{50Hz}} = 0.63 \frac{0.025}{13} \approx 0.12\%$$

This reductions, function of frequency, haven't been considered in the equivalent transversal area calculation.

The test has been carried out upon two different Ag LTCC sensors named Ag-10-1 and Ag-10-2. The results are shown in **Figure 37** (main area) and **Figure 38** (transverse area, both sides).

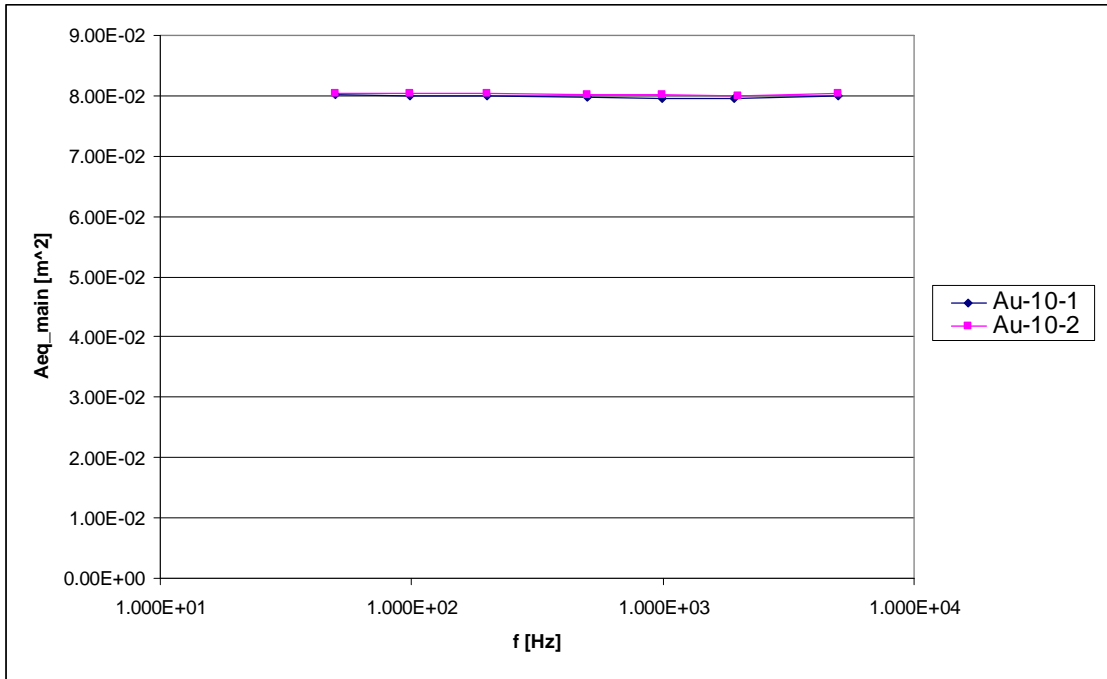


Figure 37: main equivalent area of Ag 10-layer LTCC sensors

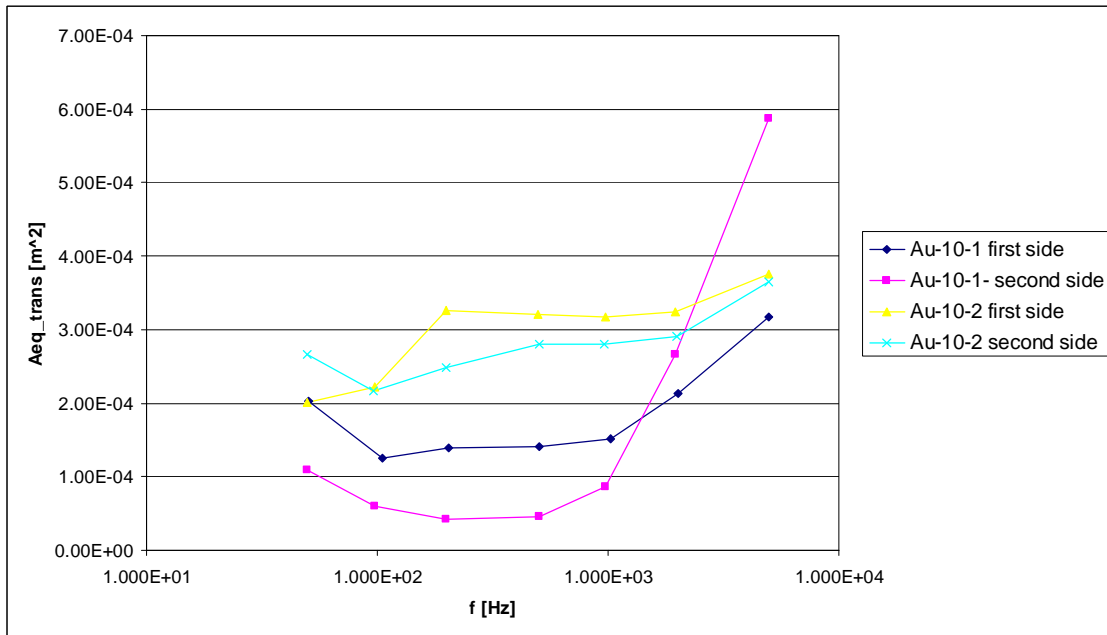


Figure 38: transverse equivalent area of Ag 10-layer LTCC sensors, both sides

Table 13 lists the values of the main and transverse equivalent area at 100Hz for each sensor and the maximum $A_{transverse}/A_{main}$ ratio. The magnetic equivalent area of the

sensors are fully satisfactory, since along the main direction it is consistent with the geometrical characteristics of the winding and along the transverse direction is <1%.

Table 13: average values of main and transverse area and maximum $A_{\text{transverse}}/A_{\text{main}}$ ratio

Sensor	Main Area [m ²]	Transverse first side area [m ²]	Transverse second side area [m ²]	Maximum $A_{\text{transverse}}/A_{\text{main}}$
Ag_10_1	7.99E-02	1.24E-04	6.02E-05	0.2%
Ag_10_2	8.05E-02	2.23E-04	2.17E-04	0.3%

3.1.4 Thermal characterization

The equivalent thermal conductivity of the LTCC sensor λ has an important effect on the thermal gradient during operation, when the sensor is subjected to neutron radiation and the thermal power produced shall be drained towards the internal wall of vacuum vessel. In order to measure the (equivalent) thermal conductivity of the LTCC sensor, the set-up shown in **Figure 39** has been used, where the internal printed circuit of the sensor has been used as heat generator. If the two sensors are connected to a DC voltage source, in steady state conditions the electric power VI is equal to the longitudinal heat flux transferred to the sink across the two sensors. The thermal resistance of the LTCC sensor can be determined by measuring the temperature drop across the thickness from the mid-plane to the edge.

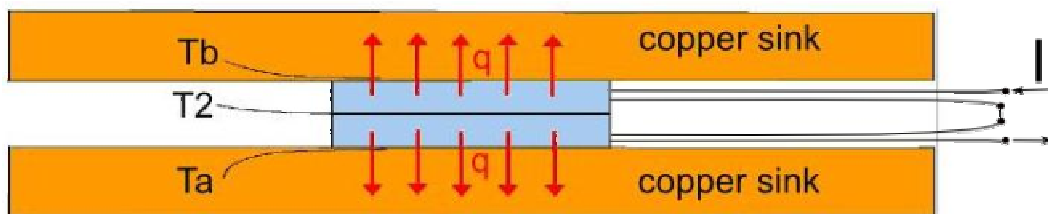


Figure 39: experimental set-up

3.1.4.1 Mathematical model

We first define a simple mathematical model of thermal conduction which establishes a relationship between the conductivity of the LTCC sensor and the temperature distribution. The equation of thermal conduction for an indefinitely wide slab with internal heat generation is the following:

$$\frac{d^2T}{dx^2} + \frac{H}{\lambda} = 0$$

where H is the internal heat generation power per unit volume (constant for simplicity) and λ is the conductivity of the material. By integrating the differential equation with the boundary conditions indicated below we obtain (**Figure 40**):

$$T(L) = T_1 \quad T(-L) = T_1$$

$$(4) \quad T = T_1 + \frac{H}{2\lambda}(L^2 - x^2)$$

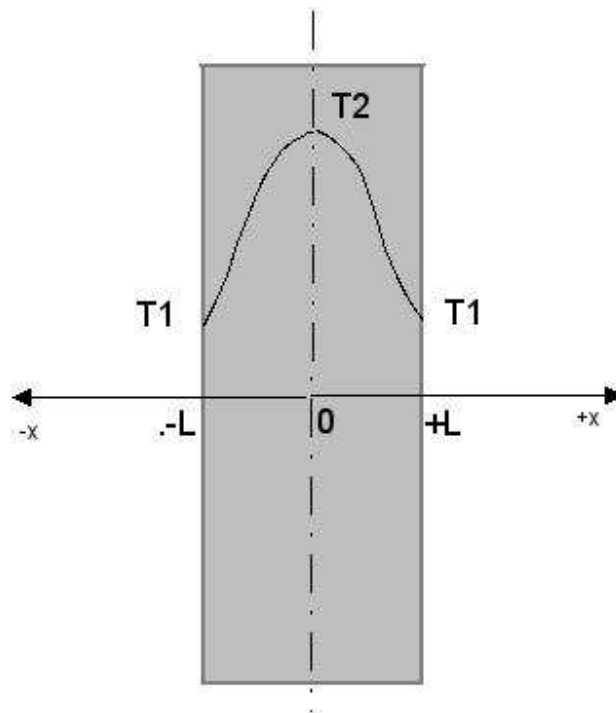


Figure 40: Thermal distribution according to the model

Figure 40 shows the variation of the temperature along x . From the knowledge of the maximum temperature T_2 at $x=0$ can be reversed equation (4) in order to obtain the conductivity

$$(5) \lambda = \frac{H}{2(T_2 - T_1)} (L^2 - 0^2) = \frac{H}{2(T_2 - T_1)} L^2$$

If we assume a thermal flux normal to the plain section of the LTCC sensors then the experiment can be described using a one-dimensional model, considering the two LTCC sensors like an infinite slab. This assumption is realistic thanks to the small thickness of the sensors, which ensures that only a little fraction of the heat gets out from lateral sides by thermal convection with air.

We also assume that the heat produced by the internal circuit of the LTCC sensor is homogeneously distributed on the entire volume. This is realistic since the electric circuit is formed by many layers distributed in the entire thickness of the sensor.

3.1.4.2 Test results

The above geometrical conditions have been achieved by using two Ag LTCC sensors and two copper bars (thermal sinks), as shown in **Figure 39**. The temperature drop between the middle surface (the surface between the two LTCC sensors) and the copper bars have been measured by three thermocouples (**Figure 39**). A thin aluminum plate with a slit to fit the insulated thermocouple has been placed between the two sensors in order to measure the central temperature T_2 . The temperature T_1 can be calculated by taking the arithmetic mean between T_a and T_b . It is worth noticing that any air gap between the two LTCC sensors does not compromise the results since there is no thermal flow across the central surface (the system is symmetric). The LTCC sensors were connected in series and fed with an electric current to produce like heat generators a thermal flux along the main direction of the sensors, from the center to the thermal sinks. In order to assure a good thermal contact between the surfaces the KF 1201 thermal conductive paste (CRC Industries France S.A.) has been set on every surface before clamping.

Figure 41 and *Figure 42* show the instrumentation used during the test while *Figure 43* shows the experimental set-up. The data acquisition Agilent 34970A was used to acquire the thermocouple signals, the voltage signal from LEM current probe PR30 (Figure 20) and the voltage between terminals of the sensors (connected in series). Two multimeters HP34401A were used to check the values of current and voltage acquired by Agilent 34970A. A KEPCO BOP 50-8M DC power supply was used to produce the voltage needed (about 20V).

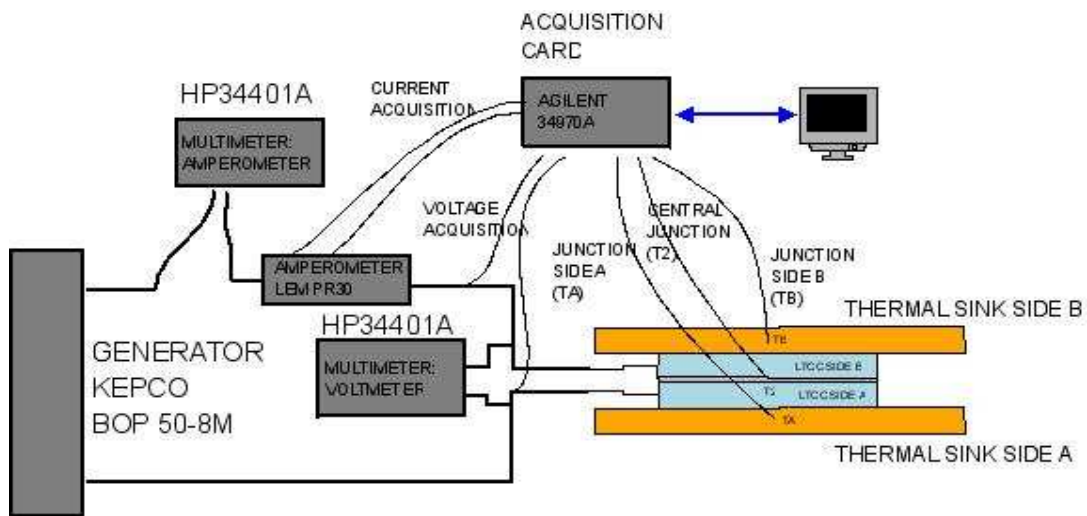


Figure 41: instrumentation used during the test

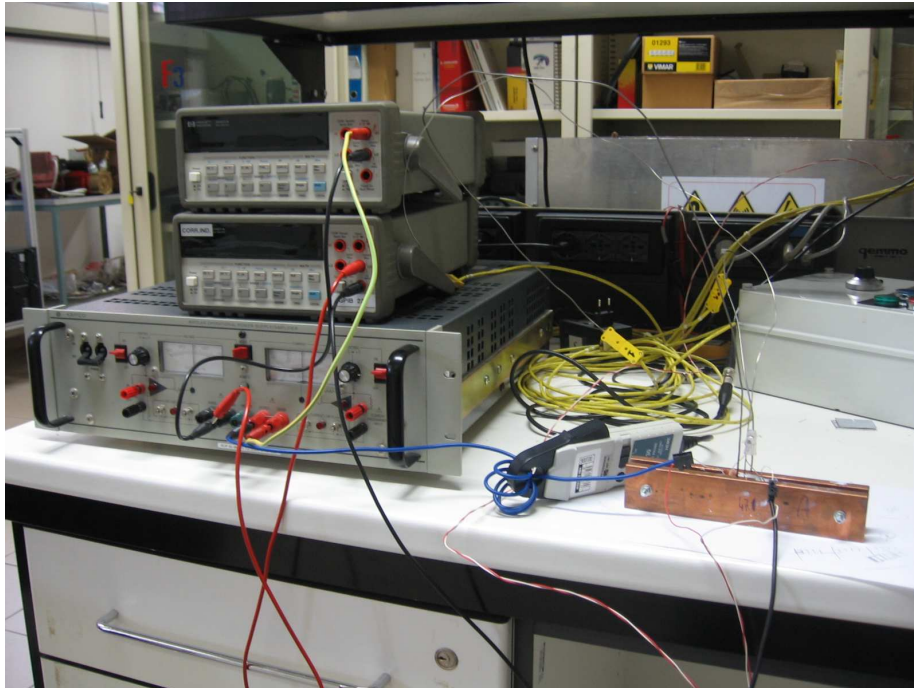


Figure 42: instrumentation used during the test

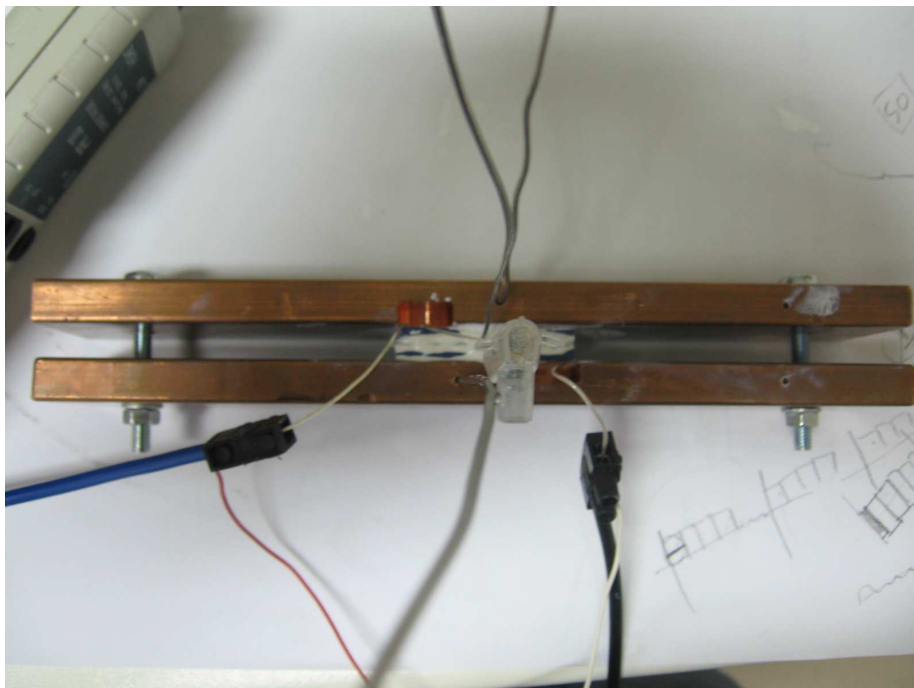


Figure 43: experimental set-up

The acquisition of temperatures, voltage and current has been carried out at a frequency of 0.25Hz. The average current flowing inside the LTCC sensors was 0.197A and the

Voltage drop was 18.9V (considering the two sensors in series). **Figure 44** shows the temperature variation with time. During the first 2 hours the power was on and the typical exponential rise is visible. The power was then turned off and the temperature was recorded for a period of 4 hours, till the sensor temperature reached the room temperature.

The blue line in the figure represents the temperature of the central point, measured by the thermocouple installed between the two LTCC sensors: T2 (**Figure 39**). The red line represents the temperature of the sink side a, T_a , while the yellow line represents the temperature of the sink side b, T_b . The two temperatures T_a and T_b are not exactly equal, being the temperature of the side a slightly lower than the temperature of side b (the difference is 0.4°C). This is most likely due to the different resistances of the two LTCC sensors. This light asymmetry has been neglected in this study and an average temperature of the sink T_1 has been considered:

$$(6) T_1 = \frac{T_a + T_b}{2}$$

The total heat power produced can be found by Ohm's law:

$$q = R_A I^2 + R_B I^2 = 1.88 + 1.9 = 3.79W$$

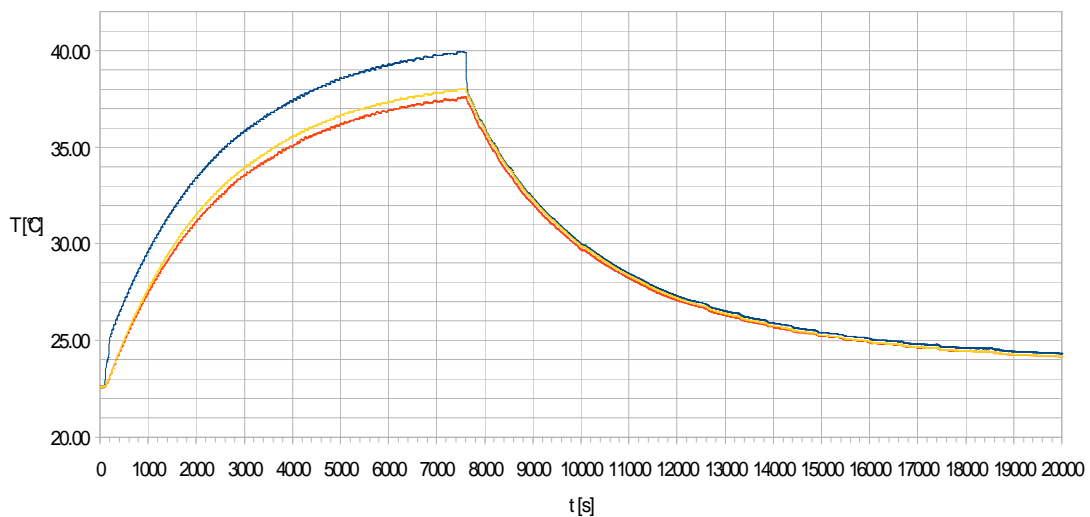


Figure 44: temperature variation with time

The thermal conductivity λ has been calculated according to equation (5):

$$\lambda = \frac{H}{2(T_2 - T_1)} L^2$$

The internal heat generation power H is:

$$H = \frac{q}{2\text{Vol}}$$

Where Vol is the volume of one LTCC sensor equal to 3600mm².

To calculate the thermal conductivity λ by eq (5) we have followed the following way: for 6000s < t < 7500s λ (t) was calculated according to eq. (5) using the instantaneous values of T_2 , T_a and T_b . Then the average value of λ (t) was calculated.

The final result is $\lambda = 1.1 \frac{W}{mK}$. We choose the range from t=6000s to t=7500s because the differences $T_2 - T_A$ and $T_2 - T_B$ remain almost constant inside this interval (the system is in the proximity of the steady state condition).

This value of λ is smaller than the thermal conductivity of the fired ceramic declared by Heraeus in the LTCC CT700 data sheet which is $\lambda_{datasheet} = 4.3 \frac{W}{mK}$.

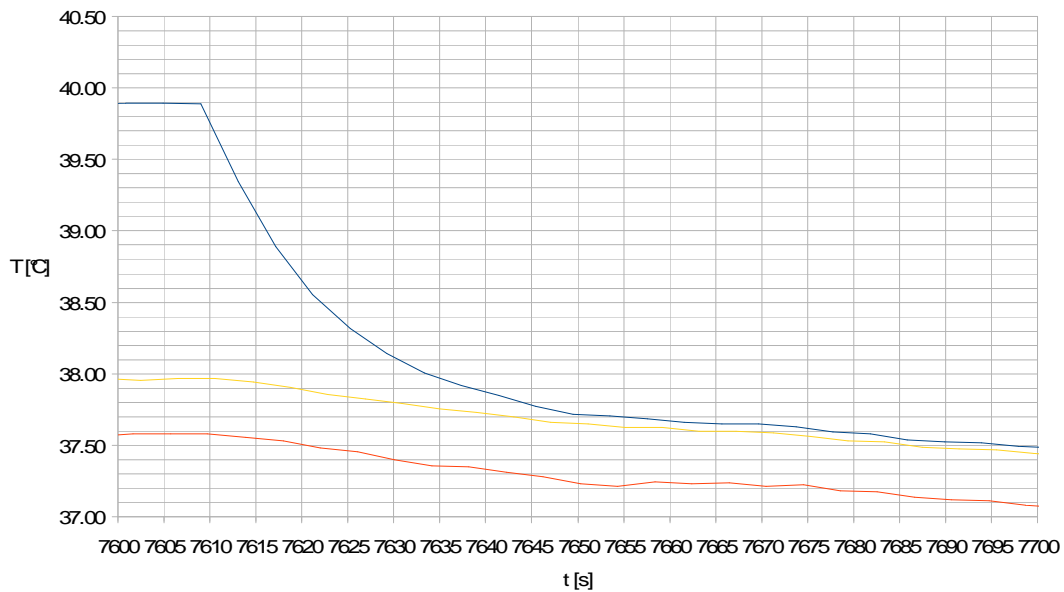


Figure 45: Sharp descent of temperature T_2 after power has been turned off

Fig. 4 shows a detail of the graph in fig. 3: it's possible to appreciate the sharp descent of temperature T_2 after power has been turned off. The constant of time of the LTCC sensor is small, about 15 seconds, how it's possible to see from the graph.

3.1.4.3 Spice simulations

To verify the value of the thermal conductivity λ a Spice simulation has been carried out taking advantage of the electric analogy. SPICE (Simulation Program with Integrated Circuit Emphasis) is a general-purpose open source analog electronic circuit simulator used in integrated circuit and board-level design to check the integrity of circuit designs and to predict circuit behavior.

According to the electric analogy the thermal flux q could be treated like a current I while the temperature variation between two different layers ΔT could be treated like a voltage V . Moreover, heat generators (the printed circuit of each layer) could be treated like current generators and the thermal resistances (the layers of ceramic between the circuits) like electrical resistances (see *Figure 46* and *Figure 47*). Ohm's law could be rewritten in this way:

$$\Delta T = R_i q^*$$

where $R_t = \frac{l}{\lambda}$ is the thermal resistance of the ceramic layer and q^* is the heat flux per unit area q/A . The quantity l is the thickness of one layer of the sensor: $200 \mu m$. The unknown quantity is the thermal resistance R_t .

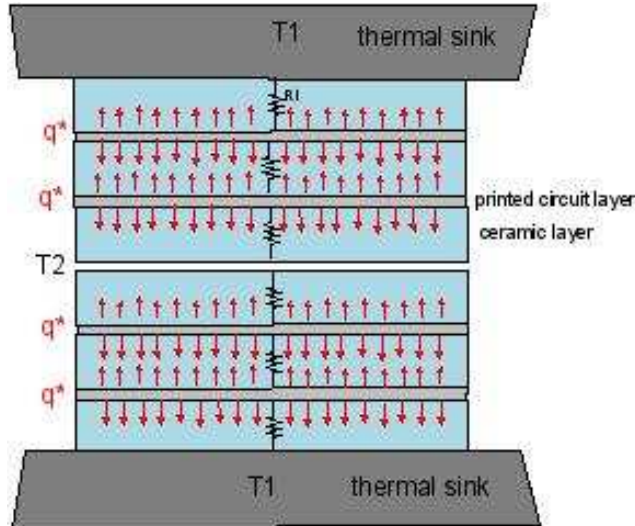


Figure 46: internal heat generators and resistances

Figure 47 shows one half equivalent circuit.

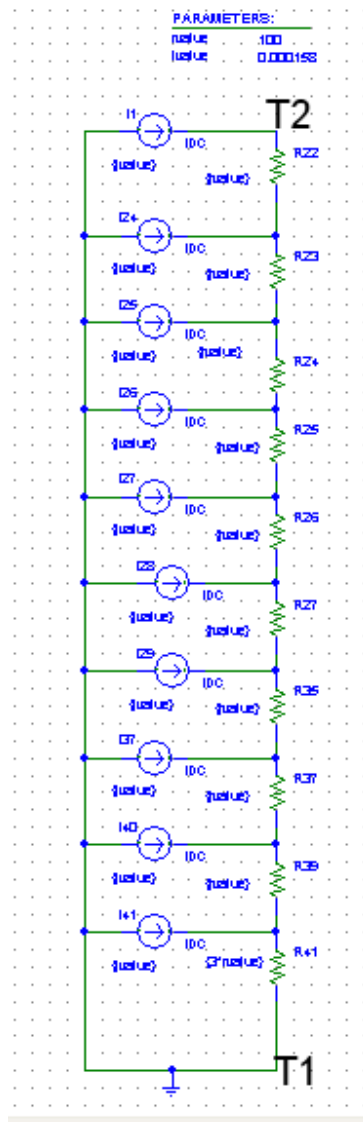


Figure 47: one half equivalent circuit.

Each heat generator produces a heat flux $q^* = 0.000158 \frac{W}{mm^2}$ (calculated according to (7)).

$$(7) \quad q^* = \frac{P}{10A}$$

Simulation results show that a resistance $R_l = 182 \frac{mm^2 K}{W}$ produces a temperature drop $T_2 - T_1 = 2.15K$.

Since $R_l = \frac{l}{\lambda}$ we obtain:

$$\lambda = \frac{l}{R_t} = \frac{0.2}{182} = 0.0011 \frac{W}{mmK} = 1.1 \frac{W}{mK}$$

3.1.4.4 Final considerations

The measured thermal conductivity λ is less than a quarter of the value declared by Heraeus in the LTCC CT700 data sheet. Some considerations must be done about the reliability of the experiment:

- According to the manual of the instrument the total measurement error (thermocouple plus Agilent 34970A acquisition system) is $<2^\circ\text{C}$. This error includes the error of the thermocouples and the error on voltage measurement and digitalization. However, since we are only measuring a temperature difference (temperature drop across the thickness of LTCC sensor) and we calibrate the measurement system in conditions of uniform temperature at the beginning of the experiment, the systematic error due to thermocouples is cancelled for the calculation of λ . Only the error due to voltage acquisition must be evaluated. The resolution of the Agilent34970A is $3\mu\text{V}$, the thermocouple constant is $42 \frac{\mu\text{V}}{^\circ\text{C}}$ and consequently the maximum error on voltage acquisition is $\frac{3}{42} = 0.07^\circ\text{C}$. By adding an error due to non linearity of the thermocouples and digitalization we obtain an error that is less than 0.2°C . This uncertainty on temperature measurements causes an uncertainty on the estimation of λ which is approximately $0.2/(T_1-T_2) \lambda \approx 10\%$
- The use of a simple one-dimensional model to describe the phenomenon is realistic thanks to the small thickness of the sensor, which ensures that only a little fraction of the heat gets out from lateral sides by thermal convection in air.
- Thermocouples used to measure the temperatures of copper sinks have been fitted near the centre of each sink but a little difference of temperature ΔT_c is present between the midpoint of each sink and the surface of the sink that matches the surface of the sensor. This difference ΔT_c has been assumed to be negligible because of the large thermal conductivity of the copper (with respect to thermal

conductivity of LTCC material): the sink has been considered at a uniform temperature.

3.1.5 Outgassing rate in ITER relevant conditions

The measurement has been taken in a small vacuum oven equipped to carry out the dynamic flow method [4] in which sensors are introduced in order to evaluate their Outgassing Rate (OR). The vacuum level was of the order of 10^{-9} mbar.

The set-up of the experiment is shown in *Figure 48* and *Figure 49*. The position of the five thermocouples used during the tests is also shown in *Figure 48*.

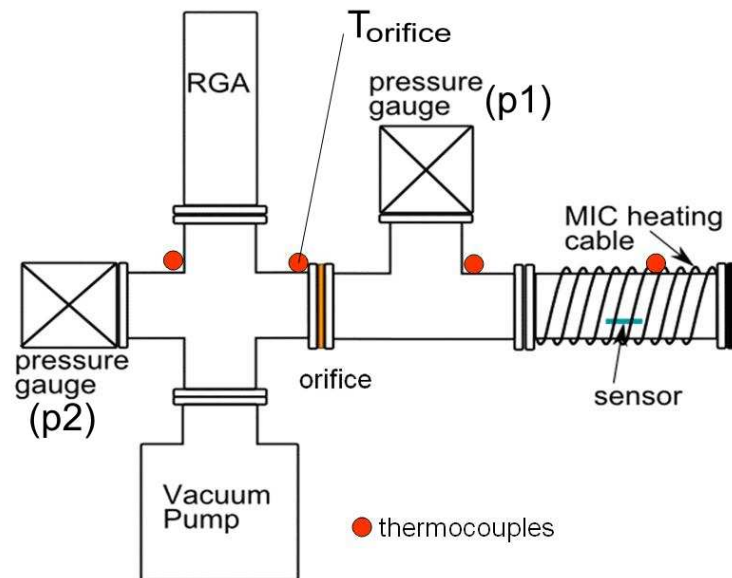


Figure 48: experiment set-up

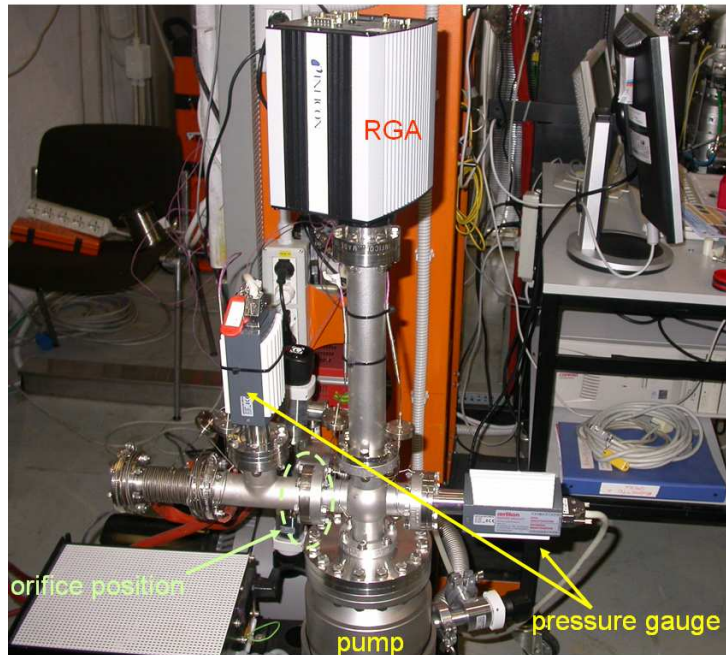


Figure 49: experiment set-up

The following instruments have been used to control the experiment:

- Pressure gauges p1 and p2: Ionivac ITR 90 full range
- Vacuum pumps: molecular pump in series with a dry scroll pump
- Residual Gas Analyzer (RGA) : Transpector H100M RGA

Near the pump inlet an orifice of 2mm has been mounted, **Figure 50** shows a sample of the orifices used during this experiment.

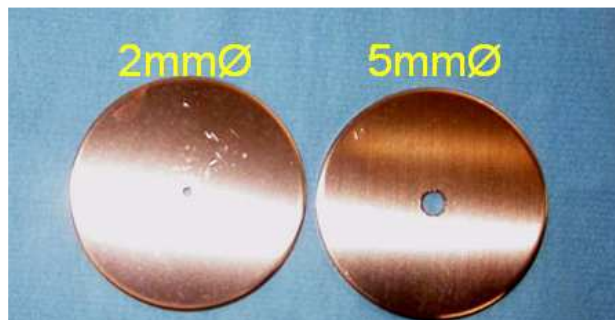


Figure 50: a sample of the orifices used

The experiments has been carried out with the following order

- Empty chamber only
- Ag LTCC sensor

All the parts of the oven involved, except for the sensors and the pump, have been cleaned with ultrasounds and baked at 150°C for 3 days. The baking cycle is reported in Figure 51, while in Figure 52 the effective baking cycle is indicated.

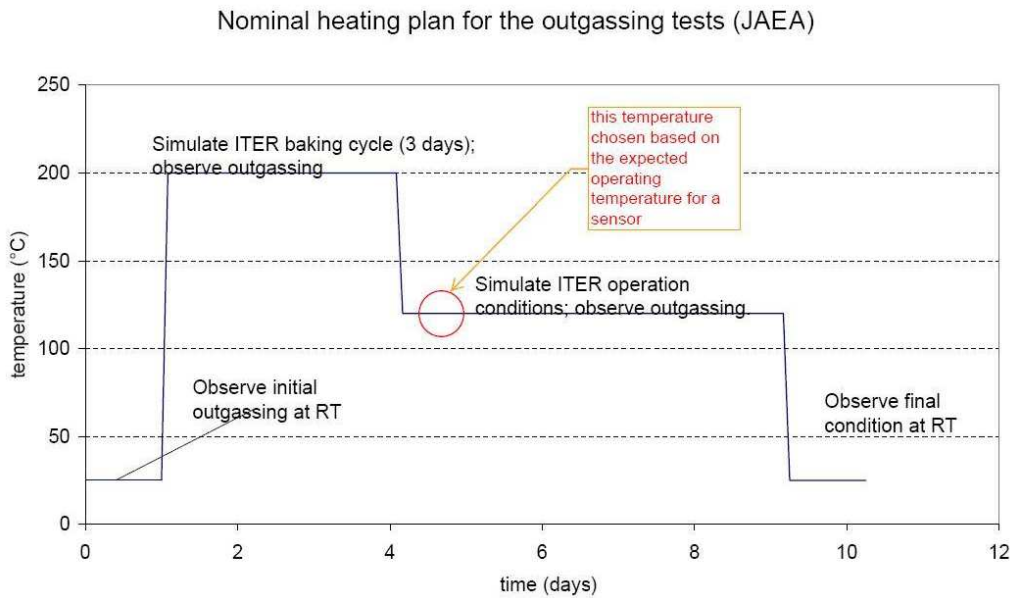


Figure 51: ITER like baking cycle for outgassing measurements [4]

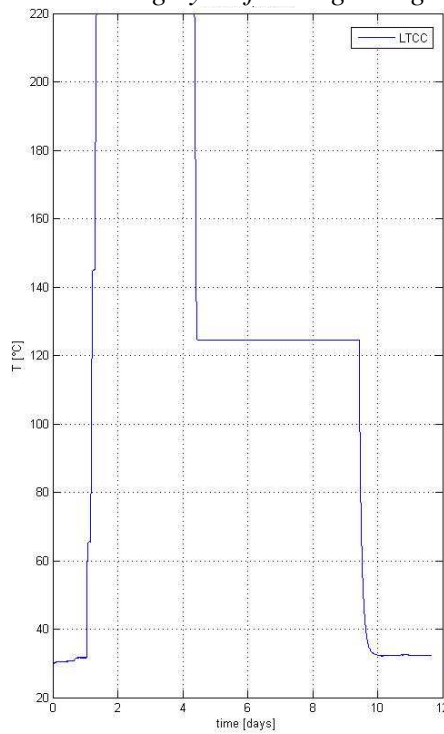


Figure 52: Effective Baking Cycle, according to [5]

The out-gassing rate Q has been calculated according to (8):

$$(8) Q = C \cdot (p_1 - p_2)$$

where p_1 and p_2 are the pressures measured and C is the conductance of the orifice. The conductance of other parts of the conduit has been neglected because much smaller than the orifice's.

The conductance of the orifice has been calculated according to (9) [6]:

$$(9) C = \frac{A}{4} \cdot \frac{1}{1 - (d_{\text{orifice}}/d_{\text{conduit}})^2} \cdot \sqrt{\frac{8RT}{\pi M}}$$

where R is the gas constant, A is the orifice's opening, T is the average temperature between the two pressure gauges (T_{orifice} used, see **Figure 48**) and M is the molecular mass of the gas inside the vacuum chamber.

Table 14 reports the results of the experiment at the end of the baking cycle; the OR values of the sensors are obtained by difference with OR value of the empty chamber.

Table 14: Absolute OR of sensors and empty chamber

	Empty chamber * 10^{-9} [Pa m ³ /s]	Ag LTCC sensor * 10^{-9} [Pa m ³ /s]
120°C	7.3	11-7.3 = 3.7
30°C	0.7	2.7 - 0.7 = 2.0

Figure 53 indicates the measured pressures and the calculated OR for the empty chamber while **Figure 54** shows the pressures and the OR of the Ag LTCC sensor.

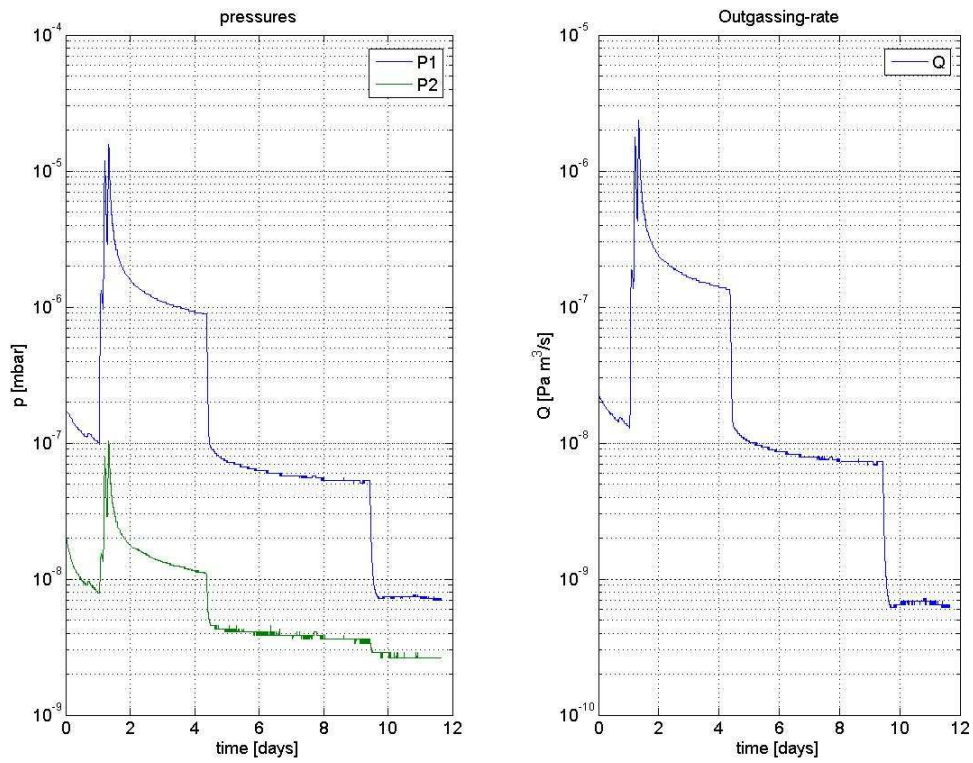


Figure 53: Measured Pressures (left) and out-gassing rate of the empty chamber (right)

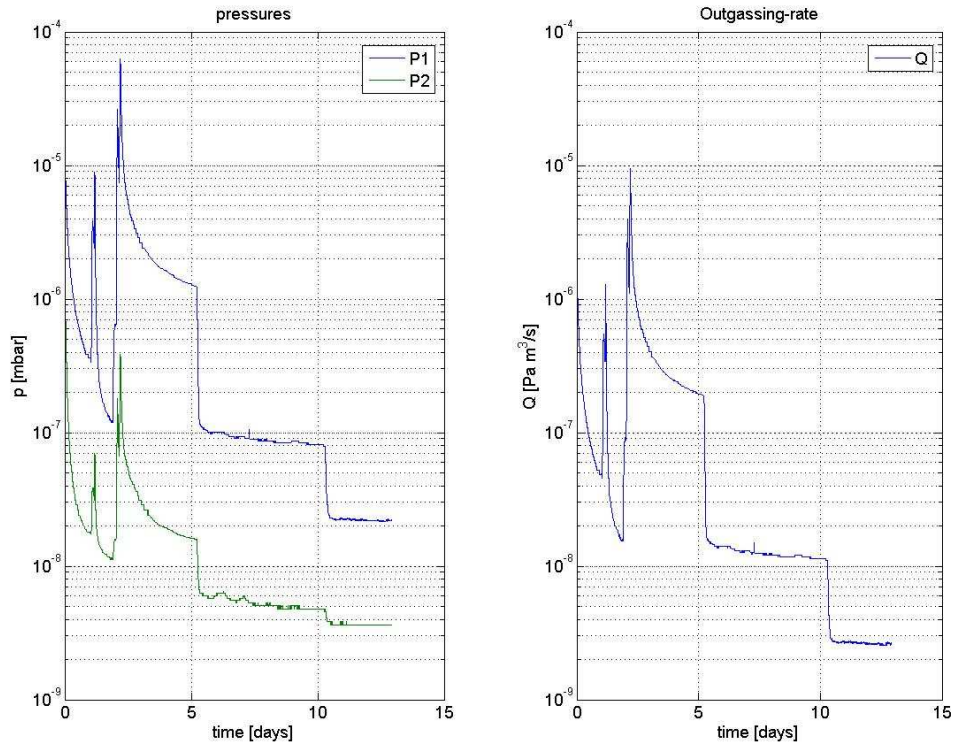


Figure 54: Measured pressures (left) and out-gassing rate of the Ag LTCC sensor (right)

The obtained out-gassing rate per unit area is reported in Table 15. The out-gassing rate of one Ag LTCC sensor is in the order of magnitude of 10^{-9} Pa·m³/s. Considering the geometrical dimensions of the sensor, the specific out-gassing rate at 120°C is approximately $2,4 \cdot 10^{-6}$ Pa m³ s⁻¹ m⁻², which is one order of magnitude larger than the limit requested in ITER Vacuum Handbook [5]. Due to the unavailability of a proper calibrated RGA, pure H₂ has been considered as out-gassed substance and this choice determines an overestimation of the out-gassing rate.

Table 15: out-gassing rate results

Ag LTCC sensor	
* 10 ⁻⁶ [Pa m ³ /s m ²]	
120°C	2.4
30°C	0.83

The composition of the gas inside the vacuum chamber has been estimated observing the mass spectrum by means of the Transpector H100M Residual Gas A. Figure 55 to **Figure 56** show the pattern of the ion current peaks as a function of mass-to-charge ratio for the different tests carried out.

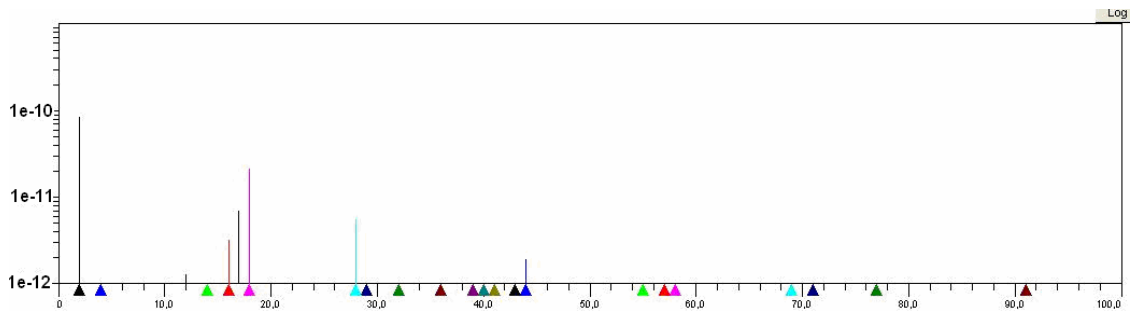


Figure 55 : Mass spectrum of the empty chamber

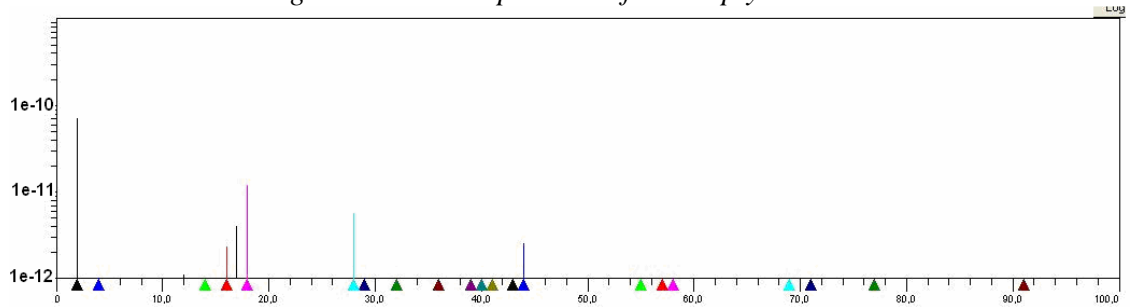


Figure 56 : Mass spectrum of the chamber + Ag LTCC sensor

As indicated in figures above, the main substances in the vacuum chamber are H₂ (mass 2), CH₄ (mass 16), NH₃ (mass 17), H₂O (mass 18), N₂ and CO (mass 28) and CO₂ (mass 44). It can be noted that the major peak is located at mass 2.

Looking at *Figure 56* it can be argued that the main substance would be H₂, being the corresponding current peak exceeding of 1 order of magnitude larger than the other peaks. Nevertheless there is a great uncertainty in this measurements set-up on the RGA sensitivity to the different substances, which affect strongly the evaluation of the partial pressures from the current peaks measurements. It is also worth noticing that the peak CH₄ is reduced inserting the sample, indicating probably an absorption phenomena. More accurate results require a specific data analysis.

Our experience indicates that is very hard to evaluate the OR of gas single species; because of technical limits of the instruments available .

3.1.6 TIEMF measurements

The TIEMF effect is the presence of a parasitic voltage induced by thermal gradients inside the sensor. This undesired voltage can strongly affect the measurements of the magnetic fields inside the ITER vacuum vessel because of the drift produced during long integration time.

The data acquisition Agilent 34970A has been used to acquire the signals from the thermocouples and the induced voltage (TIEMF). In the case of DC voltage measurement the range error of the instrument is 0.004%, that is 4μV (range used equal to 100mV). The reading error is negligible because being equal to 0.005% of the read value, that is less than 1nV. The total error is therefore ~ 4μV. For the temperature measurements the error is <2°C.

Figure 57 and *Figure 58* show the experimental set-up. The LTCC sensor was clamped between two copper bars that play the role of thermal sinks. The upper bar was first warmed up (first stage) by a flow of hot air in order to obtain a positive difference of

temperature T_1 – T_3 and then cooled (second stage) by compressed air in order to reverse the thermal flux. During all the process the induced voltage V (TIEMF) between the two terminal wires of the sensor was measured together with the temperatures of the sinks T_1 , T_2 , T_3 , T_4 .

The four thermocouples were placed inside calibrated holes in the copper sinks, two thermocouples per sink.

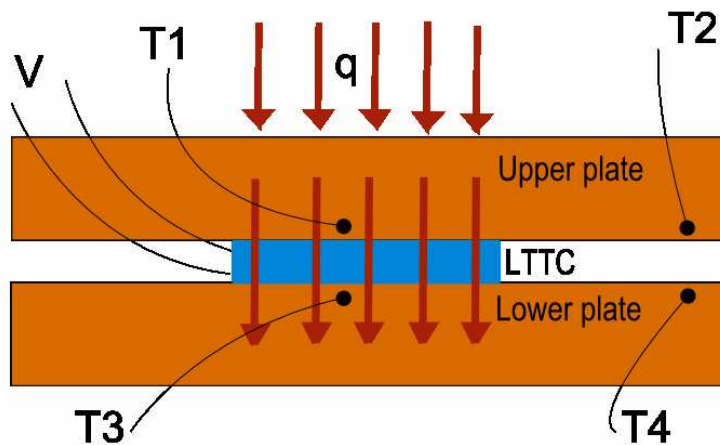


Figure 57: TIEMF experimental set-up

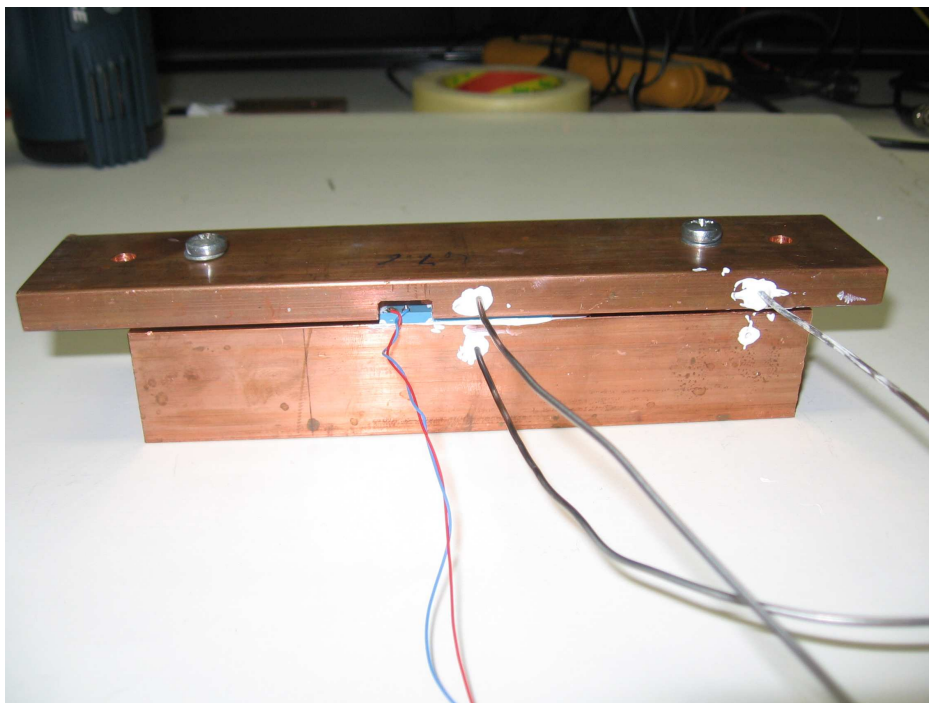


Figure 58 : LTCC sensor between copper bars

Figure 59 shows the variation of T_1 , T_2 , T_3 and T_4 during the heating and cooling process for the Ag sensor. Figure 60 shows T_1-T_3 and T_2-T_4 versus time (left) and TIEMF versus T_1-T_3 (right) for the Ag sensor. In the same figure (right) the Ordinary Least Square (OLS) line has been drawn in order to highlight the linear dependence between the difference T_1-T_3 and the TIEMF effect.

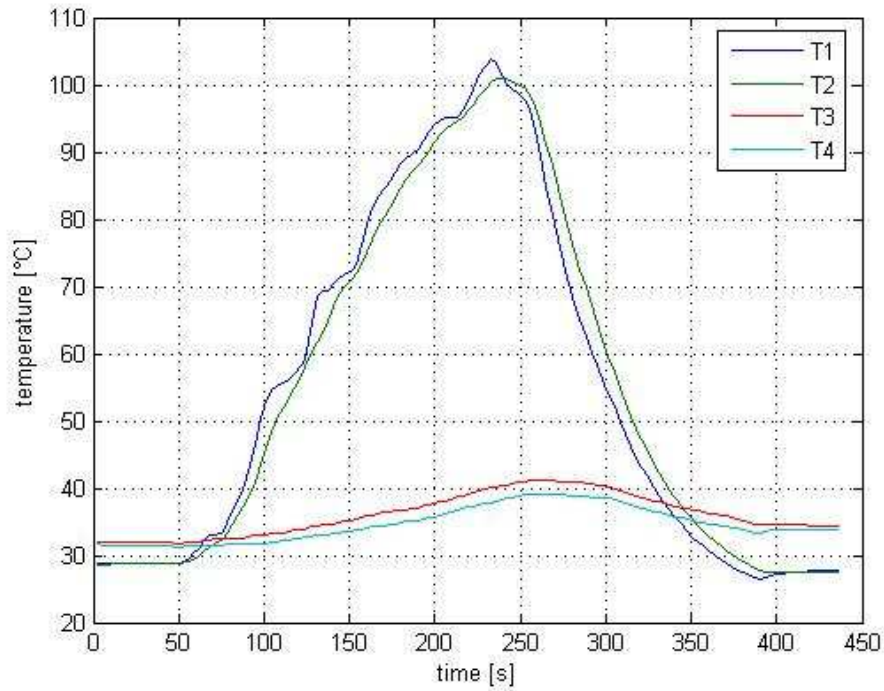


Figure 59 : temperatures T_1 , T_2 , T_3 , T_4

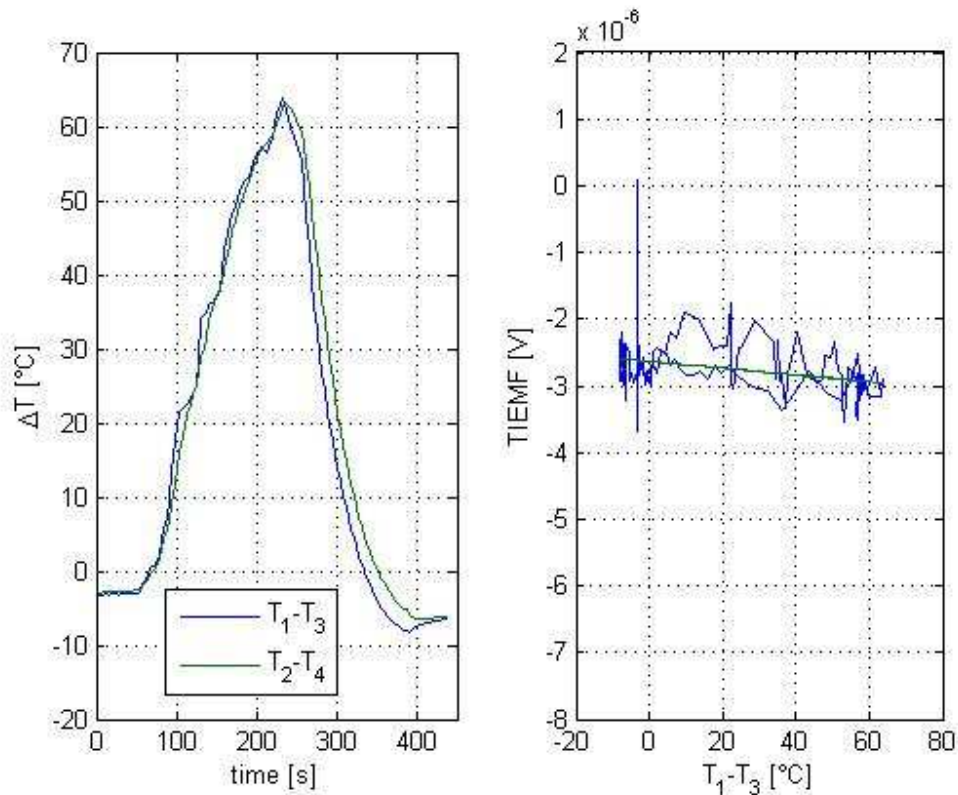


Figure 60 : temperature drop between the two copper sinks (left) and TIEMF (right)

3.1.6.1 Discussion

Since the measured values of TIEMF are of the same order of magnitude of the error of the instrument ($4\mu\text{V}$), it's clear that the graphs showed above can only describe the phenomena in a qualitative way. In order to obtain reliable TIEMF values an acquisition instrument with a better precision (some nV) is necessary.

Since the terminal wires were protected inside a rectangular slot in the upper bar (**Figure 61** and **Figure 58**) they were not exposed to thermal flux and the temperature gradient on the Au-Cu junction was negligible.

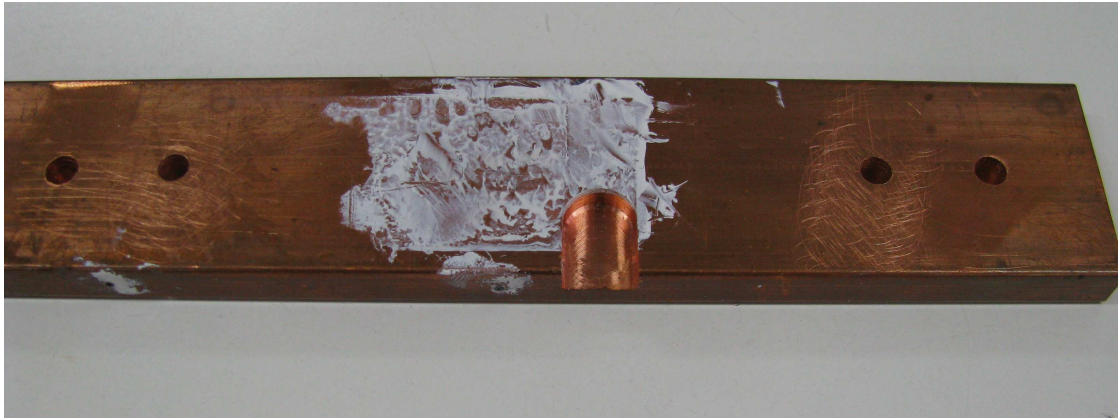


Figure 61 : slot in the upper bar

3.2 Design and testing of Au LTCC sensors

Two new sets of LTCC sensors have been built by Linkra (<http://www.linkra.it>) and tested by Consorzio RFX in the framework of the ITER Contract ITER/CT/08/529.

- a first set of 3 sensors formed by 10 conductive layers
- a second set of 7 sensors formed by 30 or 40 conductive layers (being the achievement of the maximum number of layers a limit to be attempted and explored with the present manufacturing process).

These prototype sensors have been designed on the basis of Ag sensors already supplied to Consorzio RFX by Linkra (formerly Mitel-Teleoptix) in January 2008. The new sets of prototypes were aimed at obtaining a sensor with an increased magnetic area, compatible with the final ITER requirements, and at testing different composition for the ceramic layers and conductor material:

- Au conductor material in place of Ag (inner conductive lines, vias and connecting pads)
- DuPont 951 ceramic in place of Heraeus CT700
- Number of conductive layers increased from 10 to 30 (or tentatively 40)

Au has been chosen also because this material should transmute less than Ag under neutron radiation. Anyway, since Au transmutes to Hg under neutron radiation while Ag transmute to Cd, the comparison between Au and Ag transmutation effect can be achieved by observing the amount of Cd/Hg from an out-gassing test after a neutron radiation of the sensors.

Anyway, Ag and Au are both LTCC compatible and regarding transmutation there isn't much difference between Au and Ag.

The DuPont 951 ceramic has been chosen in place of Heraeus CT700 since the last one contains some percentage of Co, Ba and Sr, being these substances not suitable for the ITER vacuum vessel.

The design parameters and reference requirements for the Au prototype sensors are summarized in *Table 16*.

Sensor dimensions (max)	30mm x 40mm x 15mm
Equivalent magnetic area (optimal value)	0.3m ²
Electrical resistance (optimal value)	100 Ω
Electrical resistance (maximum value)	500 Ω
Ceramic substrate material	Al ₂ O ₃
Conductor material	Au
Normal operation temperature	200 °C
Max allowable temperature	500 °C
Number of conductive layers (first set of sensors)	10
Number of conductive layers (second set of	40

sensors, optimal value)	
Number of conductive layers (second set of sensors, minimum value)	30
Thickness of one ceramic layer (suggested value)	300 μm
Conductor lines layout	racetrack
Conductor line width (suggested value)	400 μm
Conductor line thickness (minimum value)	10 μm
Conductor line spacing (suggested value)	200 μm
Insulation withstand voltage to ground	>1kV

Table 16: design parameters and reference requirements for the Au prototype sensors

The first set of three 10-layer Au LTCC prototype sensors, complete with Au terminal wires, was delivered by Linkra to Consorzio RFX in January 2009. During the magnetic and electrical tests at RFX the welding of the terminal wires of two prototypes was broken, following the application of a limited mechanical stress (see 3.2.8). The broken prototype sensors were sent back to Linkra for repair at the beginning of February 2009 and re-delivered to RFX in July 2009.

Due to the difficulties met in the building of 40 layers prototype sensors only one sample of the second set (40 layers) was delivered in July 2009. Since the failure rate in the manufacturing of 40 layer sensors was too high (4 sensors out of a total of 5 attempts resulted cracked after the curing in oven at 850°C), it was decided, in accordance with RFX, to go ahead with the manufacture of 7 LTCC sensors having 30 layers instead of 40.

As explained by Linkra, several specific precautions have been taken regarding non-uniform shrinkage during firing, misalignment of layers, non-uniform thickness of conductive lines and stray magnetic areas, since the number of layers required for

obtaining the equivalent area required is larger than that usually produced with LTCC technology. According to the declarations of conformance and test report sheets provided by Linkra the shrinkage of the LTCC ceramic layers during firing is 27% (the green type sheets have reduced from 254 to 200 μ m thickness).

Table 17 describes the whole set of sensors, with a unique ID number (indicating the n. of layers and a sequential number), the delivery date and the type of tests executed. The tests carried out on the prototype sensors discussed exhaustively in the following sections are:

- 3.2.1 Dimensional, density and shrinkage analysis
- 3.2.2 Planarity tests
- 3.2.3 Electrical tests: static and dynamic characterization
- 3.2.4 Magnetic tests: main and transverse equivalent area
- 3.2.5 Thermal conductivity tests along the main direction
- 3.2.6 Vacuum out-gassing in ITER relevant conditions
- 3.2.7 Micrographic tests
- 3.2.8 Connection tests on the coil terminals
- 3.2.9 TIEMF measurements

Table 17: sensors identification, delivery date and tests executed ('1.2.n' indicates the Section number of this document where the test is described)

ID	Delivery date	3.2.1	3.2.2	3.2.3	3.2.4	3.2.5	3.2.6	3.2.7	3.2.8	3.2.9
Au-10-1	Dec 2008	√	√	√	√	-	-	√	√	√
Au-10-2	Jan 2009, repaired July 2009	√	√	√	√	√	-	√	√	√
Au-10-3	Jan 2009, repaired July 2009	√	√	√	√	√	√	√	√	√
Au-40-1	July 2009	√	√	√	√	-	-	√	√	√
Au-30-1	Dec 2009	√	√	√	√	-	-	-	√	√
Au-30-2	Dec 2009	√	√	√	√	-	-	√	√	√
Au-30-3	Dec 2009	√	√	√	√	-	-	-	√	-

Au-30-4	Jan 2010	√	√	√	√	-	-	-	√	-
Au-30-5	Jan 2010	√	√	√	√	-	-	-	√	-
Au-30-6	Feb 2010	√	√	√	√	-	-	-	√	√
Au-30-7	Feb 2010	√	√	√	√	-	-	-	√	-

3.2.1 Dimensional, density and shrinkage analysis

The Au LTCC sensors (*Figure 62* to *Figure 64*) have the following nominal dimensions:

- 10 layers: 30 x 40 x 2.7 mm
- 30 layers: 30 x 40 x 6.9 mm
- 40 layers: 30 x 40 x 9.0 mm

Table 18 lists the weight of the LTCC sensors.

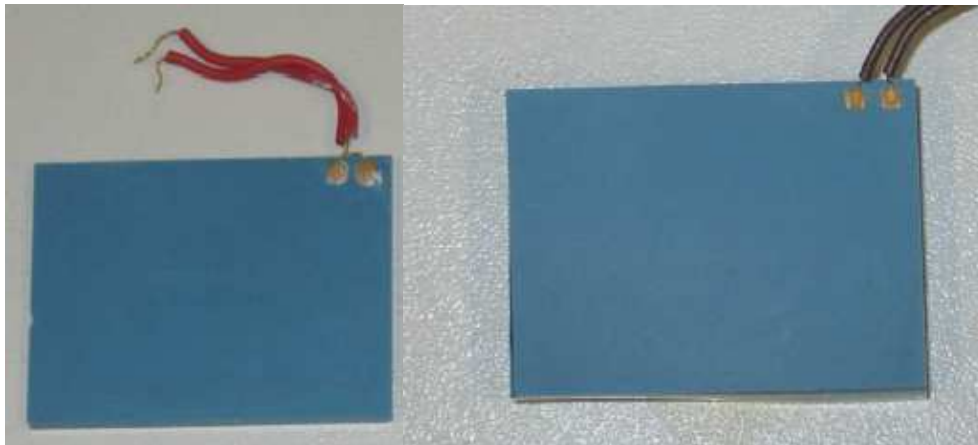


Figure 62 : Au LTCC sensors (10-layer left, 40-layer right)

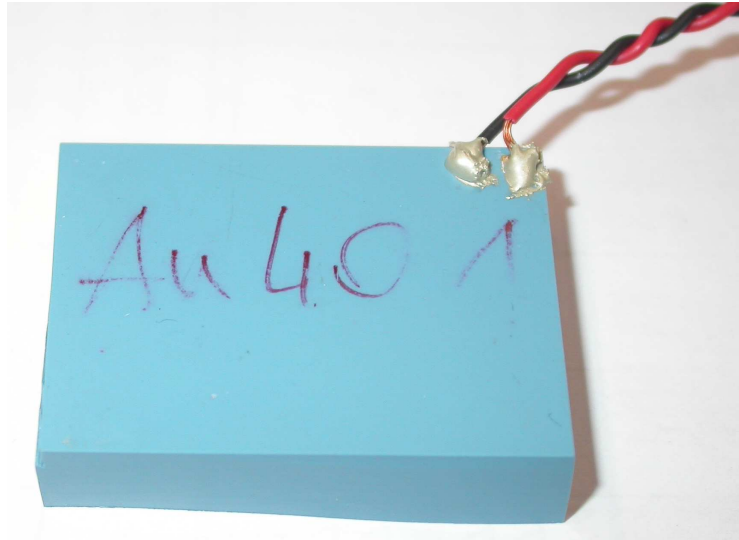


Figure 63 : 40-layer sensor

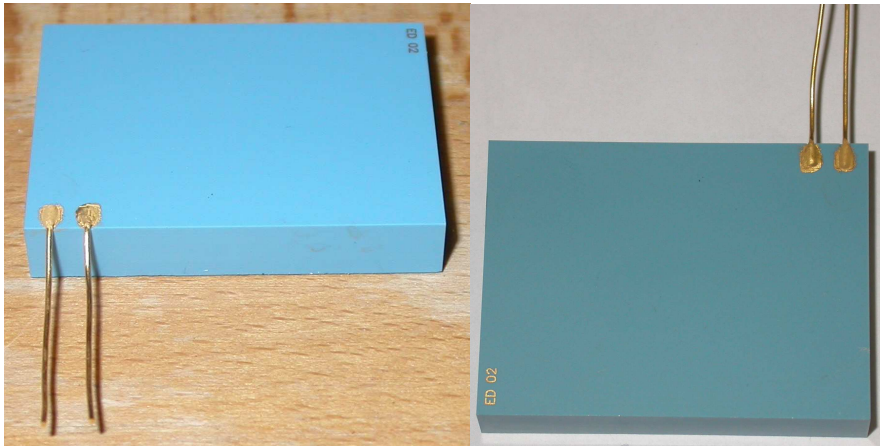


Figure 64 : 30-layer sensor

Table 18: sensors' weight

Sensor	Weight [g]
Au-10-1	11
Au-30-1	28
Au-30-2	28
Au-30-3	28
Au-30-4	28
Au-30-5	28
Au-30-6	27
Au-30-7	28

3.2.2 Planarity tests

A planarity test has been carried out by measuring the maximum and minimum thickness for each LTCC sensor and calculating the deviation as the difference between the two measured values. The thickness of the central point has been measured too. A feeler pin having a resolution of 0.01mm has been used for the test (*Figure 65*).



Figure 65: feeler pin used for the planarity test

Table 19 lists the measured thicknesses for each sensor and the respective deviations (absolute and percentage).

sensor\thickness	Maximum thickness	Minimum thickness	Central thickness	deviation	Percentage deviation
	mm	mm	mm	mm	
Au-10-1	2.70	2.65	2.61	0.09	3.3%
Au-10-2	2.72	2.68	2.65	0.07	2.6%
Au-10-3	2.73	2.69	2.67	0.06	2.2%
Au-40-1	8.99	8.85	8.99	0.14	1.6%
Au-30-1	6.89	6.75	6.8	0.14	2.0%
Au-30-2	6.83	6.73	6.8	0.1	1.5%
Au-30-3	6.85	6.72	6.84	0.13	1.9%
Au-30-4	6.85	6.76	6.85	0.09	1.3%
Au-30-5	6.83	6.76	6.81	0.07	1.0%

Au-30-6	6.84	6.73	6.84	0.11	1.6%
Au-30-7	6.82	6.72	6.82	0.10	1.5%

Table 19: measured thickness and deviations

In the case of 30-layer LTCC sensors the planarity of the transversal sides has been verified too. The four edge points of each transversal side have been verified by measuring their vertical position with respect to a reference point (marked in *Figure 66* by a vertical arrow). The surfaces tested are shown in *Figure 66*.

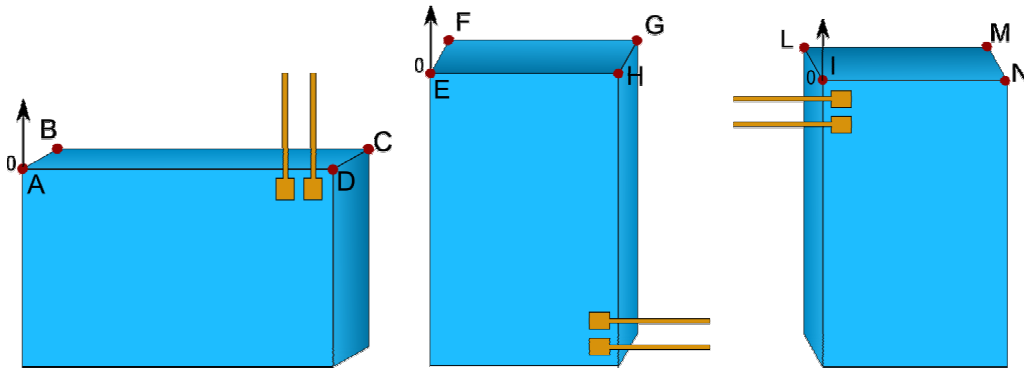


Figure 66: scheme of the planarity tests carried out on the transversal sides of 30-layer sensors

sensor	A [μ m]	B [μ m]	C [μ m]	D [μ m]	E [μ m]	F [μ m]	G [μ m]	H [μ m]	I [μ m]	L [μ m]	M [μ m]	N [μ m]
Au-30-1	0	0	0	0	0	0	2	1	0	0	0	0
Au-30-2	0	150	150	0	0	90	120	-20	0	-150	-170	-20
Au-30-3	0	130	80	30	0	80	60	0	0	-60	-70	10
Au-30-4	0	30	20	20	0	10	-20	-10	0	-10	10	10
Au-30-5	0	-20	-20	0	0	10	20	0	0	20	10	0
Au-30-6	0	30	60	20	0	-20	30	30	0	20	30	-10
Au-30-7	0	90	120	50	0	110	100	10	0	-90	0	40

Table 20: vertical position of the edge points of the transversal sides

The planarity error appears considerable in the case of Au-30-2 and Au-30-3, with a deviation up to 170 μ m. This is probably due to the deflection of the diamond cutting saw used to trim the sensor after curing and this process could be improved.

3.2.3 Electrical tests: static and dynamic characterization

Both static and dynamic electric tests have been carried out on each LTCC sensor in order to find out important parameters such as the insulation withstand voltage (dielectric

strength), the static resistance, the equivalent inductance and capacitance, the resonance frequency and the bandwidth.

3.2.3.1 Insulation withstand voltage

The insulation withstand voltage was measured by wrapping the outer surface of the LTCC sensor with a aluminum foil and applying a voltage up to 5kV between one terminal and the grounded foil (**Figure 28**). The procedure for the measurement of the insulation withstand voltage is the same already used for Ag LTCC sensors (3.1.2.1).

Sensor\Voltage	SATURN ISO				ABB METRISO	
	100 V	250 V	500 V	1000 V	2500 V	5000 V
Au-10-1	>3GΩ	>3GΩ	>30GΩ	>30GΩ	>20GΩ	Surface discharge occurred
Au-10-2	>3GΩ	>3GΩ	>30GΩ	>30GΩ	>20GΩ	Surface discharge occurred
Au-10-3	>3GΩ	>3GΩ	>30GΩ	>30GΩ	>20GΩ	Surface discharge occurred
Au-30-1	>3GΩ	>3GΩ	>30GΩ	>30GΩ	>20GΩ	Surface discharge occurred
Au-30-2	>3GΩ	>3GΩ	>30GΩ	>30GΩ	>20GΩ	Surface discharge occurred
Au-30-3	>3GΩ	>3GΩ	>30GΩ	>30GΩ	>20GΩ	Surface discharge occurred
Au-30-4	>3GΩ	>3GΩ	>30GΩ	>30GΩ	>20GΩ	Surface discharge occurred
Au-30-5	>3GΩ	>3GΩ	>30GΩ	>30GΩ	>20GΩ	Surface discharge occurred
Au-30-6	>3GΩ	>3GΩ	>30GΩ	>30GΩ	>20GΩ	discharge occurred
Au-30-7	>3GΩ	>3GΩ	>30GΩ	>30GΩ	>20GΩ	discharge occurred
Au-40-1	>3GΩ	>3GΩ	>30GΩ	>30GΩ	>20GΩ	Surface discharge occurred

Table 21: Insulation resistance values of Au LTCC sensors

3.2.3.2 Static and dynamic electric characterization

Table 22 displays the values of the electric resistance measured in static conditions by the ABB METRAWATT GmbH instrument.

LTCC sensor	R [Ω]
Au-10-1	132.3
Au-10-2	129.5
Au-10-3	128.1

Au-30-1	368.0
Au-30-2	388.3
Au-30-3	375.2
Au-30-4	377.8
Au-30-5	375.3
Au-30-6	434.0
Au-30-7	437.0
Au-40-1	493.0

Table 22 : values of the static electric resistance

The sensor dynamic behavior is equivalent to that of a circuit constituted by the series of an inductance and a resistance in parallel with a capacitance (Figure 29). Table 23 displays the values of the equivalent resistance, capacitance and inductance of the LTCC sensors together with the resonance frequencies. The above mentioned parameters have been measured by the HP4194 impedance analyzer.

Sensor	Req [Ω]	Leq [μH]	Ceq [pF]	Resonance frequency [Hz]
Au-10-1	1.32E+02	7.35E+02	4.28E+01	8.98E+05
Au-10-2	1.30E+02	7.33E+02	3.66E+01	9.72E+05
Au-10-3	1.31E+02	7.32E+02	3.65E+01	9.74E+05
Au-40-1	4.96E+02	8.95E+03	1.19E+01	4.89E+05
Au-30-1	5.78E+02	5.48E+03	1.52E+01	5.52E+05
Au-30-2	3.87E+02	5.51E+03	1.52E+01	5.50E+05
Au-30-3	3.74E+02	5.49E+03	1.52E+01	5.52E+05
Au-30-4	3.80E+02	5.49E+03	1.54E+01	5.48E+05
Au-30-5	3.74E+02	5.49E+03	1.54E+01	5.47E+05
Au-30-6	4.36E+02	5.49E+03	1.56E+01	5.44E+05

Table 23: electric parameters of the LTCC sensor equivalent circuit

Figure 67 shows the bode diagram of the impedance Z_{eq} of the equivalent circuit (calculated according to the values of Req, Leq and Ceq determined).

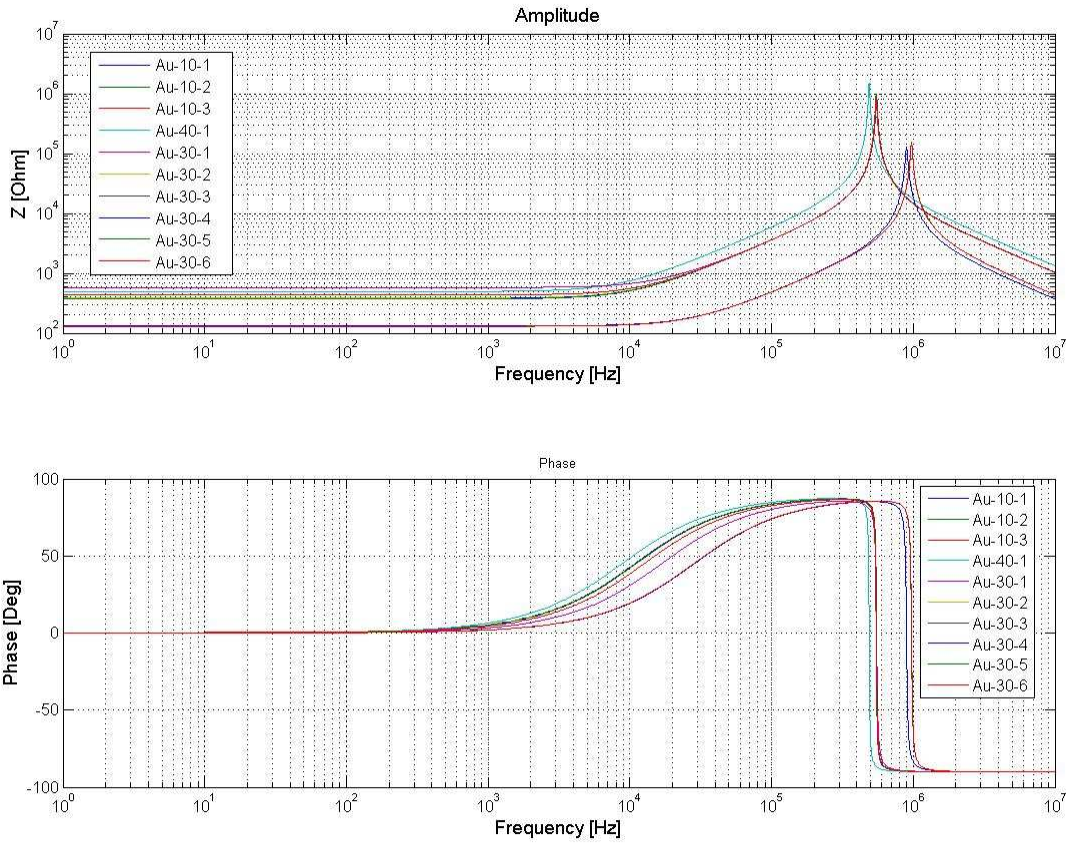


Figure 67: Amplitude and phase of the equivalent impedance of the LTCC pick-up coils

The bandwidth of the measuring probe consisting of LTCC sensor and acquisition system has been calculated referring to the equivalent circuit shown in **Figure 31** (see 3.1.2.2).

Figure 68 shows the amplitude of the transfer function of the measuring probe (LTCC including the input resistance of the acquisition system) while **Table 24** lists the cut off frequencies.

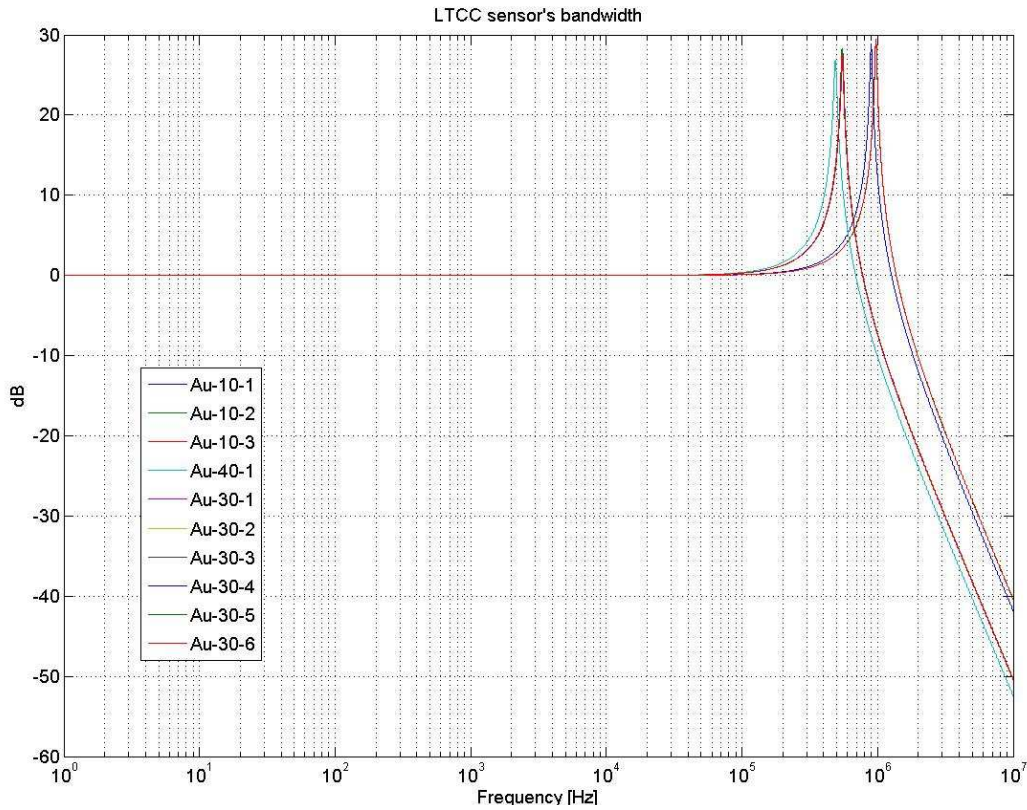


Figure 68: Amplitude of the frequency response of the LTCC magnetic probe

LTCC sensor	Cut off frequency (-3dB) [MHz]
Au-10-1	1.39
Au-10-2	1.51
Au-10-3	1.51
Au-40-1	0.759
Au-30-1	0.856
Au-30-2	0.854
Au-30-3	0.856
Au-30-4	0.850
Au-30-5	0.850
Au-30-6	0.850

Table 24 : cut off frequencies of measuring probe (LTCC sensor and integrator)

3.2.4 Magnetic tests: main and transverse equivalent area

The equivalent magnetic areas of the LTCC sensors, main and transverse, have been calculated in order to evaluate the sensitivity to magnetic fields along the main and transverse direction of the sensor. The procedure for the magnetic calibration is the same already used for Ag LTCC sensors (3.1.3).

The LTCC sensors were fixed on a calibrated support in order to obtain a good alignment with respect to the direction of the imposed magnetic field B . The value of the field is proportional to the current I inside the solenoid, where the constant of proportionality is $k = B/I = 0.0009642 \text{ T/A}$.

3.2.4.1 10-layer sensors

Figure 69 and Figure 70 show the equivalent area, main and transverse, Vs frequency for the 10- layers LTCC sensors. A general comment is given in Section 2.4.4.

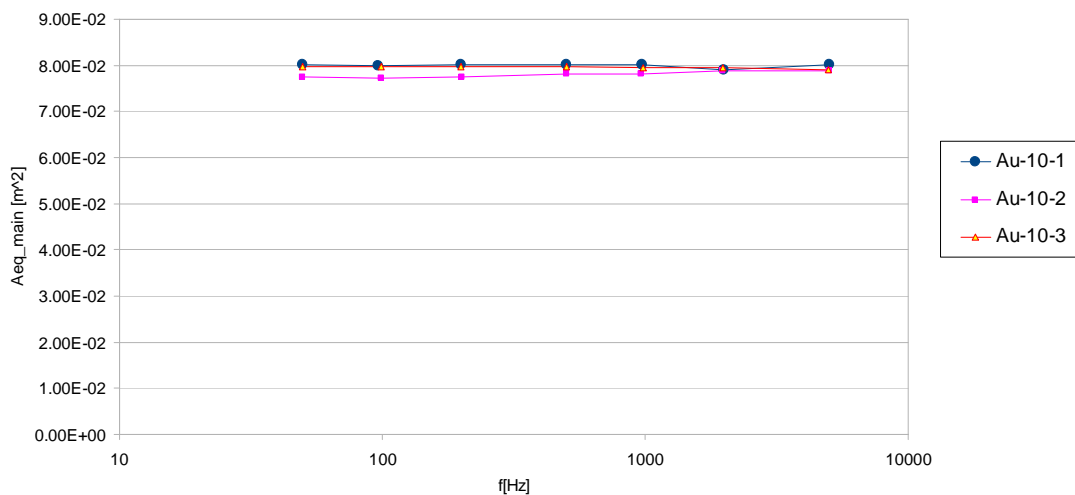


Figure 69 : main equivalent area of 10-layer LTCC sensors

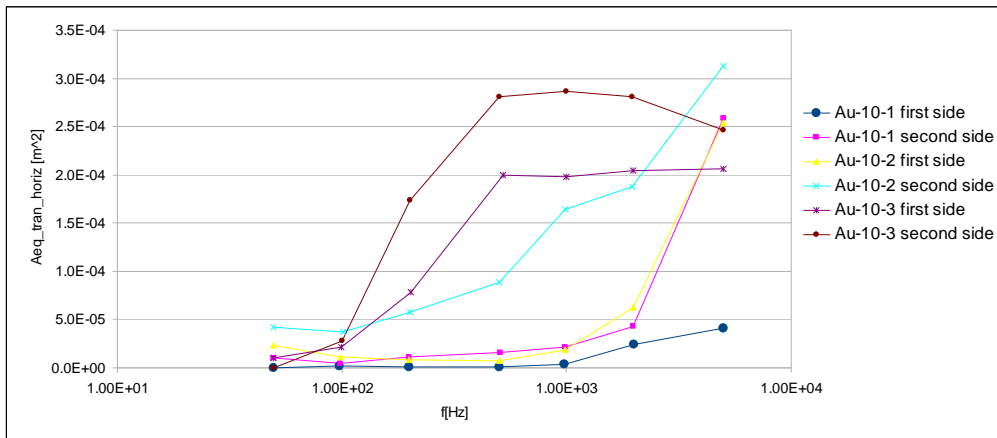


Figure 70: transverse equivalent area of 10-layer LTCC sensors, both sides

3.2.4.2 40-layer sensors

Figure 71 and Figure 72 show the equivalent area, main and transverse, Vs frequency for the 40-layer LTCC sensors. A general comment is given in 3.2.4.4.

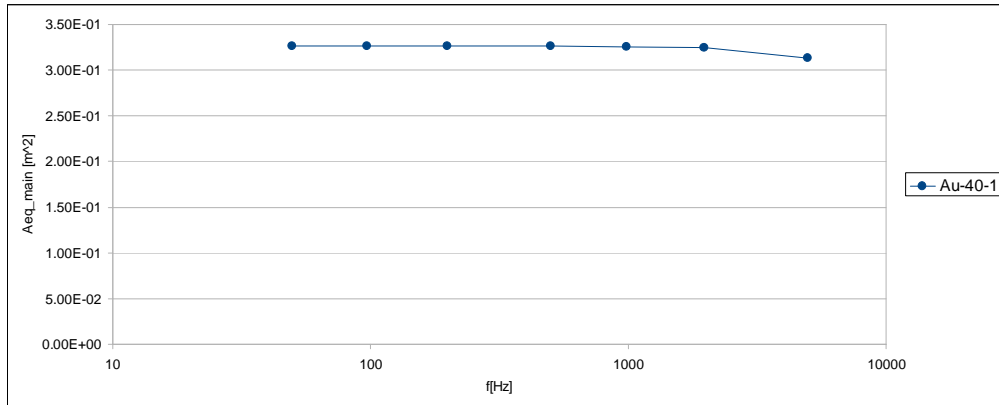


Figure 71: main equivalent area of the sensor Au-40-1

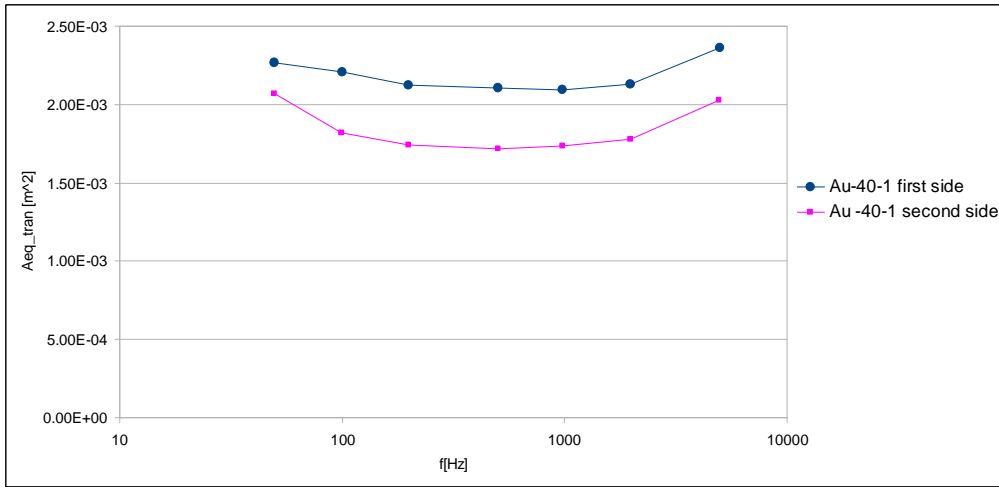


Figure 72: transverse equivalent area of the sensor Au-40-1, both sides

3.2.4.3 30-layer sensors

Figure 73 and Figure 74 show the equivalent area, main and transverse, Vs frequency for the 30-layer LTCC sensors. A general comment is given in 3.2.4.4.

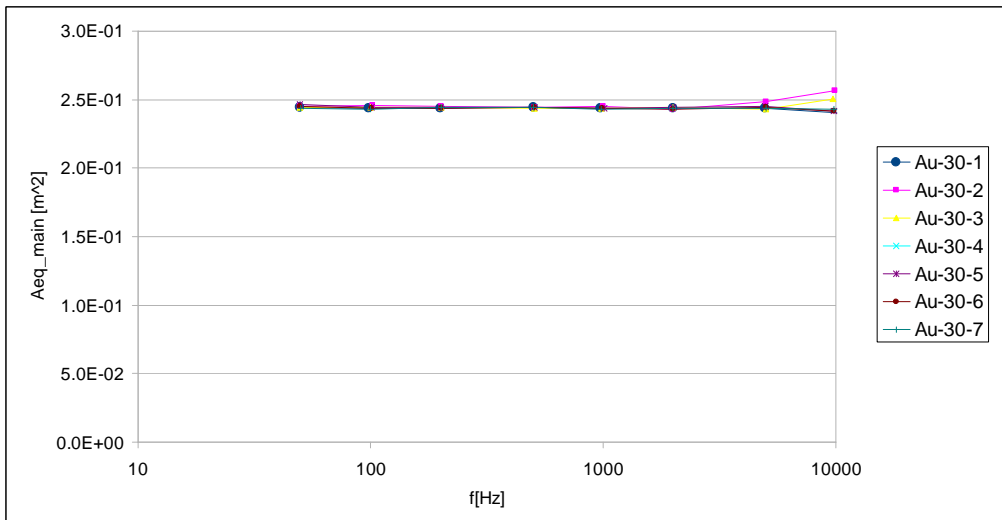


Figure 73: main equivalent area of 30-layer LTCC sensors

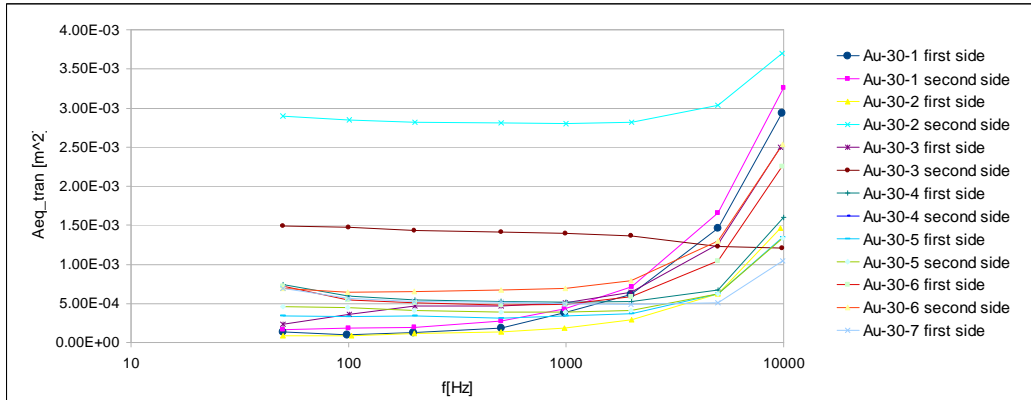


Figure 74: transverse equivalent area of 30-layer LTCC sensors, both sides

3.2.4.4 Final considerations

Table 25 lists the values of the main and transverse equivalent area at 100Hz for each sensor and the maximum $A_{\text{transverse}}/A_{\text{main}}$ ratio. The magnetic equivalent area of the sensors are fully satisfactory, since along the main direction it is consistent with the geometrical characteristics of the winding and along the transverse direction is <1%.

The increase of magnetic area at higher frequency along the transverse direction (in particular **Figure 70** and **Figure 74**) could be due to a local deformation of the magnetic field in the proximity of the sensor, owing to the aluminum foil which was wrapped around the sensor to shield the sensor from the background electromagnetic noise.

The evident higher transverse area of some cases (for instance Au-30-2 and Au-30-3 in **Figure 74**) are probably due to a not optimal alignment of the sensor within the calibration rig rather than to a misalignment of the conductor layers within the LTCC sensors.

Sensor	Main Area [m ²]	Transverse area first side [m ²]	Transverse area second side [m ²]	Maximum $A_{\text{transverse}}/A_{\text{main}}$
Au_10_1	8.00E-02	1.69E-06	5.06E-06	0,0%
Au_10_2	8.02E-02	1.12E-05	3.75E-05	0,0%
Au_10_3	7.97E-02	2.15E-05	2.77E-05	0,0%
Au_40_1	3.27E-01	2.21E-03	1.82E-03	0,7%
Au_30_1	2.44E-01	1.02E-04	1.81E-04	0,1%
Au_30_2	2.45E-01	9.00E-05	2.85E-03	1,2%
Au_30_3	2.44E-01	3.57E-04	1.47E-03	0,6%
Au_30_4	2.45E-01	5.95E-04	6.49E-04	0,3%
Au_30_5	2.45E-01	3.33E-04	4.50E-04	0,2%
Au_30_6	2.44E-01	5.44E-04	6.48E-04	0,3%

Au_30_7	2.43E-01	5.65E-04	-	0,2%
---------	----------	----------	---	------

Table 25: average values of main and transverse area and the maximum $A_{transverse}/A_{main}$ ratio

3.2.5 Thermal conductivity tests along the main direction

The procedure of the experiment and the mathematical model adopted are the same already used in the case of Ag LTCC sensors and can be found in 3.1.4: two LTCC sensors were tightened between two copper bars that play the role of thermal sinks. The LTCC sensors were connected in series and fed by an electric generator. The heat by Joule effect inside the sensors produces a thermal flux along the main direction of the sensors, from the center to the thermal sinks. The experiment was carried out on 10-layer LTCC sensors only.

A one-dimensional model has been used to describe the thermal conduction across the thickness of the two sensors, the heat flux assumed normal to the plain section of the LTCC sensor. Thanks to the limited thickness of the LTCC sensors (2.7 mm), the fraction of the heat flowing out from lateral sides by thermal convection with air can be neglected.

The instrumentation used is the same already used in the case of the Ag LTCC sensors.

The Voltage drop (imposed by the electric generator KEPCO BOP power supply) was 45.6V while the average current flowing inside the LTCC sensors was about 0.174A, depending on the actual sensor temperature. The resulting generated thermal power was $q=7.94W$.

The equivalent thermal conductivity of the sensor has been calculated on the basis of the one-dimensional analytical model (equation (5)) :

$$\lambda = \frac{H}{2(T_2 - T_1)} L^2 = 2.1 \text{ W m}^{-1} \text{ K}^{-1}$$

where H is the internal heat generation power per unit volume, T_1 is the average temperature of the sink, T_2 is the temperature of the central point and L is the thickness of one sensor (2.7mm).

The measured value of the thermal conductivity λ is slightly smaller than the one declared by DuPont in the DuPont 951 Green Tape product description which is

$$\lambda_{datasheet} = 3.3 \frac{W}{mK}.$$

The same final considerations about the reliability of the thermal test already indicated for Ag LTCC sensors are valid in the case of Au sensors too.

3.2.6 Vacuum out-gassing in ITER relevant conditions

The procedure of the experiment and the mathematical model adopted are the same already used in the case of Ag LTCC sensors and can be found in 3.1.4. The experiment set-up is shown in *Figure 48* and *Figure 49* while the baking cycle is shown in *Figure 51* and *Figure 52*. The test has been carried out on the sensor Au-10-3 only.

Table 26 reports the results of the experiment at the end of the baking cycle; the out-gassing rate of the LTCC sensor is obtained by the difference with the empty chamber OR value.

	Empty chamber * 10⁻⁹ [Pa m³/s]	Au-10-3 sensor * 10⁻⁹ [Pa m³/s]
120 °C	7.3	14 – 7.3 = 6.7
30 °C	0.7	3.0 - 0.7 = 2.3

Table 26: Absolute OR of 10-layer sensor and empty chamber

Figure 53 shows the measured pressures and the calculated OR for the empty chamber while Figure 75 shows pressures and OR for the Au-10-3 sensor.

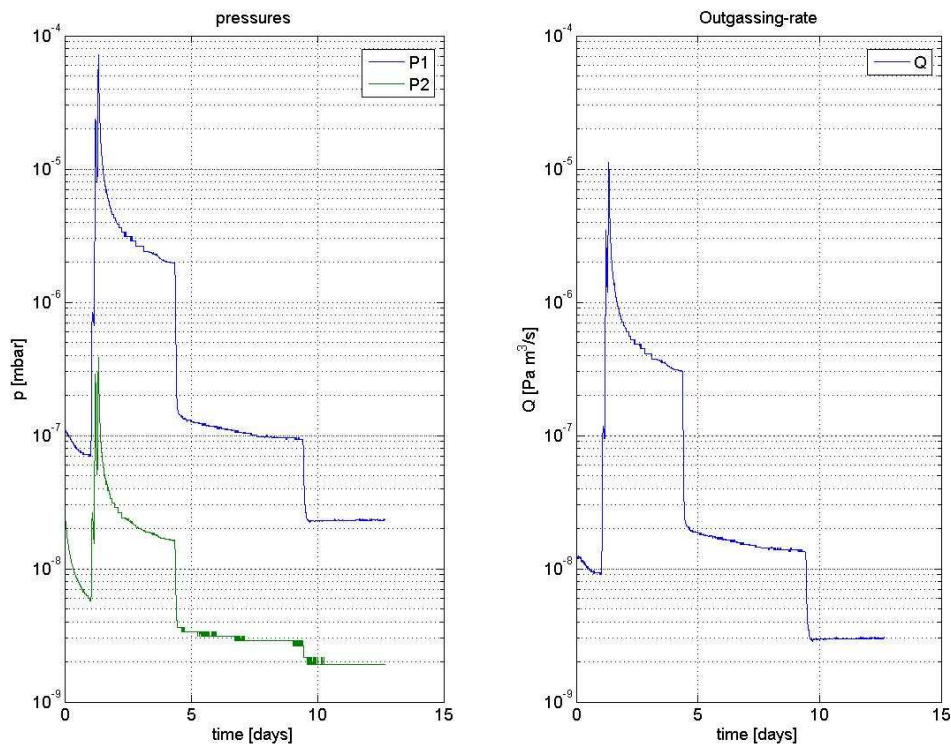


Figure 75: Measured pressures (left) and OR evaluated (right), Au-10-3 sensor

As in the case of Ag LTCC sensors pure H_2 has been considered as out-gassed substance and this choice determines an overestimation of the out-gassing rate.

3.2.7 Micrographic tests

3.2.7.1 Layer-to-layer alignment

The alignment of LTCC sensor Au conductive lines (10-layer and 40-layer) has been verified using x-ray imaging (**Figure 76** and **Figure 77**) and micrographic images of sectioned sensors (**Figure 79**). The tolerance in the positioning of the conductive lines and vias is sufficient to ensure a reliable connection of the different layers (**Table 27**).

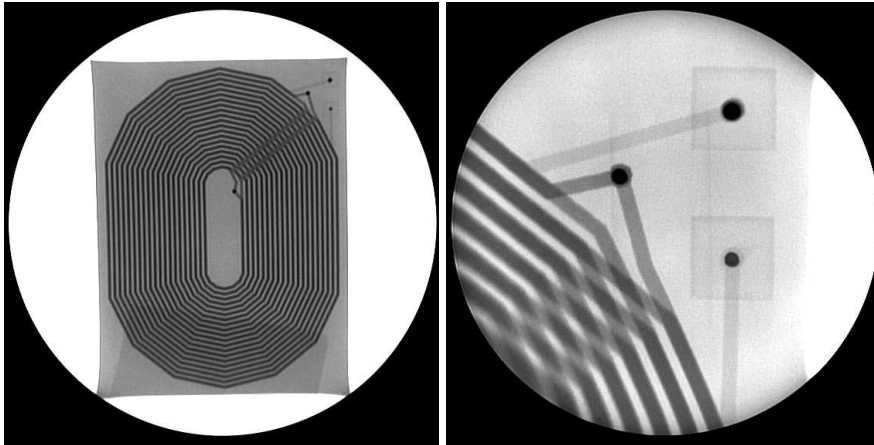


Figure 76: x-ray picture of 10-layer LTCC sensor showing the actual layout of conductor connections (detail of the connection pad on the right)

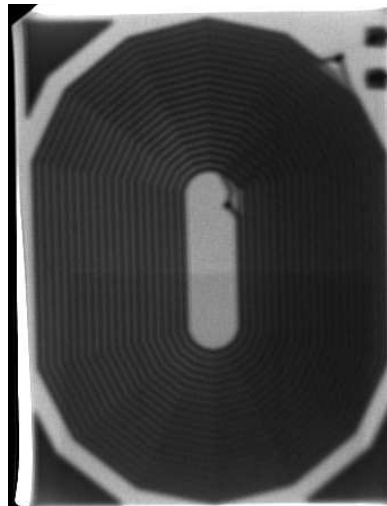


Figure 77: x-ray picture of 40-layer LTCC sensor showing the actual layout of conductor connections

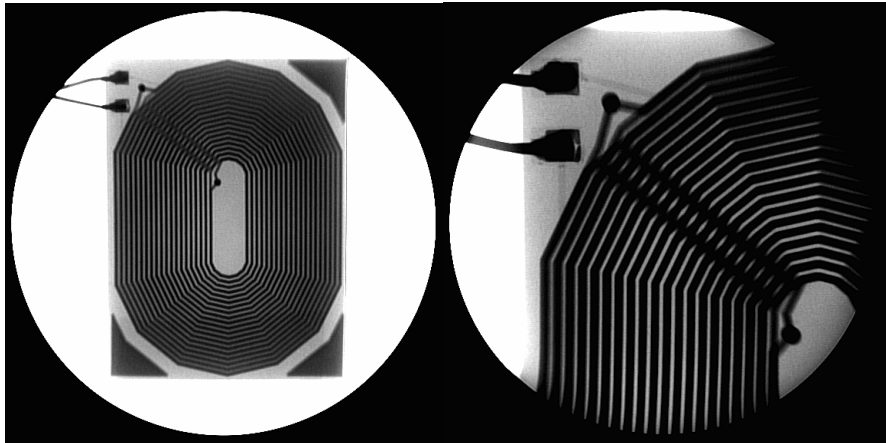


Figure 78: x-ray picture of 30-layer LTCC sensor showing the actual layout of conductor connections (detail of the pad connection on the right)

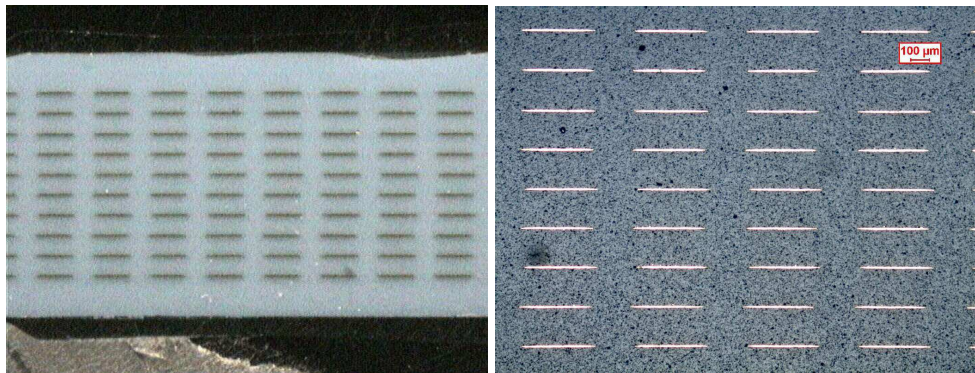


Figure 79: pictures of 10-layer LTCC sensor cross-section

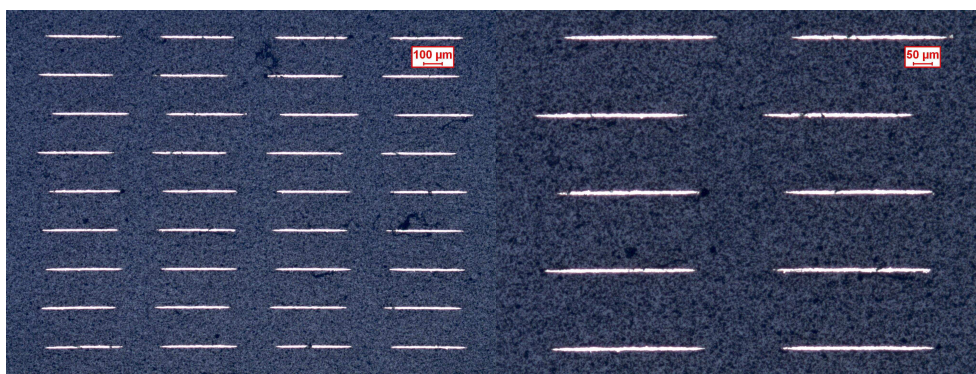


Figure 80: pictures of 40-layer LTCC sensor cross-section

Table 27 displays the cross-section characteristics of one of the 10-layer LTCC sensors and of the 40-layer sensor.

Number of layers	10	40
Number of turns per layer	20	20
Offset between layers	433 μm	495 μm
Layer thickness	201 \pm 5 μm	199 \pm 1 μm
Distance between conductive lines	210 \pm 5 μm	204 \pm 8 μm
Thickness of conductive lines	8.5 \pm 1 μm	8.1 \pm 0.6 μm
Width of conductive lines	385 \pm 5 μm	404 \pm 10 μm

Table 27: characteristics of 10-layer and 40-layer LTCC sensor cross-section

3.2.7.2 Composition

SEM-EDS analyses have been carried out to characterize the ceramic and the conductors of the LTCC sensors. The ceramic (DuPont 951) is a mixture of alumina and silica glass, containing small percentage of Pb, Zr and Ca.

External surface composition (ceramic)

Figure 81 displays two enlargements of the external surface of the LTCC sensor (2000X enlargement on the left and 7000X on the right) while Figure 82 shows the composition of the surface.

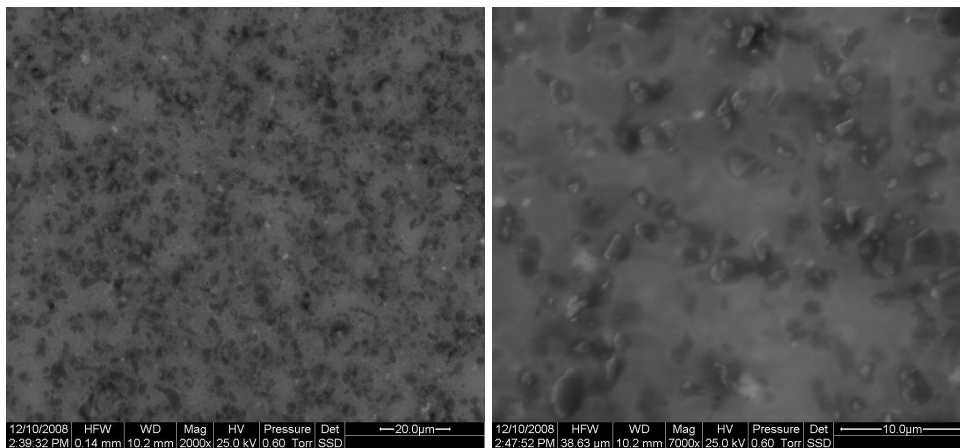


Figure 81: external surface enlargement (2000X enlargement on the left and 7000X on the right)

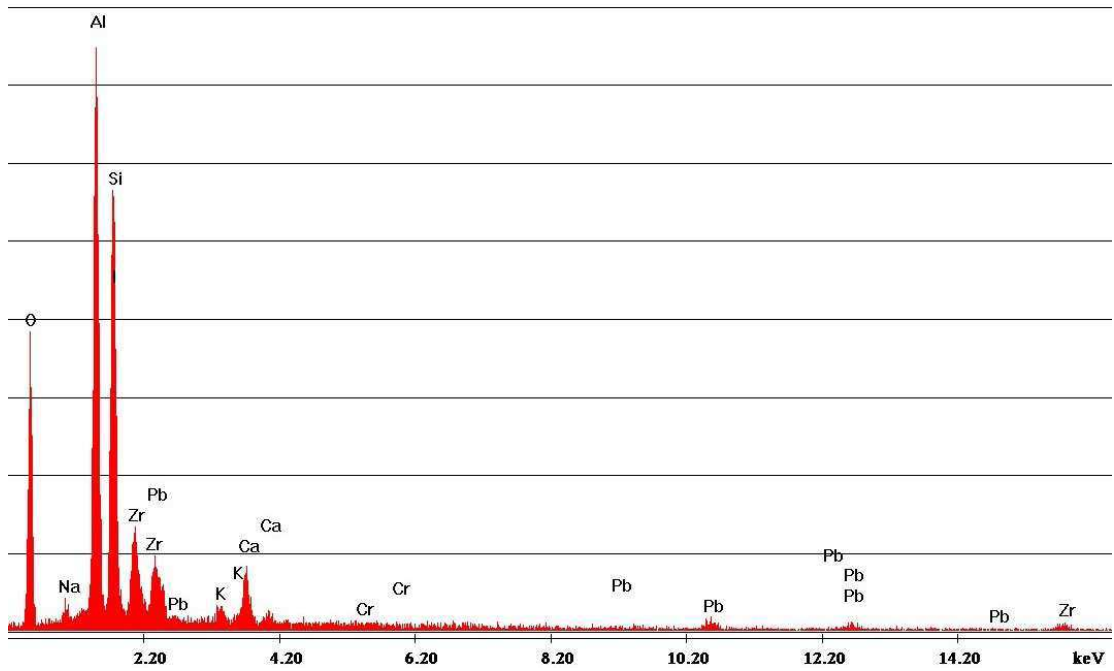


Figure 82: composition of DuPont 951 ceramic (external surface)

Au connecting pads composition

Figure 83 displays two enlargements of the surface of one Au connecting pad (100X enlargement on the left and 300X on the right) while Figure 84 shows the composition of the connecting pad.

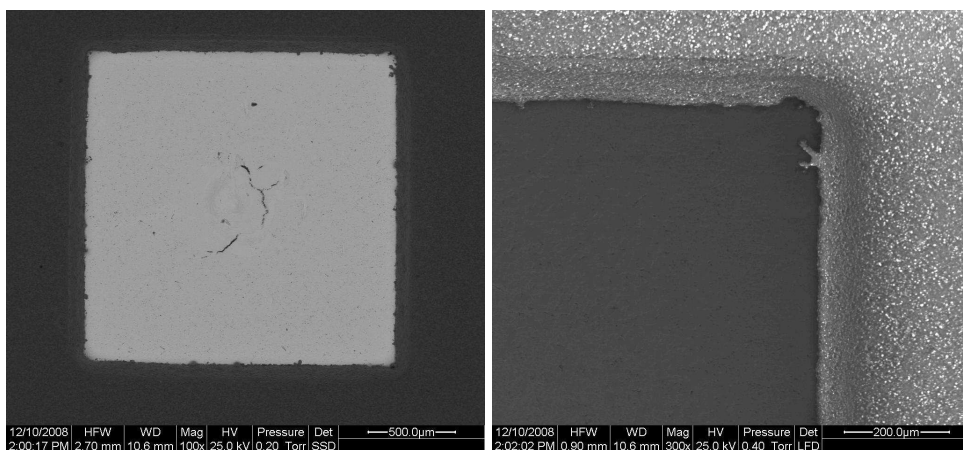


Figure 83: enlargements of one Au connecting pad (100X enlargement on the left and 300X on the right)

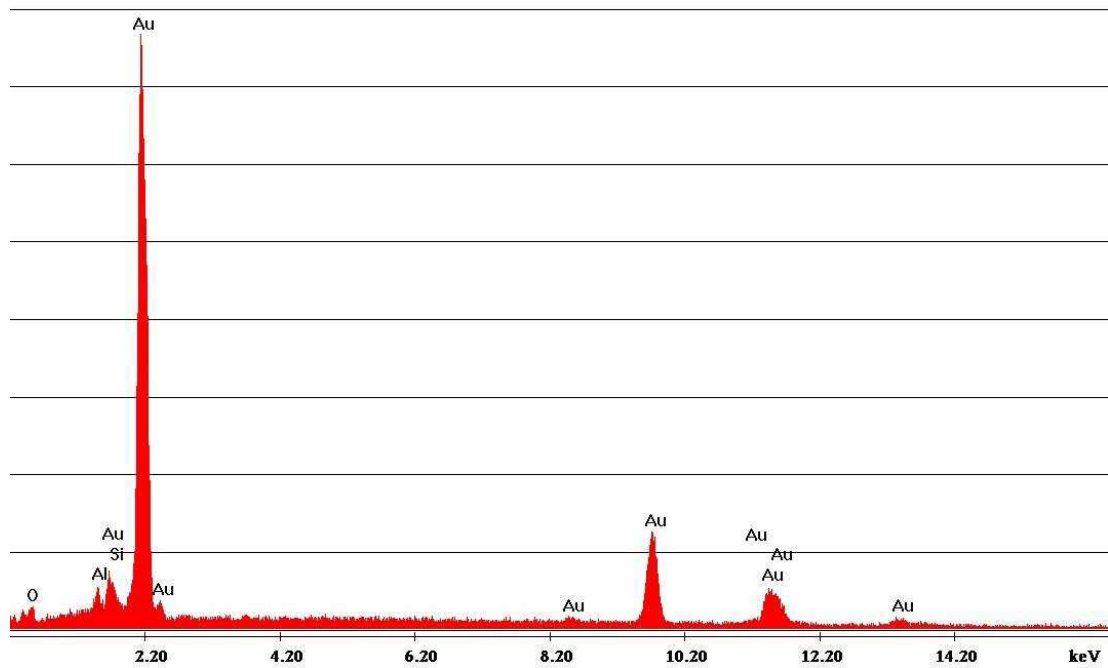


Figure 84: Au connecting pad composition

Cross-section composition (ceramic and conductive lines)

Figure 85 shows the composition of the inner conductive lines at the cross-section while Figure 86 shows the composition of the ceramic (at the cross-section).

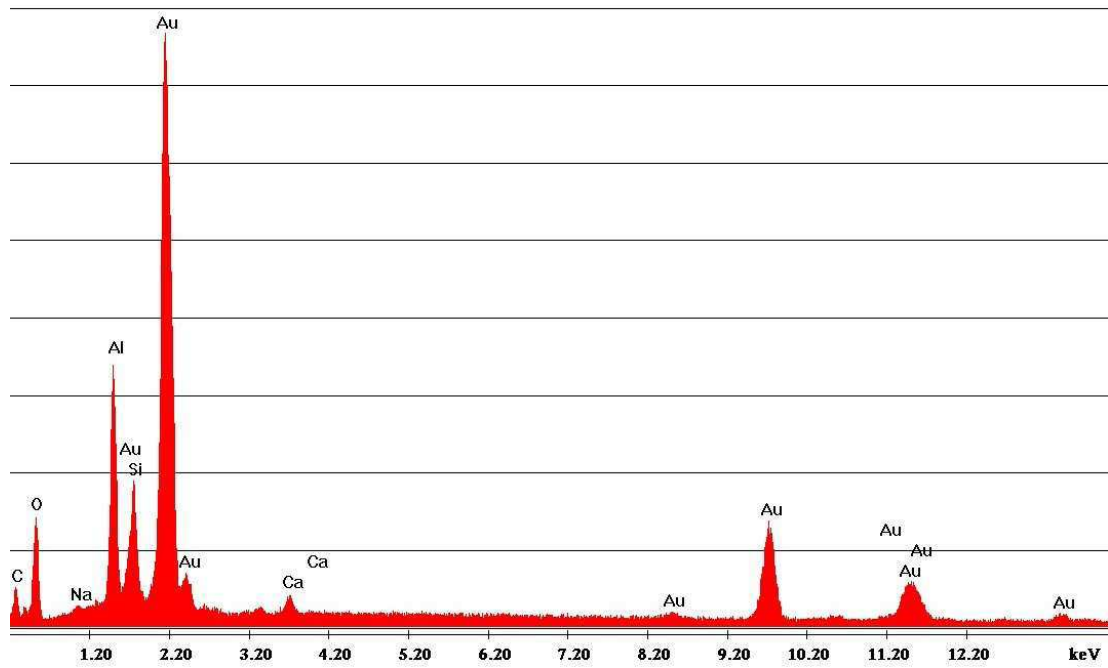


Figure 85: inner conductive lines composition

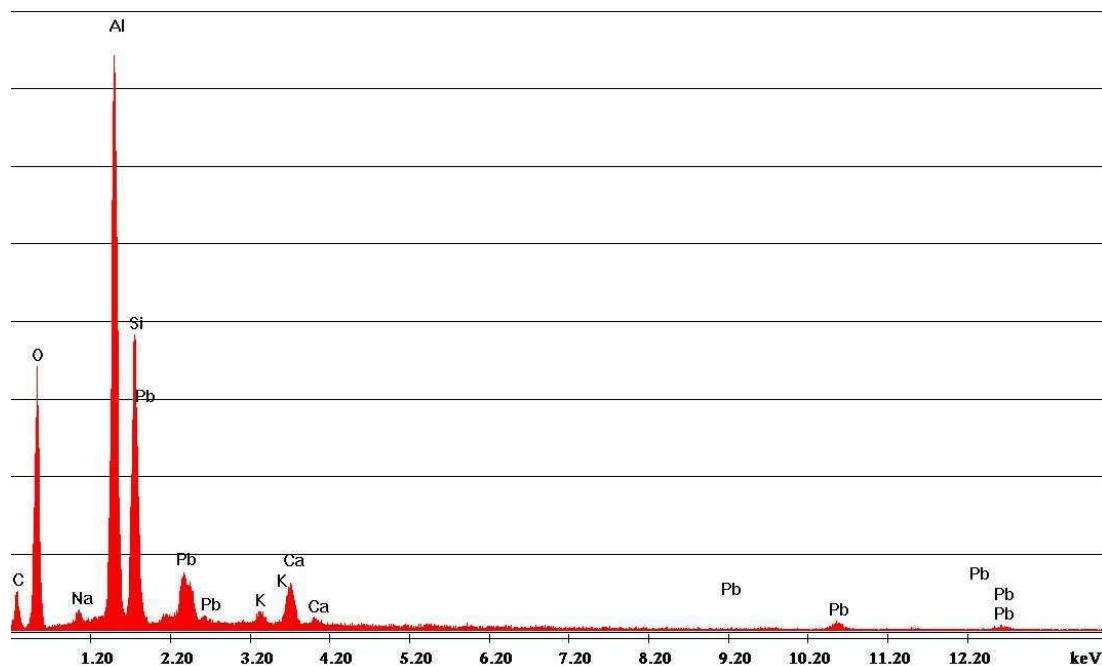


Figure 86: cross-section composition (ceramic)

3.2.8 Appropriate connection tests on the coil terminals

Terminal wires of Au LTCC sensors have been initially welded to the pads using a metallic paste, the same used for the vias, and cured in oven at 850°C. The diameter of the Au wires was 1 mm. Unlike the case of Ag sensors, the welded connection of terminal wires to the pads resulted porous after welding, evidencing an unacceptably weak mechanical resistance.

A list of comments regarding the welded connection is presented below:

- A very small force (few tens of grams, applied at the end of the conductor) proved to be sufficient to break the welded connection
- An initial detachment at the interface between the welding material and the metallic pad was probably the cause of the failure
- The welding materials appears to be porous and cracked in several places (Figure 88)

- One or more gas bubbles appear to have been entrapped between the welding material and the metallic pad during the welding process
- The adhesion between the welding material and the metallic surface of pad seems generally poor
- A considerable shrinkage has taken place during welding
- The Au conductor, whose diameter was 1mm, was not deformed during the breakdown of the welded connection, indicating that the breakdown was facilitated by the stress concentration due to the relative high stiffness of the conductor

The welded connection has been accidentally broken (for samples Au-10-1 and Au-10-2) simply handling the sensors (Figure 87). The breaking was due to the excessive mechanical stress upon the welding, produced by the movement of the terminal wires during the normal measurement operations. LTCC sensors have been sent back to Linkra for the repair.

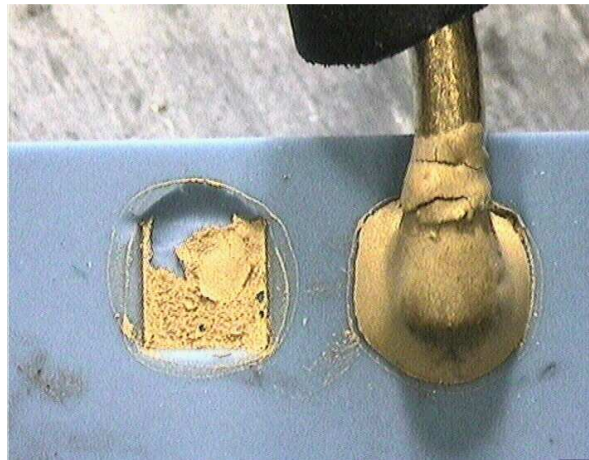


Figure 87 : broke connection between terminal wires and Au pads.



Figure 88 : the welded connection appears to be porous and cracked

In order to reduce the mechanical stress on the LTCC pads a 0.3 mm Au wire has been used for the repair (original Au wires were 1.0 mm). Moreover a different welding technique has been adopted, using both “vias” and “conductor paste” instead of “vias paste” alone and curing in oven at 850°C. The reason for this choice is that "conductor paste" is subjected to considerable shrinkage during curing, but remains compact after curing, whilst "vias paste" does not shrink but remains porous.

The final result appears to be less porous (even if some crack remains) than in the former case, showing a better adhesion to the metallic pads and a less accentuated shrinkage (Figure 89). On the other hand the 0.3 mm Au wire proved weak and not suitable for typical handling operations necessary during measurement sessions, and become the weakness of the terminal connection.

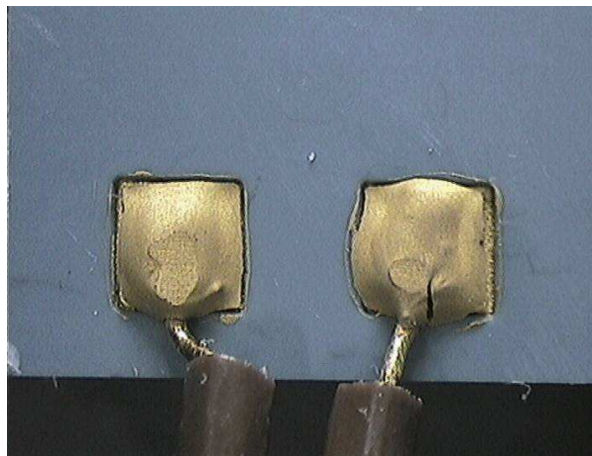


Figure 89 : enlargement of the new welded connection to the pads carried out using both “vias” and “conductor paste”

The weak repair 0.3 mm Au wires broke during the tests (in the case of Au-10-2, Au-10-3 and Au-40-1) and a conductive epoxy resin has been used, as a temporary solution, to weld two flexible copper wires to the pads in order to complete the magnetic measurements (Figure 90). Fortunately all the critical tests, i.e. the "thermally induced electromotive force" (TIEMF) test, which might have been influenced by a non-uniform chemical composition of the conductors, had already been carried out before the occurrence of the failure.



Figure 90 : terminal wires connected by conductive epoxy resin (10-layer left and 40-layer right)

The 30-layer LTCC sensors have been built using Au terminal wires having a diameter of 0.6 mm (instead of the weak 0.3 mm wires). The new connection appears robust and the wires can now be handled without the danger of breaking either the welding or the Au wires themselves. This appears a good compromise and reduces meaningfully the stress in the Au pads.

3.2.8.1 Discussion

As described above, the welding of the Au terminal wires to the metallic pads, in the case of Au LTCC sensors, proved more problematic than in the case of Ag sensors. Anyway, the problem has been solved by using two metallic pastes instead of one and reducing the diameter of the wires (0.6 mm instead of 1mm).

3.2.9 TIEMF measurements

The procedure of the experiment is the same already used in the case of Ag LTCC sensors and can be found in 3.1.6.

Figure 91 to **Figure 97** show the TIEMF effect as a function of the thermal drop T_1-T_2 between the two copper bars, measured on 7 sensors.

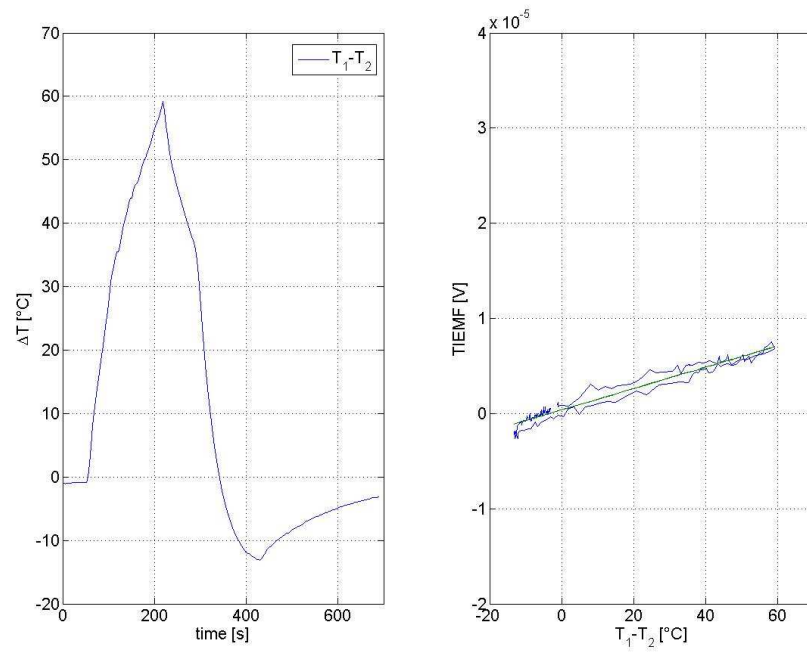


Figure 91 : thermal drop between the two copper sinks (left) and TIEMF effect (right) for the sensor Au-10-1

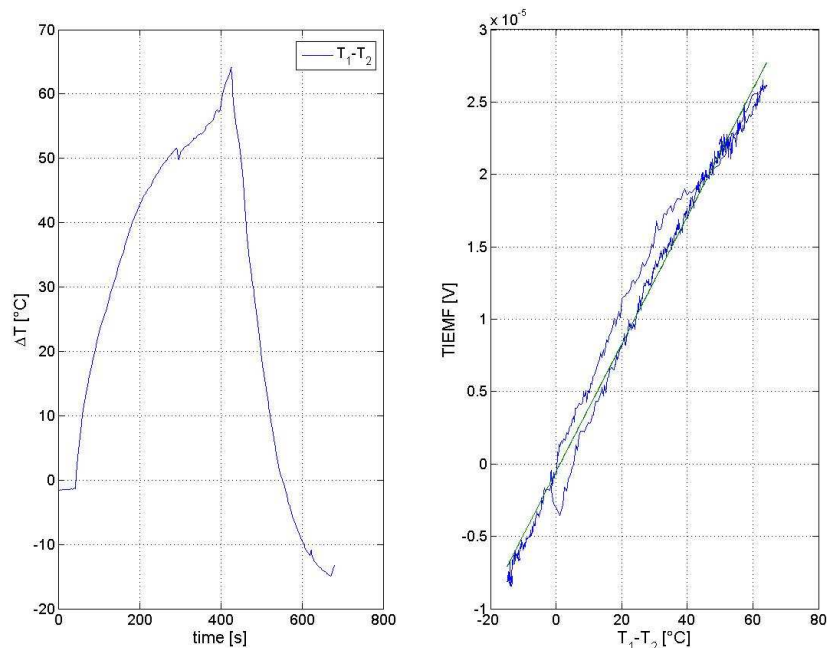


Figure 92 : thermal drop between the two copper sinks (left) and TIEMF effect (right) for the sensor Au-10-2

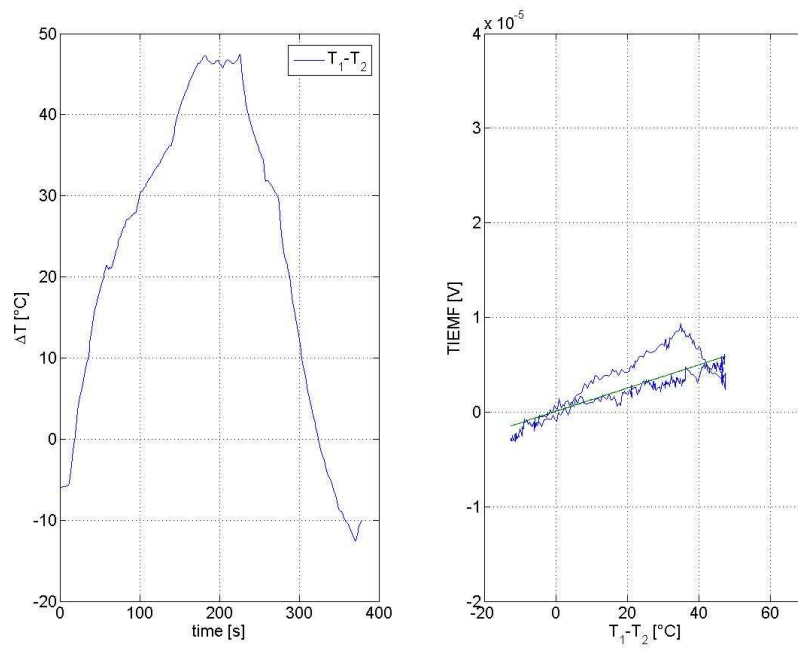


Figure 93: thermal drop between the two copper sinks (left) and TIEMF effect (right) for the sensor Au-10-3

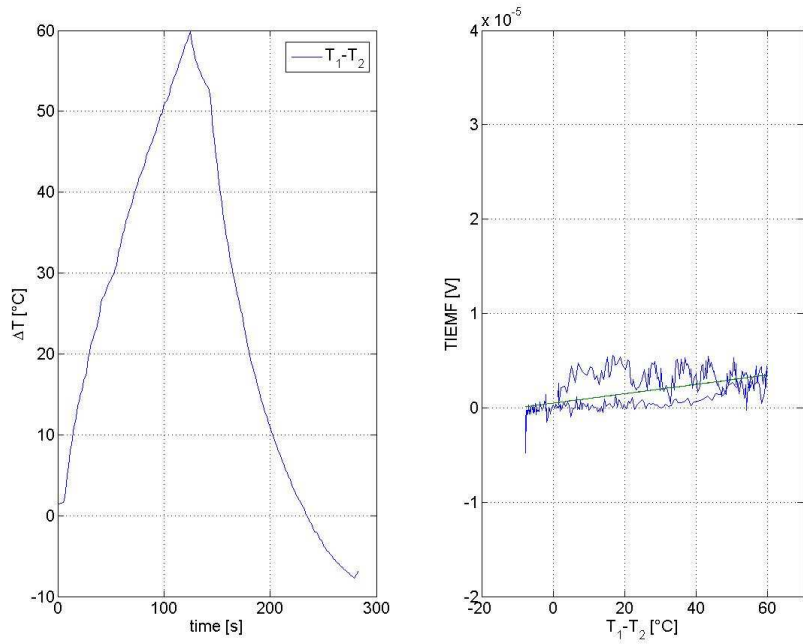


Figure 94: thermal drop between the two copper sinks (left) and TIEMF effect (right) for the sensor Au-40-1

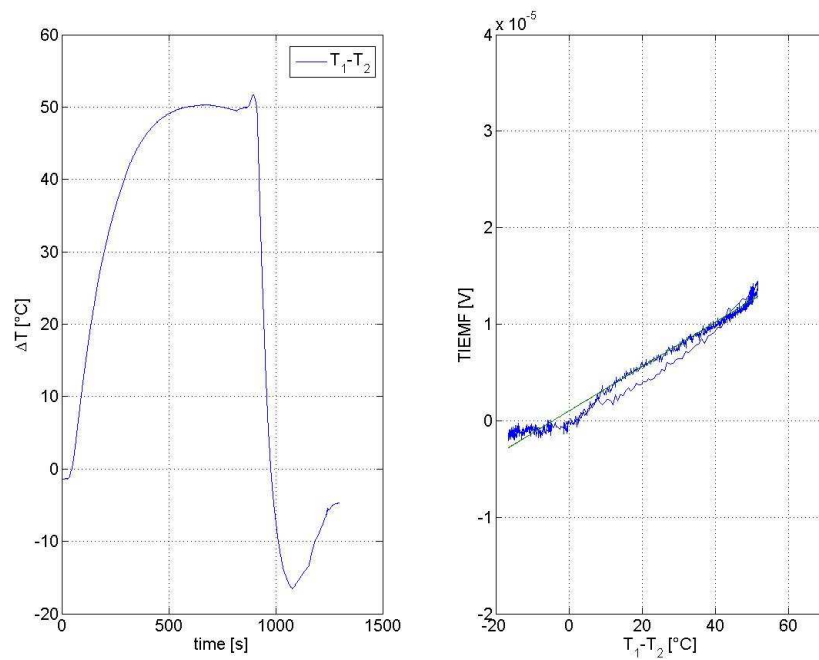


Figure 95: thermal drop between the two copper sinks (left) and TIEMF effect (right) for the sensor Au-30-1

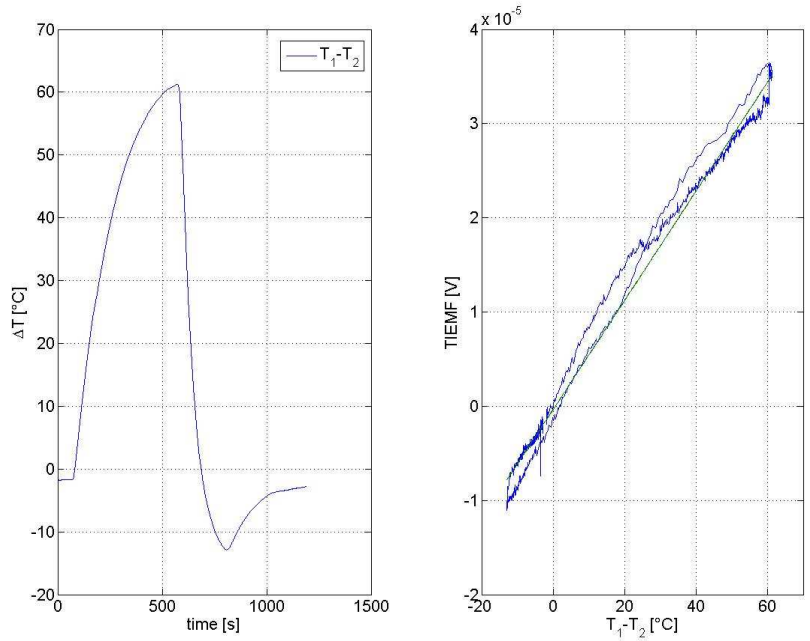


Figure 96: thermal drop between the two copper sinks (left) and TIEMF effect (right) for the sensor Au-30-2

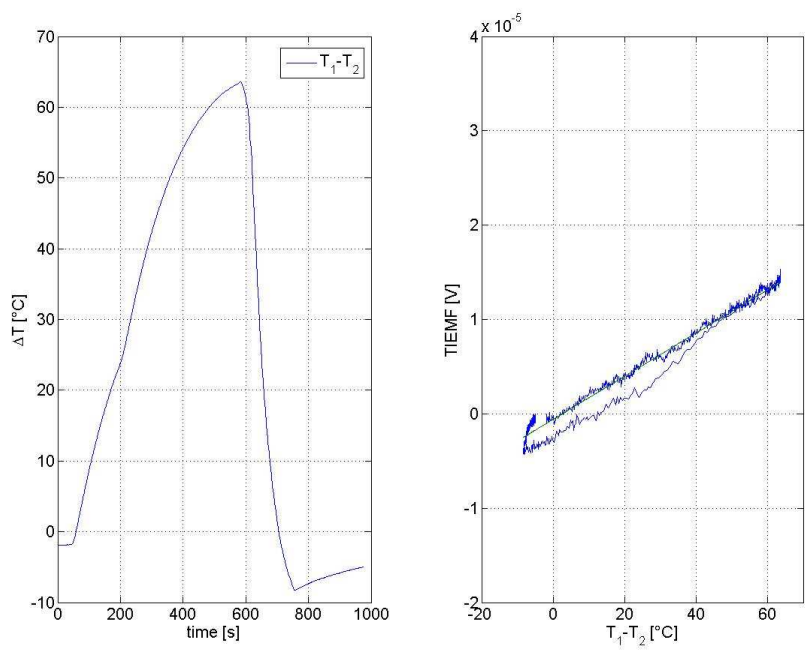


Figure 97: thermal drop between the two copper sinks (left) and TIEMF effect (right) for the sensor Au-30-6

3.2.9.1 Discussion

The TIEMF effect appears much more prominent in the case of Au LTCC sensors than in the case of Ag LTCC sensors, where the TIEMF effect was found to be $<1\mu\text{V}$ with a temperature drop of 60 K (3.1.6).

The TIEMF effect is probably due to the different thermoelectric power of the conductive materials inside the LTCC sensor, i.e. the two metallic pastes used to print the conductive lines (track paste) and to fill the connecting vias (vias paste). The imposed thermal gradient across the sensor can be considered, with a very good approximation, normal to the main surfaces of the sensor, since the two bulk copper bars assure a uniform temperature on the two external faces. The fraction of the heat flowing out from lateral sides by thermal convection with air can be neglected thanks to the limited thickness of the LTCC sensors.

The thermoelectric voltage between the two end points of a uniform conductor can be calculated according to equation (1), where μ is the thermo-power of the material and T_a and T_b are the temperatures of end points of the conductor.

$$V = \int_{T_a}^{T_b} \mu(T) dT \quad (1)$$

In **Figure 98** the cross-section of a LTCC sensor having 6 conductive layers is schematized. Each track is at uniform temperature since the thermal gradient is normal to the main surfaces of the sensor due to the thermal constraints of the copper sinks. This means that, in the specific conditions realized during the experiment, no thermoelectric voltage should exist between the two junctions of each track and therefore all the thermoelectric potential is generated within the vias.

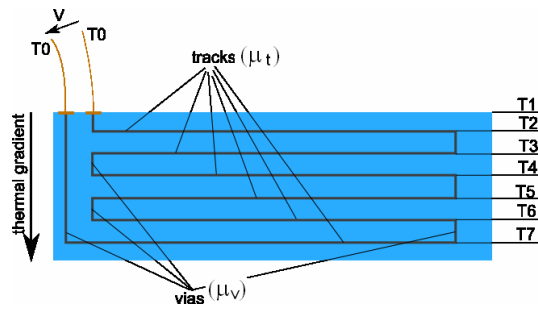


Figure 98: scheme of LTCC sensor internal circuit

Assuming the thermal gradient to be normal to the sensor main surfaces and that the terminal wires are characterized by a constant thermo-power μ_t , if the vias were constituted by a uniform material of thermo-power μ_v , the thermoelectric voltage V between the terminal wires of the LTCC sensor should be canceled out.

This leads to the conclusion that the TIEMF effect within the LTCC sensors can be mainly ascribed to some level of non-uniformity of the chemical composition of the vias paste, which could cause the thermo-power μ_v to be non uniform. This heterogeneity seems to be confirmed by the analysis of the vias (**Figure 99**) which shows a different diffusion of Si and Al elements within the Au material of the vias.

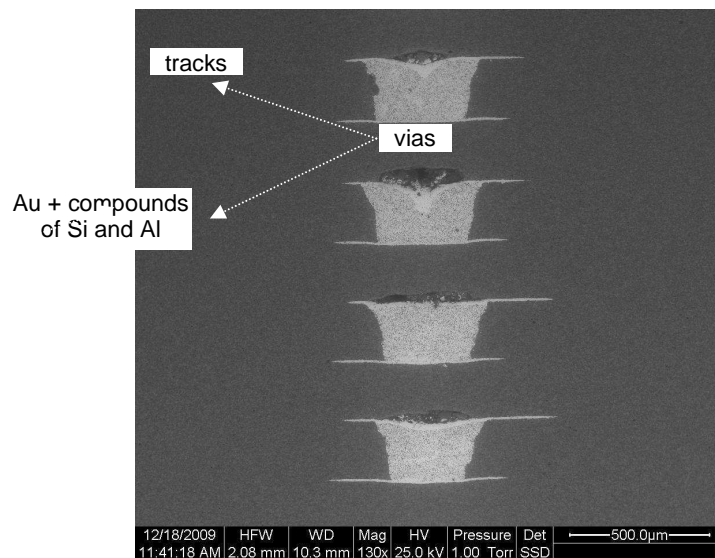


Figure 99: Cross-section of 4 vias of the 40-layer LTCC sensor

This hypothesis is supported by the fact that the TIEMF voltage measured under similar conditions on the first series of LTCC sensors made of Ag conductive lines and vias is much smaller ($<1\mu\text{V}$ with a temperature drop of 60 K)

4 Development of pick-up coils built with POZh cable

In order to obtain a pick-up coil sensor with an increased ground insulation and a reduced thermal gradient with respect to the sensor built using ceramic coated wires or MIC insulated wires, coils made using POZh wires have also been built.

"P.O.Zh. conductor" are Nickel-plated Copper conductors with braided fiberglass insulation, produced by a Russian manufacturer (VNIKIP).

There have been serious difficulties in the procurement of the conductor, which arrived only in July 2008 after one year and many contacts with Vniikp, Expocable, Best-Electro, Rubincon Power and Russian ITER Domestic Agency. The description of the electric tests carried out on the first sample of POZh cable can be found in [9].

The available POZh cable has been provided in three different batches. The pick-up coil was built using the wire coming from the first batch (batch N25) but only afterwards differences were found among characteristics of the three batches. In particular, the cable used presented the worst characteristics in terms of electric insulation. Following visual inspections evidenced the different uniformity and integrity of the insulation of the three cables.

The sensor is formed by 8 layers and 628 turns (Figure 100).

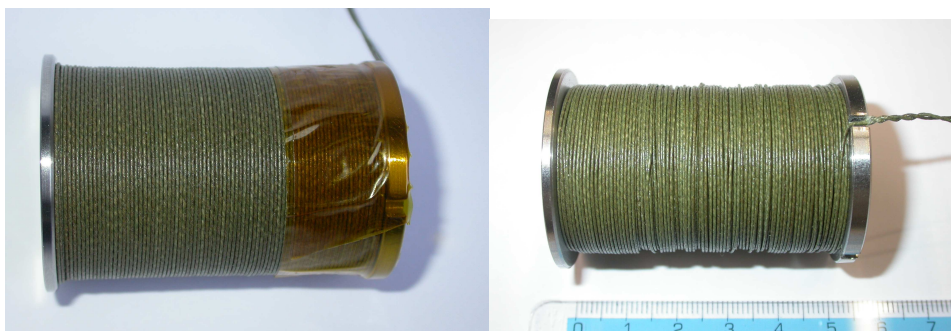


Figure 100: Pick up coil made with POZh wire

Table 28: POZh cable characteristics (according to manufacturer)

Conductor material	Cu 99.95%	Covered with a layer of nickel
	O < 0.02%	
	Others (Fe, Ni, Zn, As, Sn, Sb, Pb, Bi)	
Insulation material	Glass	No alkali
Conductor diameter	≈ 0.315 mm	Measured value
Outer diameter	≈ 0.630 mm	Measured value
Temperature range	-60°C to 600°C	

4.1 Insulation withstand voltage

The insulation withstand voltage of the POZh cable has been measured by wounding the cable on a metallic mandrel. A DC voltage has been applied between the cable and the metallic mandrel itself. The measurements have been carried out by means of two different instruments, the SATURN-ISO LEM in the range 100-1000V and the ABB METRISO 5000 in the range 2500- 5000V.

Electric insulation tests carried out on cables coming from different batches have shown some differences. Tests results are reported in Table 29. The values of resistance were measured before and after the discharge for each batch. Tests carried out after the discharge show a partial capability of regeneration.

Voltage [V]	R [GΩ] (batch N25)	R [GΩ] after discharge (batch N25)	R [GΩ] (batch N26)	R [GΩ] after discharge (batch N26)	R [GΩ] (batch N212)	R [GΩ] after discharge (batch N212)
100	200	1000	200	500	300	1000
200						
250	200	1000	200	500	300	1000
500	600	0.11 (after temporary discharge)	300	100 (with slow increase)	600	1000 (with slow increase)
600	600	DISCHARGE			600	DISCHARGE
700	700 (after temporary discharge)				1000	
750	DISCHARGE		300	50	1000	
800						
850					1000	
1000			300	DISCHARGE	DISCHARGE	
2500			DISCHARGE			

Table 29: Insulation resistance values for the three different batches

The insulation withstand voltage of the pick-up coil sensor (8 layers and 628 turns), built with the cable coming from the first batch (N25), was measured by applying a voltage between the conductor and the metallic reel on which the POZh cable is wound: the breakdown voltage was found bigger than 500 V. Due to slits on the reel necessary for the impregnation of the fluid ceramic, the metallic reel present sharp edges which reduced the withstand voltage.

4.2 Electric characterization

The sensor dynamic behavior is equivalent to that of a circuit constituted by the series of an inductance and a resistance in parallel with a capacitance (Figure 29). The above mentioned parameters have been measured by the HP4194 impedance analyzer and are shown in *Table 30*.

Table 30: electric parameters of the LTCC sensor equivalent circuit

Req	Leq	Ceq	Resonance frequency
[Ω]	[μH]	[pF]	[Hz]
12.34	3360	71.56	0.32E+06

Figure 101 shows the bode diagram of the impedance Z_{eq} of the equivalent circuit (calculated according to the values of indicated in **Table 30**).

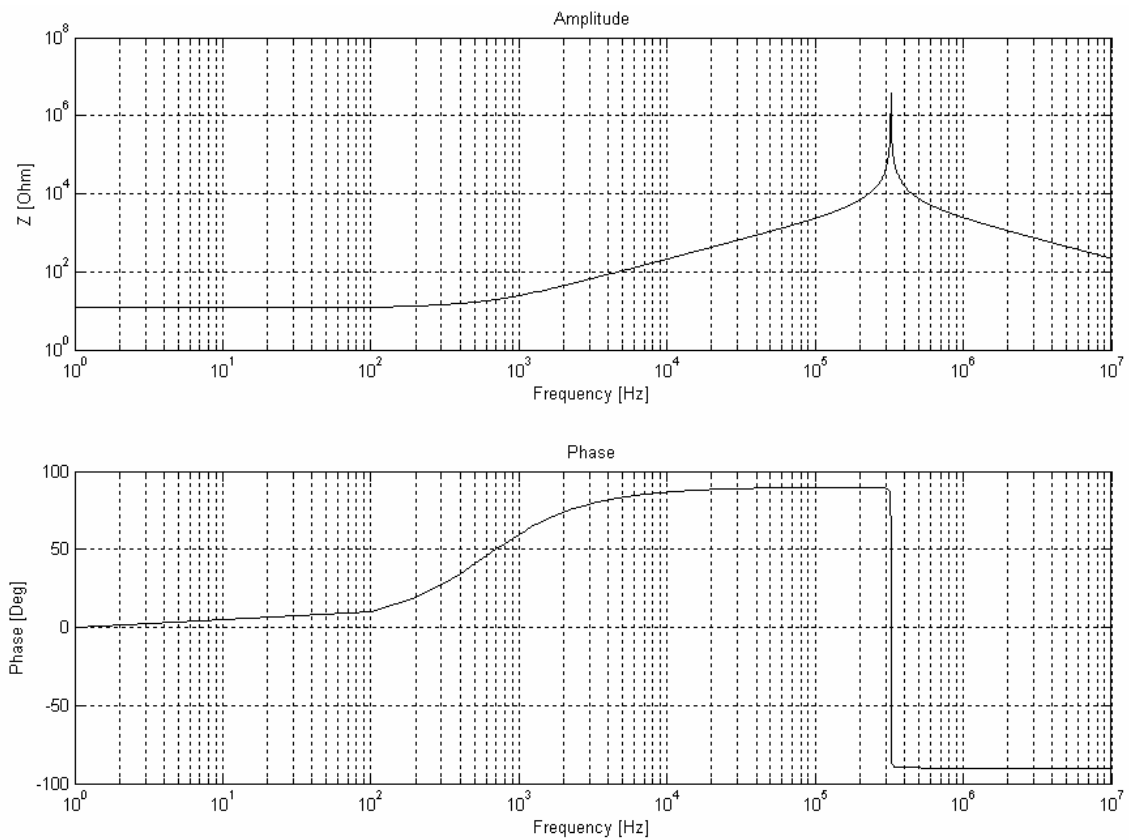


Figure 101: Amplitude and phase of the equivalent impedance of the POZh pick-up coil

The bandwidth of the measuring probe consisting of POZh sensor and acquisition system has been calculated referring to the equivalent circuit shown in **Figure 31** (see 3.1.2.2).

Figure 102 shows the amplitude of the transfer function of the measuring probe (POZh sensor + input resistance of the acquisition system) while **Table 31** display the cut off frequency.

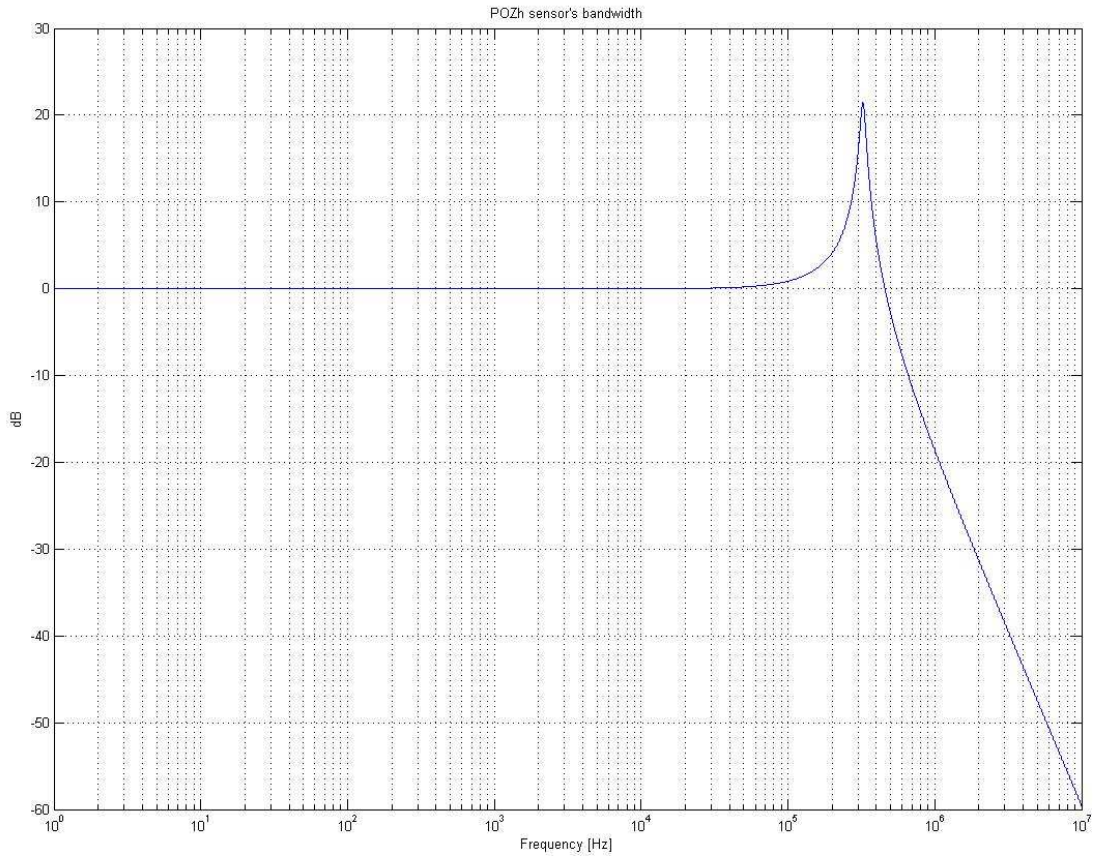


Figure 102: Amplitude of the frequency response of the LTCC magnetic probe

Table 31: cut off frequency of the measuring probe (POZh sensor and input impedance of the acquisition system)

Cut off frequency [MHz]	0.50E+6
-------------------------	---------

The cut-off frequency is smaller than that of the LTCC sensors, but still larger than required

4.3 Micrographic analysis

Figure 103 shows a SEM image of a POAh cable while **Figure 104** and **Figure 105** show the composition of the conductor core and of the conductor surface.

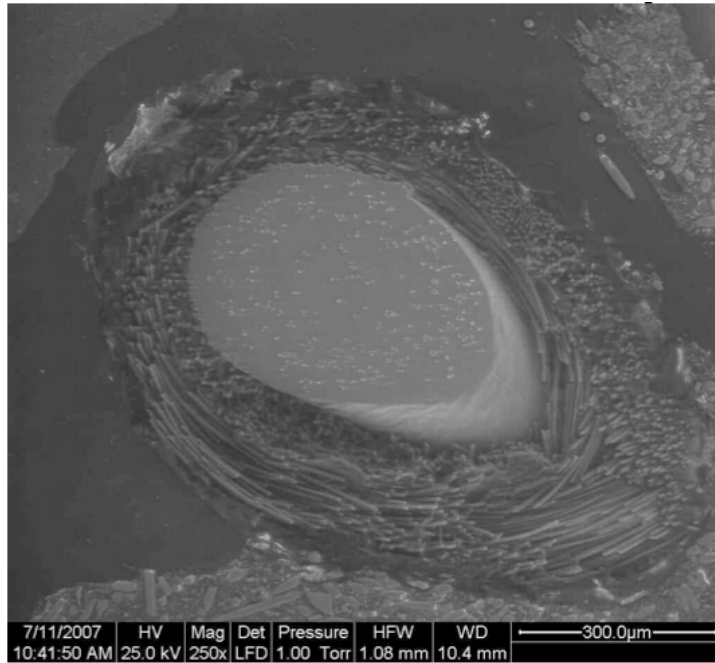


Figure 103: SEM image of POHz cable

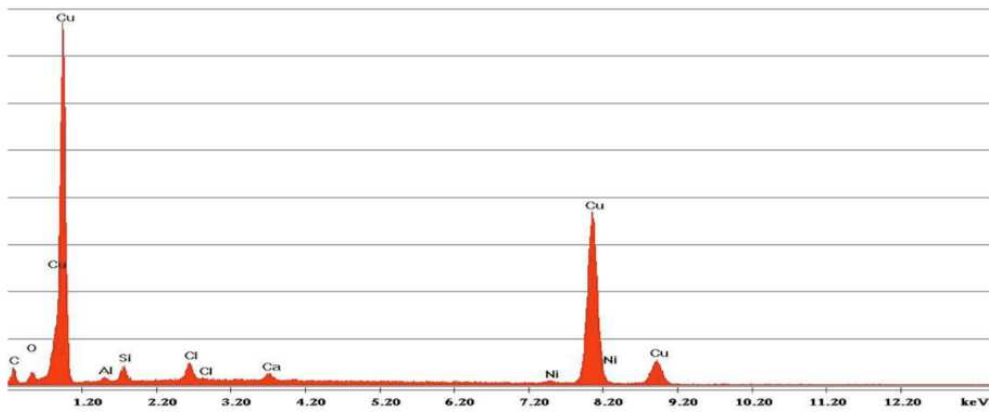


Figure 104: composition of the POZh conductor core

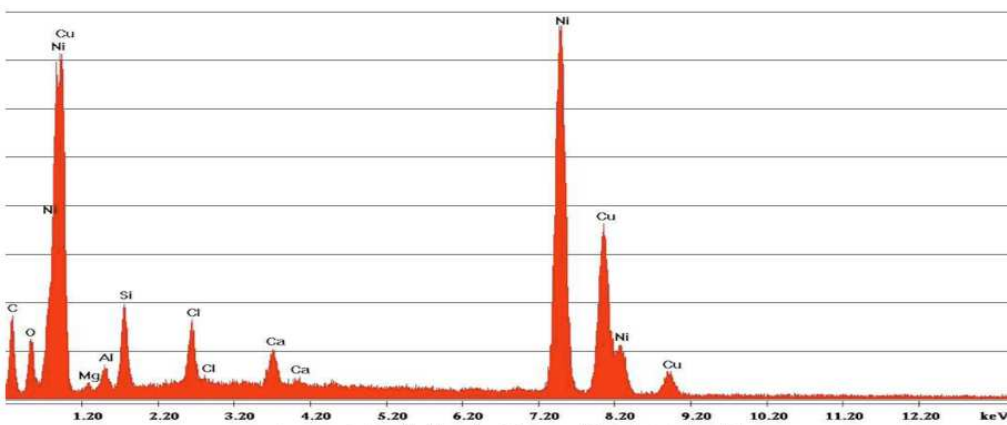


Figure 105: composition of POZh conductor surface

4.4 Magnetic characterization

The equivalent magnetic areas of the LTCC sensors, main and transverse, have been calculated in order to evaluate the sensitivity to magnetic fields along the main and transverse direction of the sensor. The procedure for the magnetic calibration is the same already used for Ag LTCC sensors (3.1.3). The LTCC sensors were fixed on a calibrated support in order to obtain a good alignment with respect to the direction of the imposed magnetic field B (*Figure 106*).

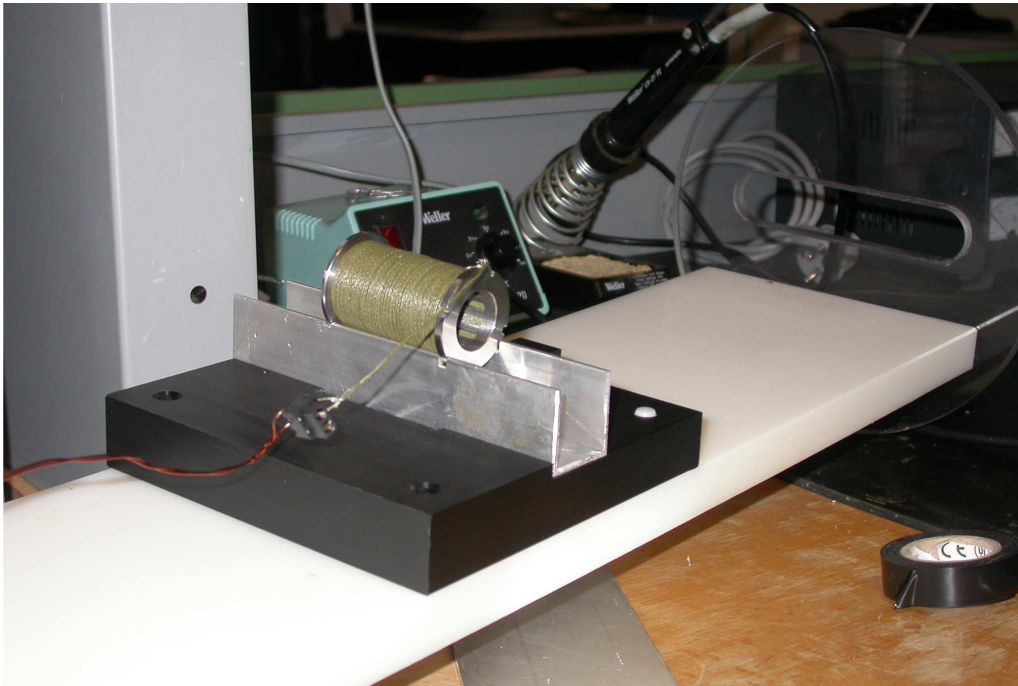


Figure 106 : POZh sensor on the calibrated support.

The results are shown in *Figure 107* (main area) and *Figure 108* (transverse area, both sides).

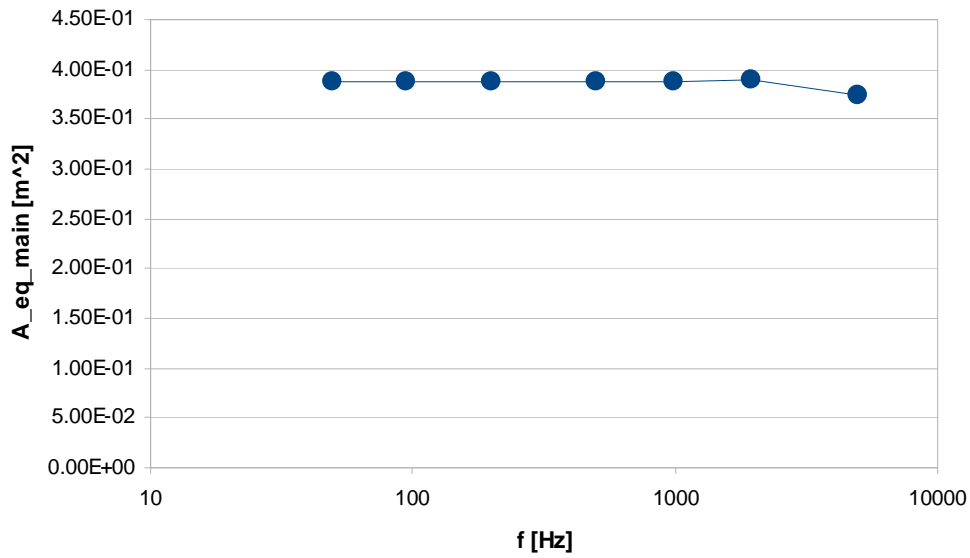


Figure 107 : Main equivalent area $A_{eq,long}$ of the POZh sensor.

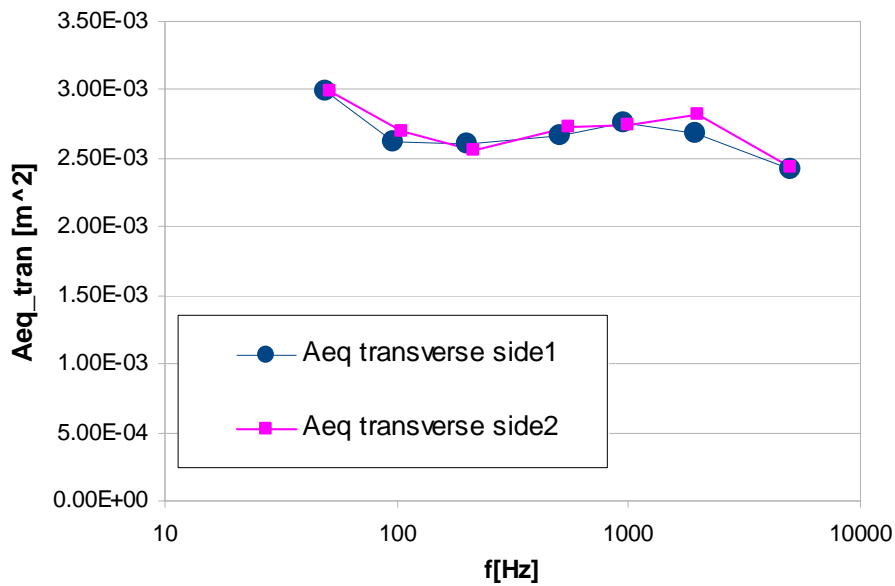


Figure 108 : Transverse equivalent area $A_{eq,tran}$ (side 1 and side 2) of the POZh sensor.

Table 32 lists the values of the main and transverse equivalent area at 100Hz for the POZh sensor and the maximum $A_{transverse}/A_{main}$ ratio. The magnetic equivalent area of the sensor is fully satisfactory, since along the main direction it is consistent with the geometrical characteristics of the winding and along the transverse direction is <1%.

Table 32: average values of main and transverse area and maximum $A_{\text{transverse}}/A_{\text{main}}$ ratio

Sensor	Main Area [m ²]	Transverse first side area [m ²]	Transverse second side area [m ²]	Maximum $A_{\text{transverse}}/A_{\text{main}}$
POZh	3.87E-01	2.61E-03	2.70E-03	0.7%

4.5 Vacuum out-gassing in ITER relevant conditions

The procedure of the experiment and the mathematical model adopted are the same already used in the case of Ag LTCC sensors and can be found in 3.1.4. The experiment set-up is shown in *Figure 48* and *Figure 49* while the baking cycle is shown in *Figure 51* and *Figure 52*.

Table 26 reports the results of the experiment at the end of the baking cycle; the out-gassing rate of the LTCC sensor is corrected from the empty chamber OR value.

	Empty chamber * 10 ⁻⁹ [Pa m ³ /s]	POZh sensor * 10 ⁻⁹ [Pa m ³ /s]
120 °C	7.3	12 – 7.3 = 4.7
30 °C	0.7	2.2 – 0.7 = 1.5

Table 33: Absolute OR of POZh sensor and empty chamber

Figure 53 shows the measured pressures and the calculated OR for the empty chamber while *Figure 109* shows pressures and OR for the POZh sensor.

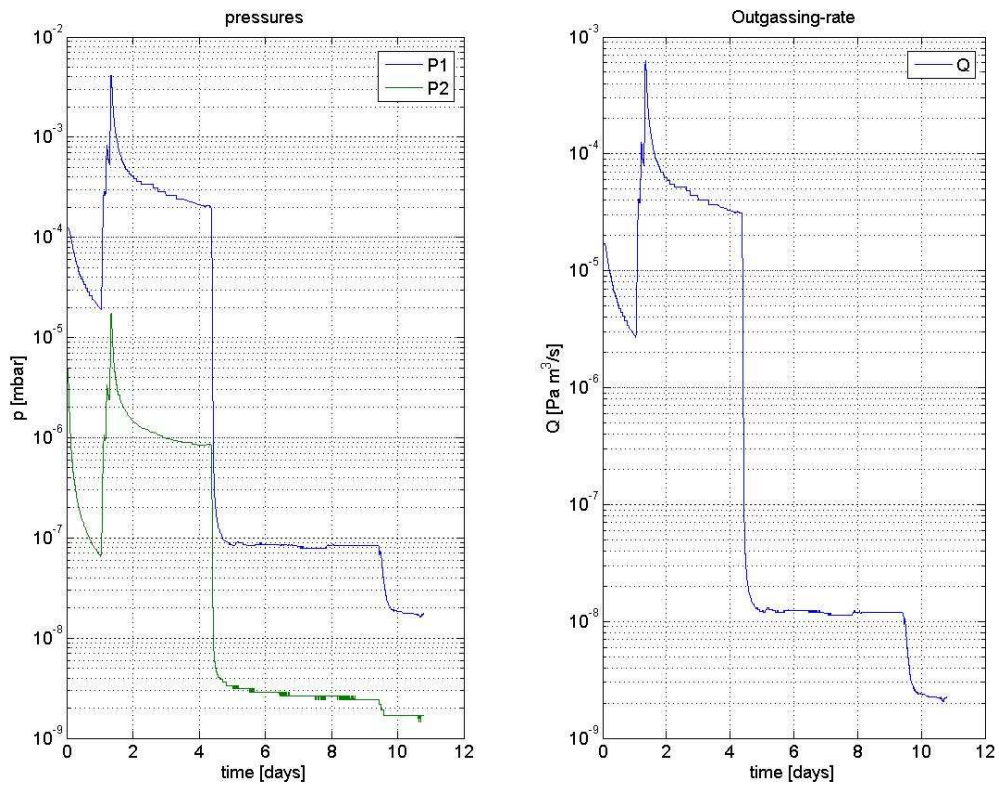


Figure 109: Measured pressures (left) and OR evaluated (right), PoZh sensor

As in the case of LTCC sensors pure H_2 has been considered as out-gassed substance and this choice determines an overestimation of the out-gassing rate.

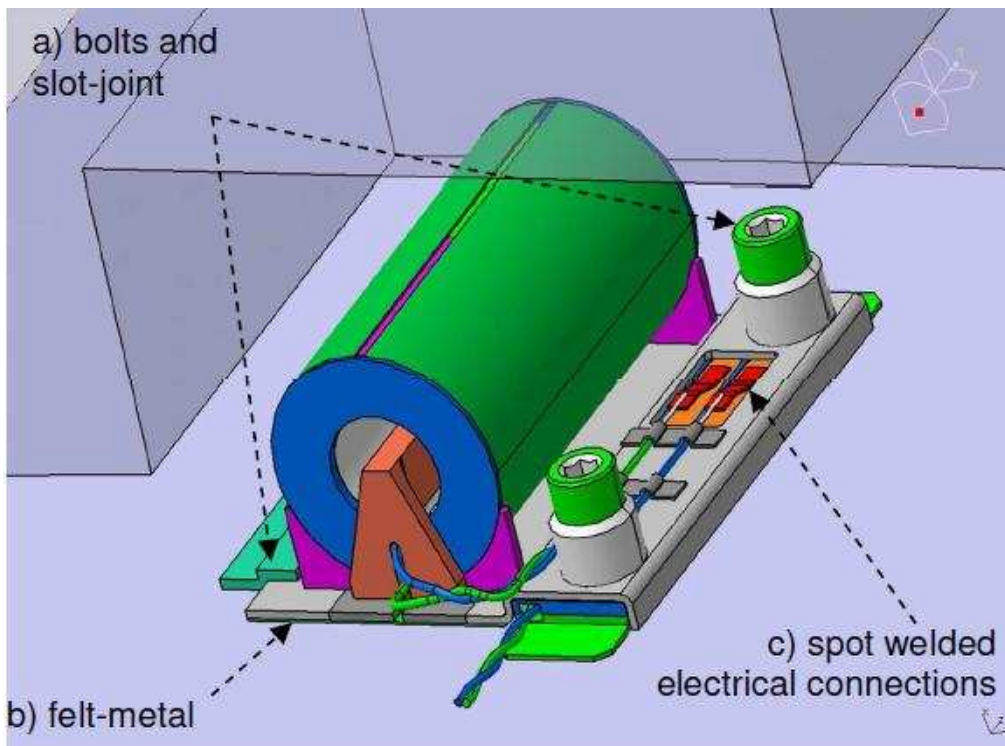


Figure 112: Model of the reference design of in-vessel equilibrium pick-up coil and fixing system

In the development of the new magnetic coil connection system the following improvements has been considered:

- Manufacture of all fixing parts on a single platform welded to the vessel
- Improved the Remote Handling suitability
- Replacement of the slot-joint with two captivated bolts for mechanical fastening
- Demonstration of the feasibility on the base of JET experience (robotic solution could be developed later)

Figure 113 shows the model of a proposed design of magnetic coil connector. The new design is mainly aimed at simplifying the interface with the vacuum vessel and at keeping the thermal gradient inside the sensor, and between the sensor and the in-vessel wiring, within limits acceptable for the sensor operation.

The assembly is composed of two main components:

- a Fixed Platform, permanently welded to Vacuum Vessel and containing the terminals of in-vessel wirings
- a Removable Support plate, supporting the coil and its terminals.

The Overall dimensions of the whole assembly are 100mm × 100mm × 42mm, fully compatible with existing design. This concept is based on a tangential pick-up coil made with the LTCC technology. Nevertheless this proposal could be adapted with minor modifications to different coil types (normal coils, bobbins made of ceramic or glass insulated wire).

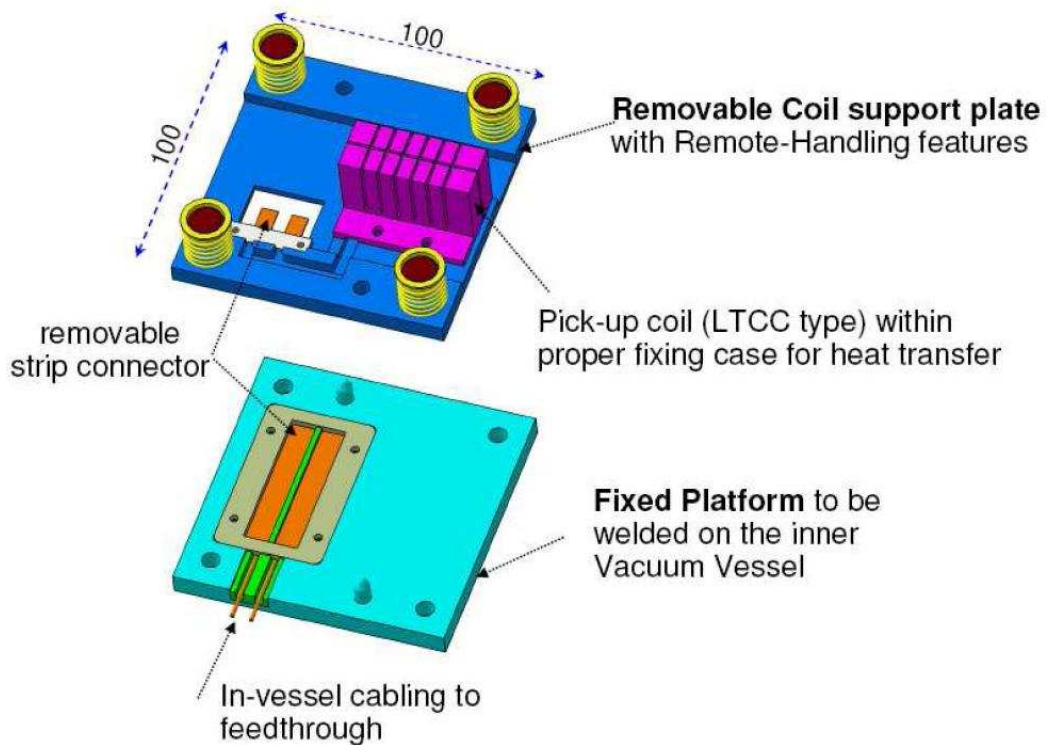


Figure 113: Model of the new proposal for in-vessel pick-up coils connector

The main characteristics of the proposed coil connection system, with comments and open issues to be refined for the detailed design, are described in the following sub-sections.

5.1 Description of the Platform

Figure 114 describes the concept of the platform, which is intended to be permanently welded to the Vacuum Vessel by means of standard welding process. The platform contains a pocket to house the terminals of the in-vessel wires (enclosed in a proper ceramic structure screwed to the platform) and all the features for engagement of the support plate by means of RH (conical dowels) and its fixing through 4 bolts.

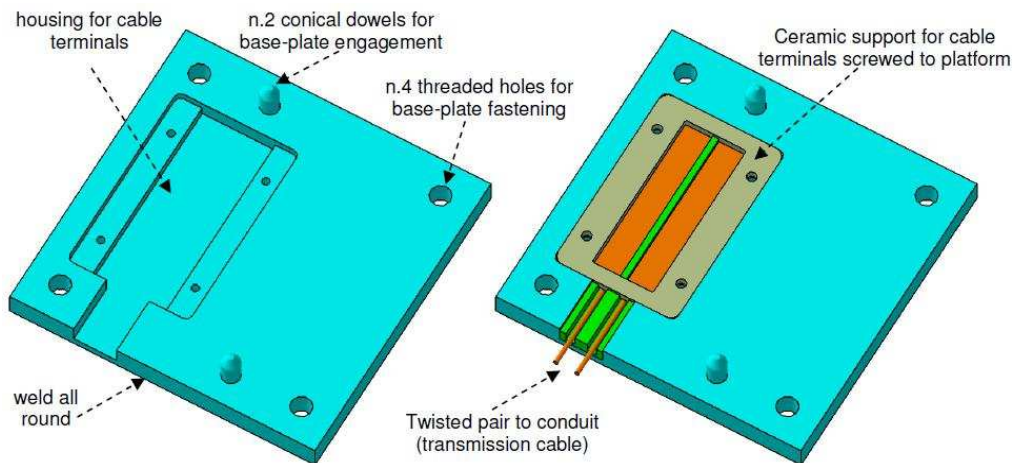


Figure 114: Platform permanently welded to Vacuum Vessel

The interface between the platform and the surface of the Vacuum Vessel is drafted in **Figure 115**. Considering the typical poloidal and toroidal extension of the sensor (100mm × 100mm) and the minimum curvature radius of the vessel (1570mm) the resulting maximum gap between sensor and vessel surface is of the order of 0.8mm. Therefore a proper surface machining must be foreseen, to guarantee a good contact necessary for heat transfer from sensors to vessel. Two solutions could be adopted:

- a) flattening of the vessel surface on each sensor location;
- b) machining the sensor support to meet the curvature of the vessel.

The solution with minor impact for the two procurements has to be evaluated: the first solution would require the machining of several hundreds pads during vessel manufacture; the second would require the manufacture of several different platforms to meet the different curvatures of the vessel surface.

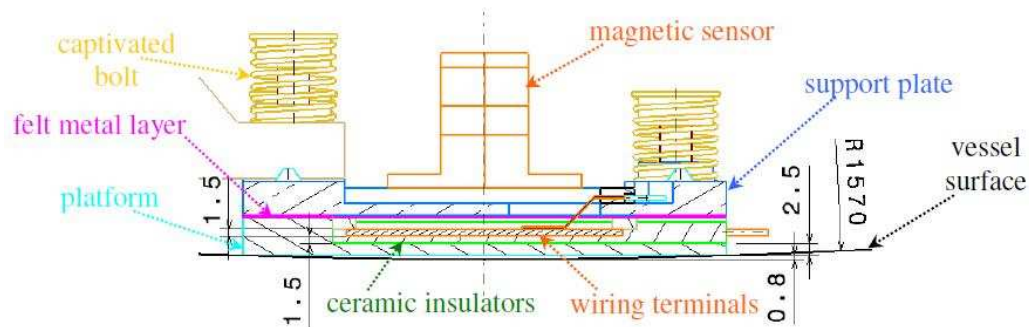


Figure 115: details of platform/vessel interface and platform terminals

The main characteristics of the Platform are summarized in **Table 34**.

Table 34: main characteristics of Fixed Platform

Characteristics	
Material:	AISI 316L
Thickness:	8 mm
Thermal interface between platform and vessel:	contact through weld fillets

5.2 Description of the Support Plate

Figure 116, Figure 117 and Figure 118 describe the concept of the coil support plate, which contains housing for the coil and for the conductor leads and all the features for installation by means of Remote Handling system.

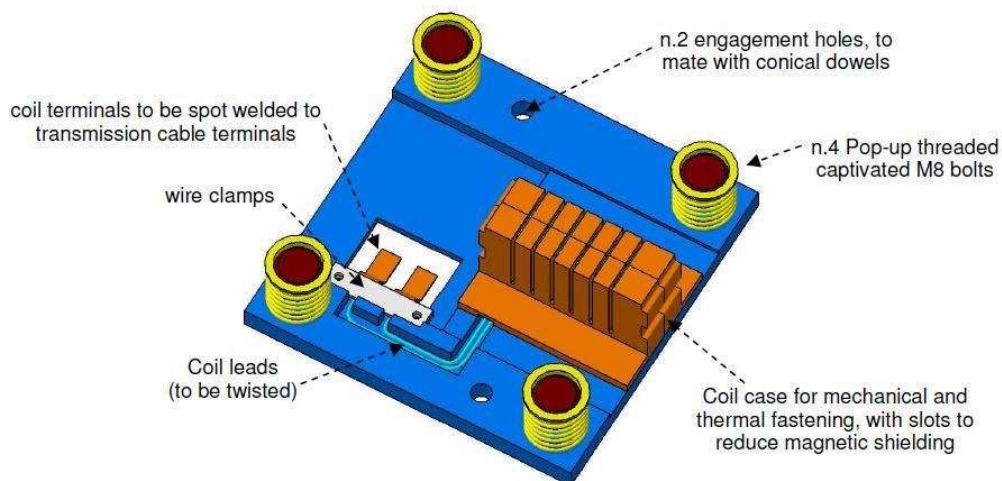


Figure 116: Coil support plate

The coil is enclosed within a copper case necessary to maximize the thermal heat transfer from coil to vessel. The case is inserted in a close fitting groove, which guarantees the correct positioning, and can be fixed by welding or bolting (to be defined).

The features for RH installation are 2 engagement holes that must mate with the conical dowels on the platform, 4 captivated bolts and an auxiliary handle to grip the whole assembly (*Figure 118*). All the RH handling features have been adapted from similar tools already designed for JET [12].

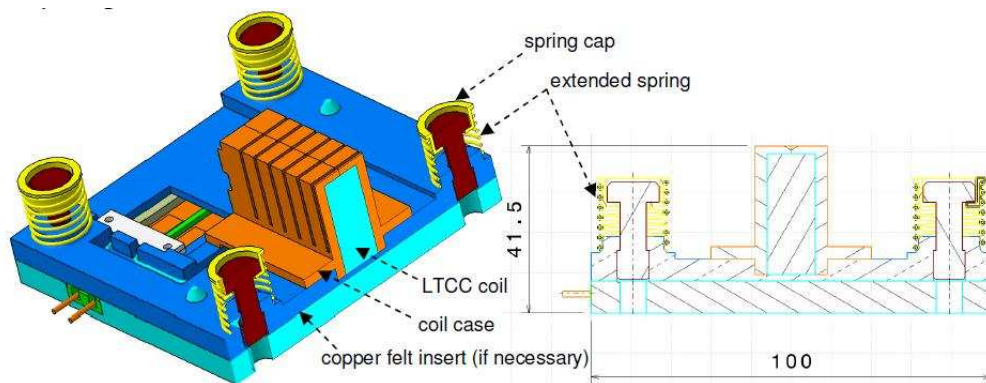


Figure 117: Cross section of pop-up threaded captivated M8 bolts and LTCC coil

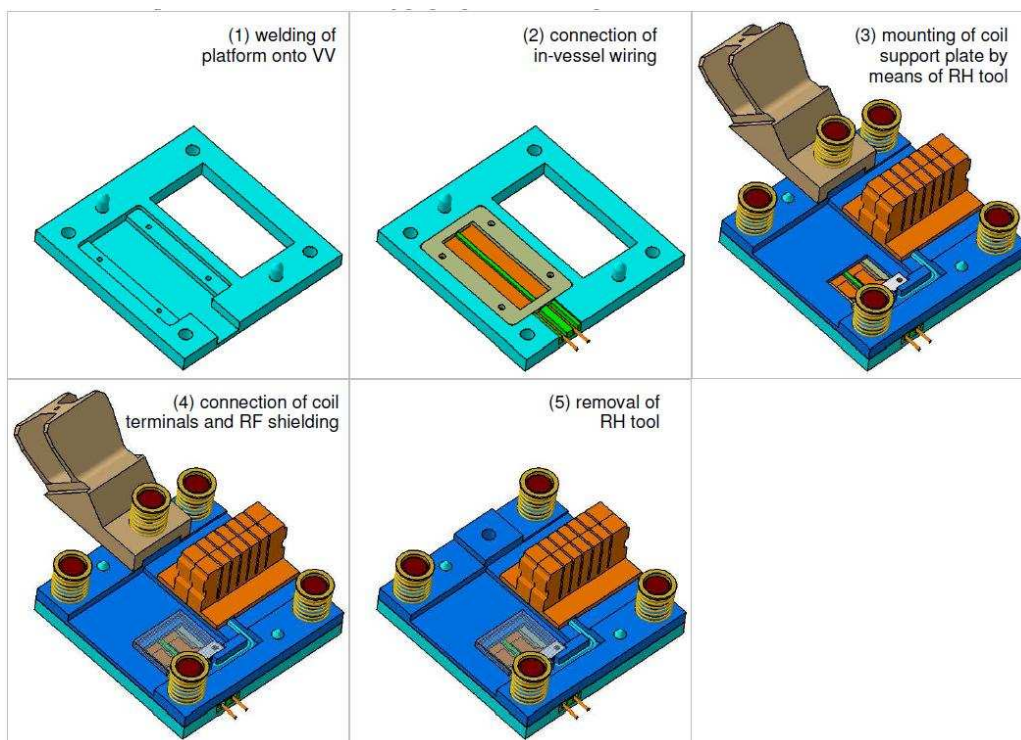


Figure 118: RH installation sequence

The main characteristics of the coil Support Plate are summarized in Table 4.

Characteristics	
material:	Copper
Thermal interface between base-plate and platform:	face to face contact with possible insert of felt metal
Electrical connection of sensor terminals to in-vessel wiring	Spot welded

5.3 Thermal Analyses

This Section describes the results of thermal analyses carried out in order to assess the overall thermal transfer capability of the coil connection system, needed to keep the temperature drop within the LTCC coil below the acceptable limits, relying only on thermal conduction towards the vacuum and without the need of active cooling.

Previous studies on the original design concept of pick-up coils made of Mineral Insulated Cable indicated that, in order to keep a measurement error induced by thermo thermoelectric phenomena like RITES and TIEMF of the order of 1%, the temperature variation within the coil must be kept below 10°C [13] [14]. This target was considered the reference design specification for the typical assembly including sensor and connector.

Steady-State Thermal Analyses have been performed on the proposal connector. The results of the analyses obtained by means of ANSYS are described in the following sub-sections.

5.3.1 Thermal analyses of new design concept

5.3.1.1 Description of the model, material characteristics, loads applied and assumptions

A 3D model has been adopted (*Figure 119*), representing the support necessary to guarantee a proper thermal path from the sensor to the vessel. The model is made using

the 3-D CAD software CATIA V5 and then imported in ANSYS with some simplification to obtain a model of about 190.000 elements and 40.000 nodes.

In order to study the better solution to reduce the thermal gradient and the maximum temperature in the magnetic pick-up coils, three variants of the same model have been analysed. Differences are only due to different possible configurations of the platform (*Figure 120* to *Figure 122*), the lower plate that has to be welded to the vessel:

- a) basic solution, considering thermal conduction only through fillet weld (*Figure 120*);
- b) with pocket, to reduce material and increase thermal path (*Figure 121*);
- c) with copper insert, to make thermal distribution more uniform (*Figure 122*);

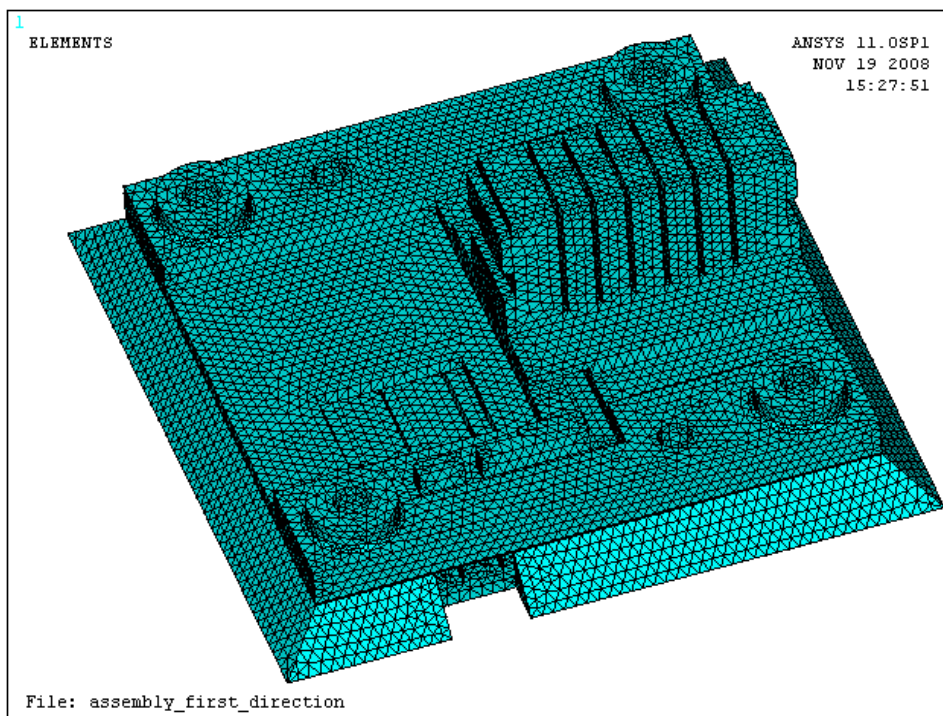


Figure 119: mesh

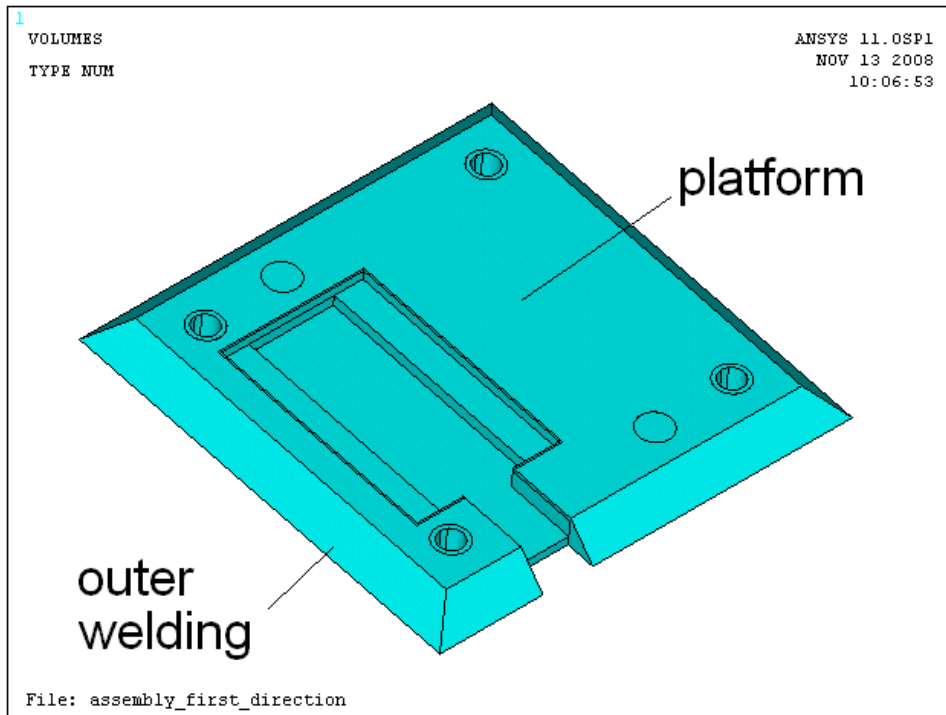


Figure 120: platform basic solution with outer welding (configuration a)

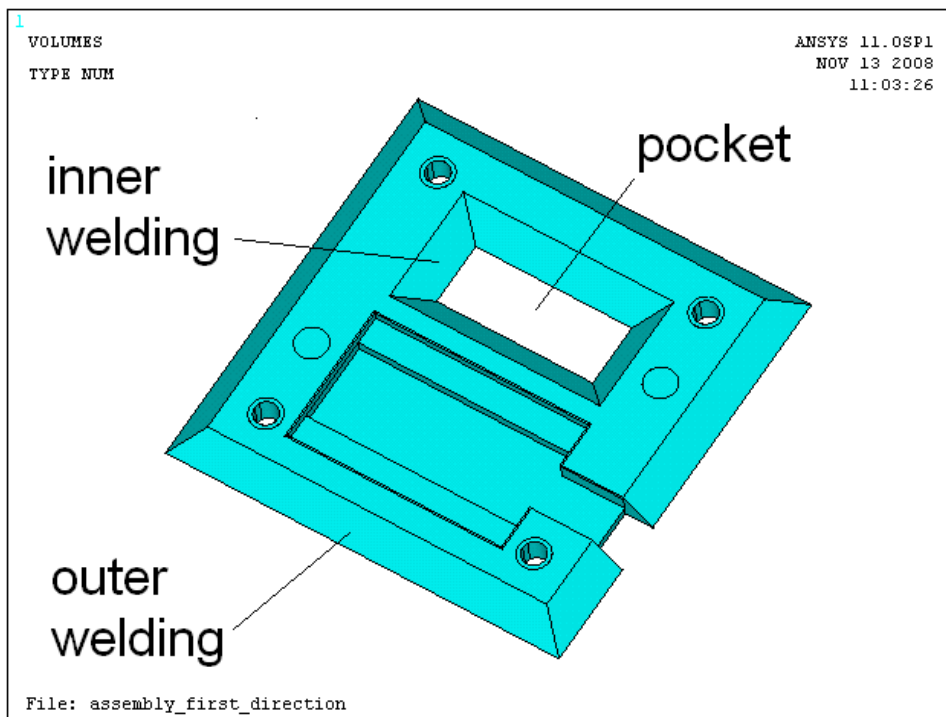


Figure 121: Platform with pocket, outer plus inner welding (configuration b)

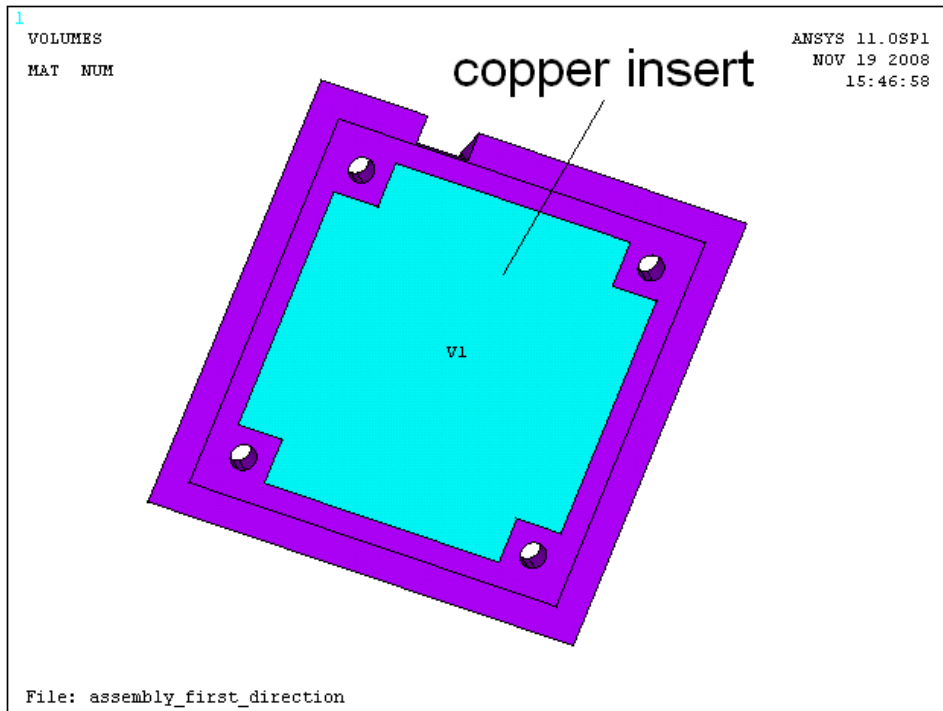


Figure 122: Platform with copper insert (bottom side). Outer welding (configuration c)

The main characteristics of the model are the following:

Model geometry:

- Dimensions as indicated in the figures of Section 3 (overall 100mm × 100mm × 42mm);

Elements:

- 3D Thermal Solid (SOLID70); 8 nodes brick; d.o.f. TEMP;

Materials (see Table 6 for properties):

- copper;
- stainless steel;
- LTCC sensor equivalent material (Heraeus CT700 ceramic + silver conductors);
- Macor;
- graphite foil (the material SIGRAFLEX, registered trademark of SGL CARBON AG, was considered as an example);

Analysis type:

- Steady-State Thermal Analysis;

Loads and boundary conditions:

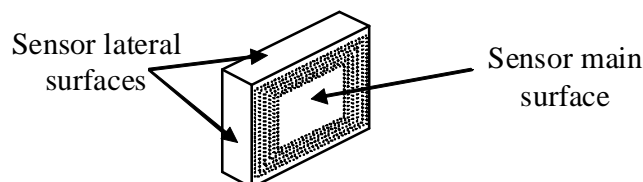
- Heat generation rate induced by radiation (**Table 35**);
- Constant temperature boundary at contact surface between platform and vessel;

Table 35: characteristics of materials used in the simulations

Material	Thermal conductivity [W / mK]	Heat generation rate induced by radiation [W / m ³]	Comments
Macor	1.5	0.22	electric insulation
LTCC sensor equivalent material	1.1	(considered equal to ceramic)	sensor
Stainless Steel	15	0.67	structures + welding
Copper	385	0.77	structures
graphite foil	100 10 _⊥	(considered equal to copper)	in plane through plane

Assumptions:

- Radiation and convection neglected;
- To assure a good thermal contact between the platform and the coil support plate a graphite foil (0.35mm thick) has been considered as interposed between the two surfaces. The “in-plane” and “through-plane” thermal conductivity of the foil, function of temperature, were extracted from the manufacturer data sheet (Figure 123) considering a typical operating value of vessel temperature <200°C;
- The LTCC sensor is fixed inside the copper case (**Figure 116**). As a conservative condition, only the main surfaces (both sides) of the sensor are considered in contact with the copper case whereas the lateral surfaces are considered adiabatic.



- As a further conservative condition, the bottom surface of the platform (the surface that matches the vessel) has been assumed adiabatic: the heat can flow only through the fillet weld.

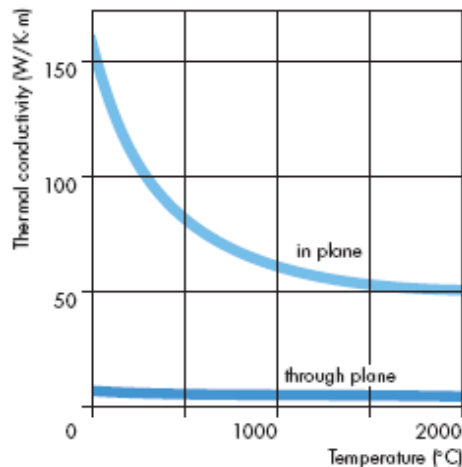


Figure 123: Thermal conductivity of SIGRAFLEX as a function of temperature [24]

5.3.1.2 Results of the simulations

In order to study the better solution to reduce the thermal increment within the support, five simulations have been carried out modifying the shape of the platform and the value of some parameters. A summary of the different solutions studied and of the results obtained is reported in **Table 36**.

The temperature distribution for the five simulations is reported in **Figure 124** to **Figure 128**.

The temperature drop within LTCC sensor plus terminals remains almost the same for each simulation except for the last one where the thermal conductivity of the copper felt has been reduced from 10W/mK to 1W/mK. The presence of the copper insert does not reduce in an appreciable way this temperature variation.

The surfaces of the welding that match the vessel (boundary conditions) have been set to 0°C except for the fourth simulation where a gradient of 8°C has been considered to take into account the actual temperature gradient foreseen in operating conditions [15].

Table 36: results of the simulations

Simulation	Pocket	Copper insert	Boundary conditions (welding)	Copper felt through-plane conductivity [W/mK]	ΔT LTCC/terminals [°C]	Tmax [°C]
1	(b) With pocket/inner +outer welding	No	0 °C	10	6.5	19.4
2	(a) Without pocket/only outer welding	No	0 °C	10	6.4	30.2
3	(c) Without	yes	0 °C	10	6.2	27.7

	pocket/only outer welding					
4	(c) Without pocket/only outer welding	yes	0-8°C gradient	10	6.8	31.9
5	(c) Without pocket/only outer welding	yes	0 °C	1	8.3	32.0

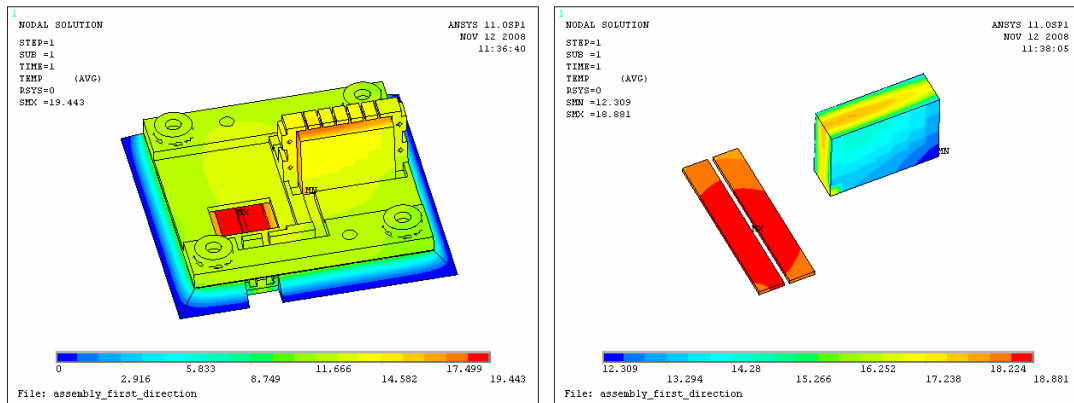


Figure 124: distribution of the temperature for the simulation n.1 (left: whole model; right: detail of LTCC sensor and terminals)

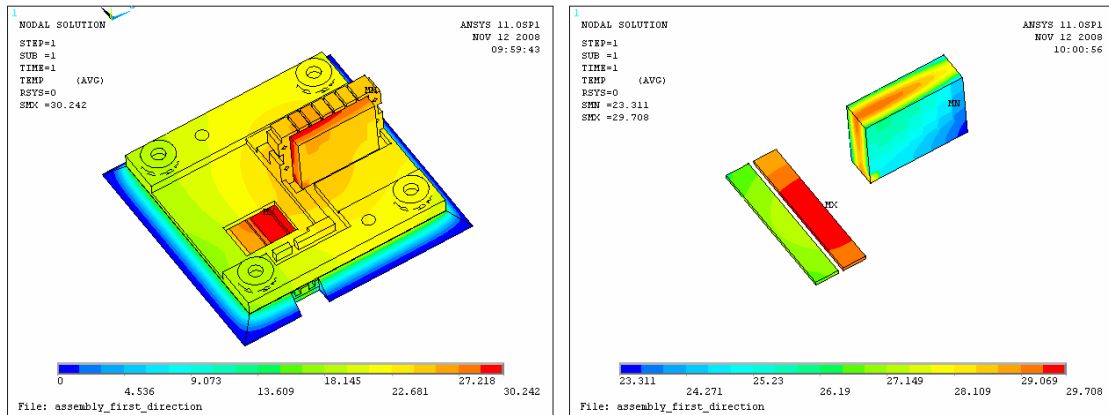


Figure 125: distribution of the temperature for the simulation n.2 (left: whole model; right: detail of LTCC sensor and terminals)

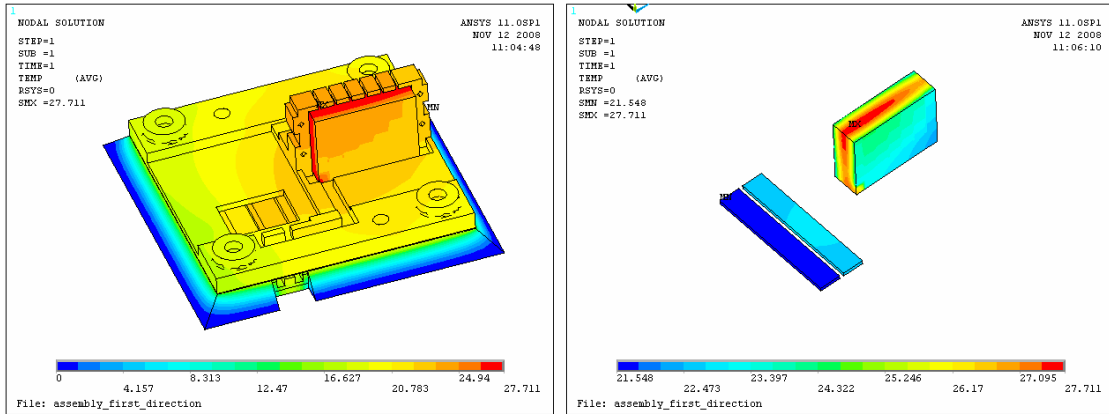


Figure 126: distribution of the temperature for the simulation n.3 (left: whole model; right: detail of LTCC sensor and terminals)

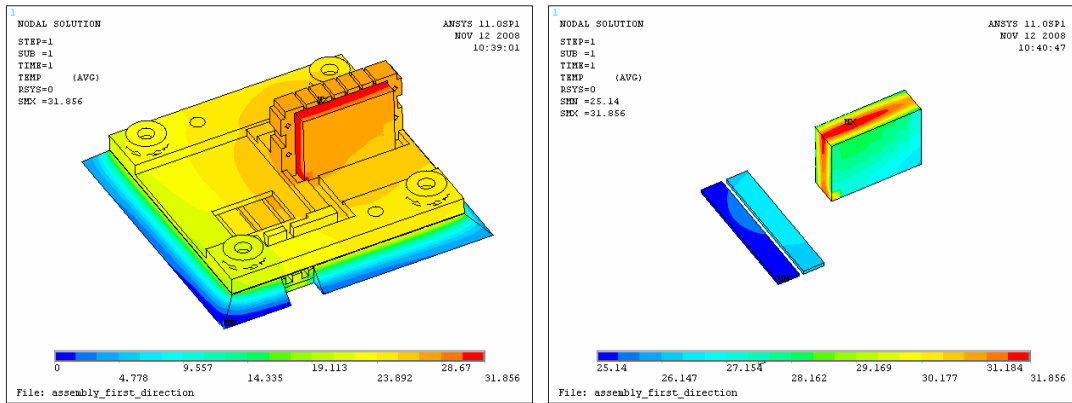


Figure 127: distribution of the temperature for the simulation n.4 (left: whole model; right: detail of LTCC sensor and terminals)

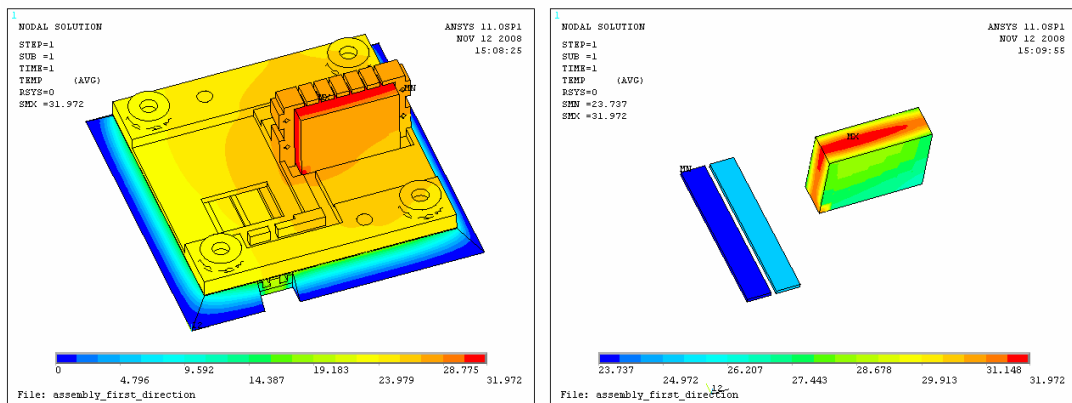


Figure 128: distribution of the temperature for the simulation n.5 (left: whole model; right: detail of LTCC sensor and terminals)

6 Conclusions

In magnetically confined nuclear fusion research the magnetic diagnostics are of great importance, providing key information on the state of the plasma and allowing an active control on the position and shape of the plasma itself.

In this work we presented the development and productions of a new type of pick-up coil magnetic sensors made with LTCC technology that should better comply with ITER requirements.

Different sets of LTCC sensors have been built since 2007 in order to test different materials for both the conductive lines and the ceramic substrate. LTCC pick-up coils have an outstanding dimensional and mechanical stability, a good thermal conductivity and a fine line pattern. These sensors should also guarantee increased radiation hardness and Signal/Noise ratio with respect to the standard pick-up coils made with Mineral Insulated Cables (MIC). They are compact, highly reliable and have an increased main/transverse magnetic area ratio.

Many tests have been carried out upon the LTCC sensors to analyze their composition and to characterize their electric, magnetic and thermal behaviors. Both Ag and Au LTCC sensors comply with ITER requirements, even if the Ag sensors present a small TIEMF effect and a small electric resistance which could reduce the spurious signals due to neutron radiation (RIEMF effect).

Sensors built with Nickel-plated Copper conductors with braided fiberglass insulation wound on a metallic reel have been developed and tested as an alternative to the standard pick-up coils built with MIC cables.

Finally, a platform suitable for the fixing of the magnetic sensors to the ITER vessel has been designed. The platform is necessary to guarantee the positioning of the sensors inside the ITER vacuum vessel in order to reduce the errors due to misalignments of the sensors themselves. Also, the new platform is suitable for remote handling operations, being composed by only two main assemblies, the first one permanently fixed to the ITER vacuum vessel and the second one designed to be easily set in place by a means of RH.

The tests carried out have shown that the new sensors can be used inside the ITER vacuum vessel. Nevertheless other tests will be carried out in the future such as

irradiation tests, necessary to evaluate the RIEMF effect. Also a fixing platform prototype has to be realized and tested.

7 References

- [1] <http://www.iter.org>
- [2] J. D. Lawson, "Some Criteria for a Useful Thermonuclear Reactor", A.E.R.E. report GP/R 1807, December 1955, declassified April 9th 1957
- [3] G. Chitarin, R. Delogu, A. Gallo, and S. Peruzzo, "Technology developments for ITER in-vessel equilibrium magnetic sensors", Fusion Engineering and Design 84 (2009) 593-598.
- [4] ITER Vacuum Handbook, v2.3 , 12/06/2009 (ITER Document 2EZ9UM)
- [5] G.Vayakis, "Baking cycle for outgassing tests used at JAERI for MIC", ITER IDM repository.
- [6] B.Ferrario, "Introduzione alla tecnologia del vuoto" Patron Editore-Bologna 1999.
- [7] N. Pomaro, "Operational procedure for calibration of magnetic sensors to be used in JET experiment", (RFX Ref.: SM-PR-001-CA, 28/02/2005)
- [8] N. Pomaro, P. Fiorentin, S. Peruzzo, L. Grando, "Messa a punto di una sorgente di riferimento di campo magnetico" (RFX Ref.: SM-NT-213, 15/06/2001)
- [9] G. Chitarin, C. Taccon, "Results of electrical tests on POZh conductors", (RFX Report: SM/NT/292 date: 22/06/07).
- [10] ITER Design Description Document - Diagnostics - 5.5.A Magnetics (N 55 DDD 1 01-06-12 W 0.3).
- [11] Appendix 1 to the Overview of the ITER Diagnostics System: ITER Magnetic Diagnostics Design Status, July 2004 (N 55 DDD 12 04-07-09 W 0.1).
- [12] "JET Facilities Remote Handling Requirements", Culham Division Specification, CD/S/J400, Issue: 2, Date: August 2006, and references therein.
- [13] G. Chitarin, L. Grando, S. Peruzzo, N. Pomaro, C. Taccon, "Design Study of the ITER magnetic diagnostic: in-Vessel tangential and normal coils, external flux loop, Halo current sensors and steady-state Sensors", EFDA Task TW4-TPDS-DIASUP "Diagnostic design for ITER", Deliverable EFDA 04-1210 D6.2, Final Report, 20/06/2006
- [14] G. Chitarin, E. Alessi, M. Cavinato, S. Dal Bello, R. Delogu, S. Peruzzo, C. Taccon, EFDA Task TW5- TPDS-DIASUP5 "Diagnostic design for ITER", Deliverable D2.2: EFDA Contract 05-1347 "Design study of the ITER magnetics diagnostic: in-

vessel pick-up coils, blanket halo sensors and divertor halo sensors, numerical model of halo currents”, Final Report 08/09/2008

[15] G. Vayakis, “Load conditions for in-vessel diagnostic components (2008)”, Presented at the ITER in-vessel diagnostic integration meeting, Cadarache, 7-8 February 2008 (ITER_D_29MWPX)

[16] Appendix 1 to the Overview of the ITER Diagnostics System: ITER Magnetic Diagnostic Design Status (N 55 DDD 12 04-07-09 W 0.1)

[17] G. Vayakis et al., “Magnetic diagnostics for ITER/BPX plasmas”, Rev. Sci. Instrum. Vol 74, No 4 (2003), 2409-2417

[18] <http://users.jet.efda.org/pages/mags/index.html>

[19] G. Chitarin, L. Grando, S. Peruzzo, N. Pomaro et al., “Design of new magnetic sensor for JET”, Review of Scientific Instruments, Vol 75, N. 10, October 2004, 4311-4313

[20] S. Peruzzo, W. Baker, V. Coccoresse, T. Edlington, S. Gerasimov, S. Huntley, N. Lam, A.Loving, C. Marren, N. Pomaro, V. Riccardo, and JETEFDA contributors, "Status of design and manufacture of the Upper Coils and Outer Poloidal Limiter Coils subsystems for the JET-EP magnetic diagnostic", Fusion Engineering and Design 74 (2005) 733-738

[21] Pomaro et al., ”New wide bandwidth in-Vessel magnetic measurement system for RFX”, Rev. Scien. Instruments, Vol. 74, N.3 (2003), 1554

[22] Y. Neyatani, et al., " Developement of magnetic sensors in JT-60 upgrade ", 14th Symp. on Fusion Eng., Vol.2 1183 (1991)

[23] http://www-jt60.naka.jaeri.go.jp/english/diag/html/diag_56.html

[24] Expanded Graphite - SLG Technologies GmbH, Data Sheet “Products Manufactured from Flexible Graphite Foil”, 2008, <http://www.sglgroup.com>

[25] G. Vayakis et al., “ Radia tion - induced thermoelectric sensitivity (RITES) in ITER prototype magnetic sensors ”, Rev. Sci. Instrum. Vol 75, No 10 (2005), 4324 - 4327.

[26] “Report on assessment and specification of in - Vessel MI - cable material for the ITER magnetic diagnostics”. R.Vila and E.R.Hodgson, final report, Contract 04 - 1207.

[27] P. Spuig, P. Defrasne, M. Moreau, Ph. Moreau, F. Saint - Laurent “Qualification of Tore Supra integrators for several thousand second long ITER pulses" TW2 - TPDS - DIADEV Final report (2003)

[28] 2001 - 082 Y. Kusama et al. " Support of the ITER diagnostics design: Impurity Influx Monitor (Divertor), Microfission Chambers, Thomson Scattering (edge) System, and Integrator for magnetic measurement" ITER_D_23DRB8, https://users.iter.org/users/idm?document_id=ITER_D_22JQLY

[29] P. J. Flanders, C. D. Graham, "DC and low frequencies magnet measuring techniques", Rep. Bog. Phys. 56 (1993) 431-492. Printed in the UK

[30] L.C.J.M. DE KOCK, Yu.K. KUZNETSOV, "MAGNETIC DIAGNOSTICS FOR FUSION PLASMAS" Report on the IAEA Technical Committee Meeting, held at Khar'kov, Ukraine 7-9 October 1994

[31] L. de Kock et all, "Design of the magnetic diagnostic for ITER", REVIEW OF SCIENTIFIC INSTRUMENTS, VOLUME 70, NUMBER 1, JANUARY 1999

SCUOLA DI DOTTORATO IN INGEGNERIA INDUSTRIALE

RIUNIONE COLLEGIO DI INDIRIZZO IN MECCATRONICA E SISTEMI INDUSTRIALI

Vicenza, 13 dicembre 2010, ore 10.00.

Collegio di indirizzo:

Battini Daria	P
Berto Filippo	P
Bolognani Silverio	G
Bonollo Franco	P
Boschetti Giovanni	P
Caracciolo Roberto	G
Chitarin Giuseppe	P
Faccio Maurizio	P
Ferrari Emilio	G
Ferro Paolo	P
Gamberi Mauro	P
Gasparella Andrea	G
Manzini Riccardo	G
Mattavelli Paolo	G
Oboe Roberto	P
Pareschi Arrigo	G
Persona Alessandro	P
Regattieri Alberto	G
Richiedei Dario	P
Rosati Giulio	P
Rossi Aldo	G
Timelli Giulio	P
Trevisani Alberto	P
Zambon Andrea	P
Zigliotto Mauro	G

Rappresentante dei Dottorandi:

Rossella Rosa P

Supervisore invitato:

Marino Quaresimin G

Ordine del giorno:

1. Comunicazioni
2. Autorizzazioni dottorandi
3. Commissione esame finale XXIII ciclo (ratifica)
4. Attività formativa strutturata di indirizzo: consuntivo anno 2010 e programmazione anno 2011
5. Valutazione dell'attività svolta dai dottorandi iscritti al XXV ciclo ed ammissione al II anno.
6. Valutazione dell'attività svolta dai dottorandi iscritti al XXIV ciclo ed ammissione al III anno.
7. Valutazione dell'attività svolta dai dottorandi iscritti al XXIII ciclo. Ammissione all'esame finale, approvazione dei medaglioni e formulazione del giudizio finale.
8. Approvazione del medaglione del dottorando iscritto al XXII ciclo ed in proroga di 12 mesi per la presentazione della tesi.

assistito alla presentazione dell'attività svolta da parte dell'Ing. Rossella Rosa e dopo aver terminato la discussione, formula il seguente giudizio sull'Ing. Rossella Rosa: ammessa al III anno con giudizio MOLTO BUONO.

7. Valutazione dell'attività svolta dei dottorandi iscritti al XXIII ciclo. Ammissione all'esame finale, approvazione dei medaglioni e formulazione del giudizio finale

Tutti i dottorandi del XXIII ciclo presentano l'attività da loro svolta.
Le presentazioni sono riportate nell'ALLEGATO 5.

Prima di avviare la discussione su ogni dottorando iscritto al XXIII ciclo, e dopo aver assistito alla presentazione della loro attività, il Coordinatore ricorda al Collegio i giudizi formulati dalla commissione che lo scorso 14 giugno 2010 ha condotto un accertamento sull'attività svolta da tali dottorandi. Tale commissione era composta dai Proff. F. Bonollo, R. Caracciolo, G. Chitarin, A. Persona e A. Trevisani.

FEDERICO CASAROTTO - XXIII CICLO

Titolo/argomento tesi di dottorato:

Critical analysis and economic optimization in the foundry after introduction of premium primary aluminum alloys for premium castings.

(Analisi ed ottimizzazione economico-gestionale in fonderia a seguito dell'impiego di leghe di alluminio innovative per la produzione di getti dagli elevati standard qualitativi)

Supervisore:

Prof. Franco Bonollo

Descrizione dell'attività:

vedi ALLEGATO 6

Dopo aver assistito alla presentazione dell'attività complessivamente svolta da parte dell'Ing. Federico Casarotto, preso atto del giudizio formulato dal supervisore e del giudizio formulato dalla commissione che ne ha accertato l'attività svolta in data 14-06-2010, dopo ampia discussione il Collegio di Indirizzo formula il seguente giudizio di ammissione all'esame finale: OTTIMO.

ANTONIO GALLO XXIII CICLO

Titolo/argomento tesi di dottorato:

Magnetic field sensors suitable for high temperature and vacuum operation and for remote handling in harsh environment

(Sensori di Campo Magnetico e di altre grandezze adatti al funzionamento in alta temperatura e vuoto e Sistemi di manipolazione remota per il loro posizionamento in ambienti ostili)

Supervisore:

Prof. Giuseppe Chitarin

Descrizione dell'attività:

vedi ALLEGATO 6

Dopo aver assistito alla presentazione dell'attività complessivamente svolta da parte dell'Ing. Antonio Gallo, preso atto del giudizio formulato dal supervisore e del giudizio formulato dalla commissione che ne ha accertato l'attività svolta in data 14-06-2010, dopo ampia discussione il Collegio di Indirizzo formula il seguente giudizio di ammissione all'esame finale: MOLTO BUONO.

CHIARA ORTOLANI XXIII CICLO

Titolo/argomento tesi di dottorato

Parametric Modeling of Logistics Networks: Operative and Environmental Costs

(Modellizzazione parametrica delle reti di trasporto: costi operativi ed ambientali)

Supervisore:

Prof. Alessandro Persona

Descrizione dell'attività:

vedi ALLEGATO 6

Dopo aver assistito alla presentazione dell'attività complessivamente svolta da parte dell'Ing. Chiara Ortolani, preso atto del giudizio formulato dal supervisore e del giudizio formulato dalla commissione che ne ha accertato l'attività svolta in data 14-06-2010, dopo ampia discussione il Collegio di Indirizzo formula il seguente giudizio di ammissione all'esame finale: MOLTO BUONO.

GABRIELE ZANARDO XXIII CICLO

Titolo/argomento tesi di dottorato:

Structural modification approaches to modal design optimisation of vibrating systems

(Ottimizzazione modale di sistemi vibranti tramite approcci di structural modification)

Supervisore:

Prof. Roberto Caracciolo

Descrizione dell'attività:

vedi ALLEGATO 6

Dopo aver assistito alla presentazione dell'attività complessivamente svolta da parte dell'Ing. Gabriele Zanardo, preso atto del giudizio formulato dal supervisore e del giudizio formulato dalla commissione che ne ha accertato l'attività svolta in data 14-06-2010, dopo ampia discussione il Collegio di Indirizzo formula il seguente giudizio di ammissione all'esame finale: OTTIMO.

DAMIANO ZANOTTO XXIII CICLO

Titolo/argomento tesi di dottorato:

Analysis and development of cable-driven robotic devices

(Studio e sviluppo di sistemi robotici a cavi)

Supervisore:

Prof. Giulio Rosati

Descrizione dell'attività:

vedi ALLEGATO 6

Dopo aver assistito alla presentazione dell'attività complessivamente svolta da parte dell'Ing. Damiano Zanotto, preso atto del giudizio formulato dal supervisore, dopo ampia discussione il Collegio di Indirizzo formula il seguente giudizio di ammissione all'esame finale: OTTIMO.

8. Approvazione del medaglione del dottorando iscritto al XXII ciclo ed in proroga di 12 mesi per la presentazione della tesi

Il Coordinatore ricorda al Collegio che lo scorso anno l'Ing. Pietro Vecchiato aveva fatto pervenire al Servizio Formazione alla Ricerca istanza di proroga di 12 mesi per la presentazione della tesi.

Il Coordinatore ricorda inoltre che durante la riunione telematica del 26-01-2010 il Collegio aveva espresso un giudizio sufficiente in merito all'attività complessivamente condotta dall'Ing. Pietro Vecchiato nel corso del triennio, ammettendolo pertanto all'esame finale. Il Collegio è pertanto oggi chiamato solamente ad approvare la relazione ("medaglione") preparata dal Supervisore del dottorando.

PIETRO VECCHIATO XXII CICLO

Titolo/argomento tesi di dottorato:

Lean Distribution

(Logistica distributiva snella)

Supervisore:

Prof. Emilio Ferrari

Descrizione dell'attività:

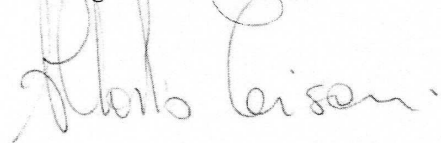
vedi ALLEGATO 6

Dopo aver assistito alla presentazione dell'attività svolta da parte dell'Ing. Pietro Vecchiato e dopo aver terminato la discussione il Collegio di Indirizzo approva la relazione preparata dal Supervisore e conferma il giudizio di ammissione all'esame finale: SUFFICIENTE.

Il presente verbale è redatto, letto ed approvato seduta stante.

La riunione termina alle ore 14.50

Prof. Ing. Alberto Trevisani



ALLEGATO 6

RELAZIONI E GIUDIZI DEI SUPERVISORI
SULL'ATTIVITÀ SVOLTA DAGLI ALLIEVI ISCRITTI AL XXIII CICLO
E SULL'ATTIVITÀ SVOLTA DALL'ALLIEVO ISCRITTO AL XXII CICLO
IN PROROGA DI 12 MESI PER LA PRESENTAZIONE DELLA TESI



RELAZIONE SULL'ATTIVITÀ SVOLTA DALL'ALLIEVO
ING. ANTONIO GALLO
NEL CORSO DEL TRIENNIO DI
**DOTTORATO DI RICERCA IN INGEGNERIA INDUSTRIALE, INDIRIZZO
MECCATRONICA E SISTEMI INDUSTRIALI**
(XXIII ciclo)

Titolo della ricerca:

Magnetic field sensors suitable for high temperature and vacuum operation and for remote handling in harsh environment

(Sensori di Campo Magnetico adatti al funzionamento in alta temperatura e vuoto e Sistemi di manipolazione remota per il loro posizionamento in ambienti ostili)

L'Ing. Antonio Gallo ha svolto la sua attività di ricerca nel triennio 2008-2010 principalmente nel campo dello sviluppo di Sensori, con particolare riferimento ai Sensori di Campo magnetico utilizzabili in vuoto e in esperimenti per la fusione controllata a confinamento magnetico, ma anche in varie applicazioni industriali.

Nell'ambito di tale studio, il dottorando ha inizialmente approfondito la propria conoscenza sui metodi e sulle tecnologie dei Sistemi per le Misure Magnetiche e termiche in macchine per la fusione e per l'esperimento internazionale ITER, attualmente in costruzione a Cadarache (F).

In collegamento con il gruppo di Padova e altri gruppi internazionali, il dottorando ha partecipato allo sviluppo dei prototipi di Sensori magnetici tipo "low Temperature Cofired Ceramics (LTCC)" per ITER, svolgendo varie prove sperimentali per la caratterizzazione del comportamento dei sensori dal punto di vista magnetico, meccanico e termico.

Particolare attenzione ha dedicato alla misura delle tensioni spurie che si sviluppano in presenza di gradienti termici (TIEMF Thermally Induced Electromotive Force) che possono causare considerevoli derive nella misura dei campi magnetici durante gli esperimenti su ITER.

Oltre allo sviluppo e alla caratterizzazione dei Sensori magnetici, il dottorando ha inoltre preso parte alla sperimentazione di un crogiolo a levitazione magnetica sviluppato e realizzato presso il DTG, contribuendo alle simulazioni numeriche delle configurazioni magnetiche e alle misure sperimentali di caratterizzazione elettromagnetica.

Ha inoltre sviluppato simulazioni numeriche magnetiche, termiche e strutturali, tramite codici ad elementi finiti, per la verifica del progetto di sensori adatti al funzionamento in ambienti ostili e di schermi elettromagnetici. Ha inoltre studiato di Sistemi di Manipolazione Remota per il posizionamento e per il collegamento elettrico di Sensori per mezzo di connessioni e saldature operabili mediante robot.

Ha partecipato alla 45th Culham Plasma Physics Summer School 7-18 July 2008 a Culham, Oxford UK.

Il buon livello del suo percorso scientifico è peraltro documentato dalla stesura di memorie presentate a convegni internazionali e pubblicate o in fase di pubblicazione su riviste internazionali.

Al termine del triennio di Dottorato, l'Ing. Gallo risulta coautore delle seguenti pubblicazioni:

ARTICOLI PUBBLICATI SU RIVISTA INTERNAZIONALE

R. Chavan, G. Chitarin, R. Delogu, A. Encheva, A. Gallo, E. R. Hodgson, C. Ingesson, A. Le-Luyer, J. B. Lister, P. Moreau, J. Moret, S. Peruzzo, J. Romero, D. Testa, M. Toussaint, G. Vayakis, and R. Vila,
"The magnetic diagnostics set for ITER",
Fusion Engineering and Design 84 (2009) 295-299.

G. Chitarin, R. Delogu, A. Gallo, and S. Peruzzo,
"Technology developments for ITER in-vessel equilibrium magnetic sensors",
Fusion Engineering and Design 84 (2009) 593-598.

Duccio Testa, G. Chitarin, Antonio Gallo,
"The Magnetic Diagnostic Set for ITER",
IEEE Transactions on Plasma Science, Vol. 38, No. 3, Mar 2010, pp 284-294.

Simone Peruzzo, Giuseppe Chitarin, Rita S. Delogu, Antonio Gallo,
"Design proposal of a connection system for ITER in-vessel magnetic sensors",
Fusion Engineering and Design 85 (2010) 1707-1710

ARTICOLI SU ATTI DI CONGRESSO INTERNAZIONALE

Antonio Gallo, Giuseppe Chitarin, Rita Sabrina Delogu, Simone Peruzzo, George Vayakis,
"ITER in-vessel magnetic sensors prototyping and tests",
presentato al SOFT 2010 a Porto

Grando, L., Dal Bello, S., Ferro, A., Pilan, N., Rizzolo, A., Taliercio, C., Valisa, M., Agostinetti, P., Bettini, P., Gallo, A., Lazzaro, G., Tiso, A., Tollin, M., Zampiva, E., Zella, D., Hirano, Y., Kiyama, S., Sakakita, H.
"INTEGRATION DESIGN OF TPE-RX NEUTRAL BEAM INJECTOR ON RFX-MOD"
presentato al SOFT2010 Porto, Sept 2010.

D.Testa, H.Carfantan, M.Toussaint, N.Baluc,, R.Chavan, G.Chitarin, Y.Fournier, A.Gallo, J.Guterl, C.Hollenstein,
J.B.Lister, T.Maeder, J-M.Moret, S.Peruzzo, F.Sanchez, B.Schaller, G.Tonetti
"Analysis and Optimization of the Baseline System Design and Sensor Prototyping for the ITER High-Frequency
Magnetic Diagnostic Set"
IAEA Fusion Energy Conference, Daejeon, Korea 11-16 October 2010

ARTICOLI SU ATTI DI CONGRESSO NAZIONALE

G.Chitarin, R.S.Delogu, A.Gallo, S.Peruzzo
"Evaluation of the Outgassing Rate of in-vessel magnetic sensors for ITER",
XIX Congresso AIV, Senigallia Italy 19-21 maggio 2009

ATTIVITA' DIDATTICA ATTIVA

- Assistenza al Laboratorio di SPICE (Simulazione numerica di circuiti) nell'ambito del corso di "Elettrotecnica" per Laurea in Ing. Meccatronica (Vicenza), (I semestre AA 2008-2009).
- Attività di Tutor Junior per Laboratorio di SPICE (Simulazione numerica di circuiti) nell'ambito del corso di "Elettrotecnica" per Laurea in Ing. Meccatronica (Vicenza), (II semestre AA 2009-2010).

La valutazione complessiva dell'attività svolta dall'ing. Antonio Gallo lo fa ritenere pienamente meritevole di ammissione all'esame finale di dottorato. Il giudizio complessivo esprimibile circa l'attività e la preparazione dell'ing. Antonio Gallo è pertanto molto buono.

Il Supervisore
Prof. G. Chitarin